eISSN: 2791-8742
doi: 10.52460/src

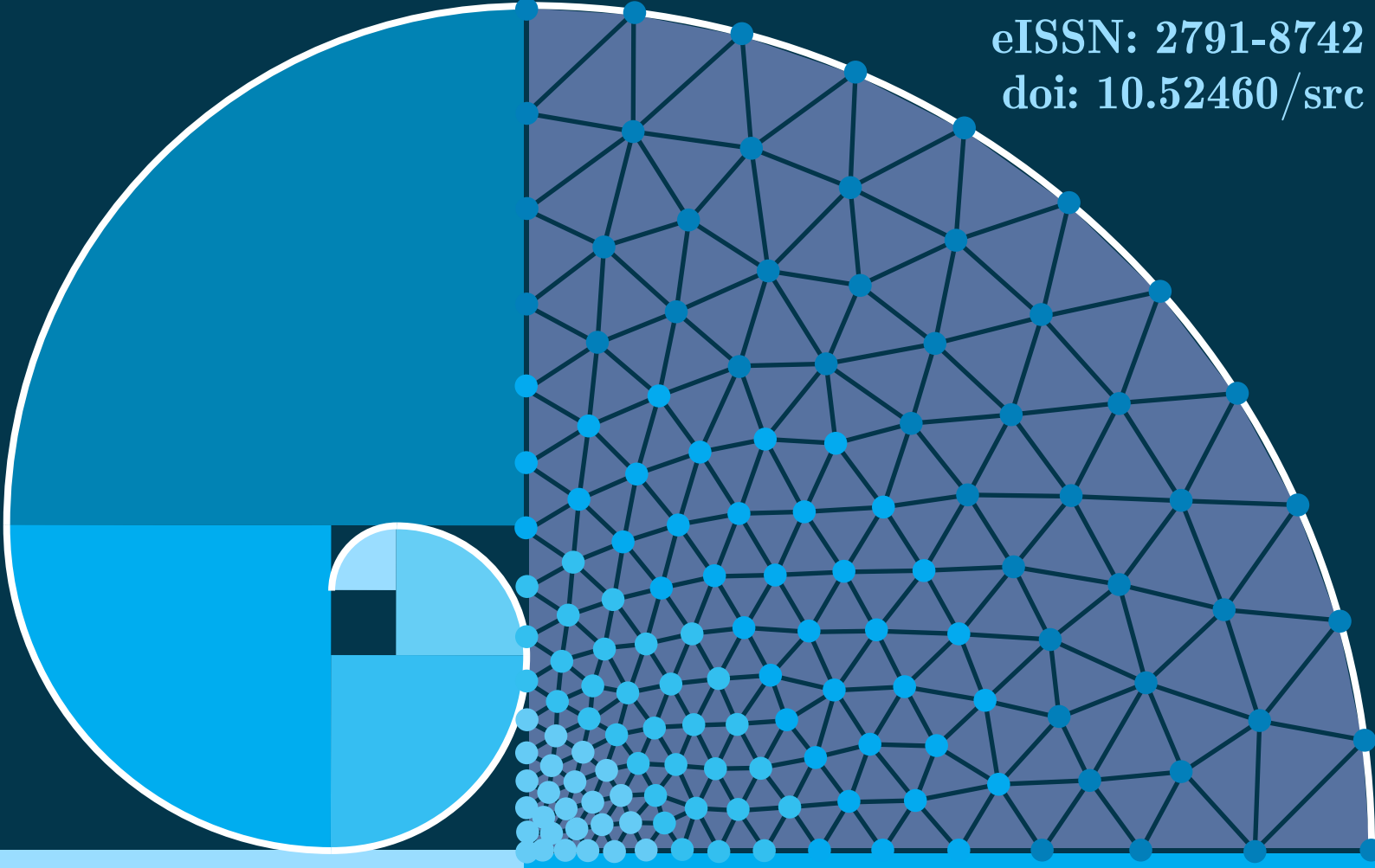

Scientific Research Communications

Volume 5
Issue 1
January 2025

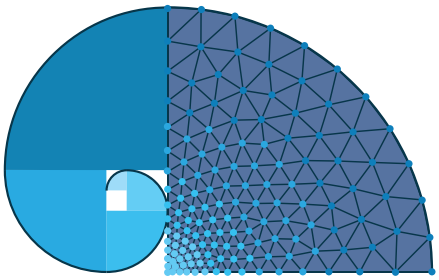

Scientific Research Communications
Volume 5, Issue 1, 2025

Editorial

Publisher
İzmir International Guest Students Association

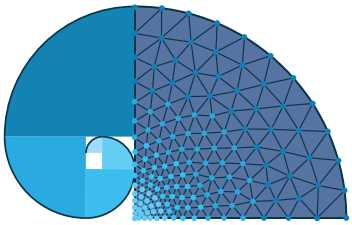

Scientific Research Communications

Volume 5, Issue 1, 2025

Contents

Research Articles

Scientific Research Communications

Solution of the Single Degree of Freedom System Using Bernoulli Collocation Method

Kübra Erdem Biçer*

Manisa Celal Bayar University, Department of Mathematics, Manisa, Türkiye

Research Article

*Correspondence:
kubra.erdem@cbu.edu.tr

Received: 6 June 2024
Accepted: 8 January 2025
Published: 24 January 2025

Keywords
Vibration
Spring-mass-damper system
Bernoulli polynomials
Collocation points
Approximate methods

Abstract

The fundamental subject of a single degree of freedom system's free vibration is essential in the field of mechanical vibrations, with applications in a wide range of engineering fields. This paper presents a novel numerical method for solving this problem based on Bernoulli polynomials in matrix form. The method is simple to implement and requires only basic linear algebra operations. The method is also very efficient; and can be used to solve problems with the single degree of freedom system. The proposed method is illustrated by a numerical example, and the results are compared with those of the exact solution. The results show that the proposed method is highly accurate and efficient.

1. Introduction

Understanding the natural oscillations of damped spring-mass systems with a single degree of freedom is a cornerstone of mechanical vibrations. In mechanical vibrations, the free vibration of damped spring-mass systems having single degree of freedom is essential for advanced systems. Interestingly, many complex systems can be simplified to a single degree of freedom spring-mass model. As a result, solving the equations of motion for this system can be used to solve many other more complex problems. There are a variety of effective methods for calculating solutions for a spring-mass-damper system excited by a harmonic force.

The approximation method based on Taylor polynomials (Kurt and Çevik, 2008), Laguerre (Savaşaneril, 2018) and Lucas polynomials (Savaşaneril, 2023) is used for the solution of single degree of freedom system. Also, an exponential matrix method is developed to solve delayed single degree of freedom system (Çevik et al., 2014). In addition, different matrix methods based on different polynomials have been developed for various type systems of differential equations (Yüzbaşı and Karaçayır, 2017; Yüzbaşı et al., 2012; Yüzbaşı and Yıldırım, 2021; Sezer and Kaynak, 1996; Bahşi et al., 2018; Gülsu et al., 2011; Baykuş and Sezer, 2017; Biçer and Dağ, 2023; Kürkçü et al., 2016; Çayan et al., 2022; Yıldız and Sezer, 2019).

How to cite this paper: Erdem Biçer, K. (2025). Solution of the single degree of freedom system using Bernoulli collocation method. *Scientific Research Communications, 5*(1), 1–10. https://doi.org/10.52460/src.2025.001

In this study, a matrix method based on Bernoulli polynomial is used to solve the single degree of freedom system. Also, this method has been used to solve high-order linear differential-difference equations, linear delay difference equations with variable coefficients, mixed linear Fredholm integro-differential-difference equations, nonlinear differential equations (Erdem and Yalçınbaş, 2012a; Erdem and Yalçınbaş, 2012b; Erdem et al., 2013; Erdem Biçer and Sezer, 2019).

We consider the Bernoulli polynomial solution of an m^{th} order differential equation given in Eq. (1):

$$\sum_{k=0}^{m} P_k x^{(k)}(t) = f(t), \tag{1}$$

with initial conditions:

$$\sum_{k=0}^{m-1} a_{ik} x^{(k)}(a) = \lambda_i,\ i = 0,1,\cdots,m-1. \tag{2}$$

$P(t)$ is analytic function defined on $a \le t \le b$ a_{ik}, λ_i are suitable constants. In the present method, the solution of (1) is expressed in the Bernoulli polynomial form as in Eq. (3):

$$x(t) = x_N(t) = \sum_{n=0}^{N} a_n B_n(t), \tag{3}$$

where, $B_n(t)$ is the Bernoulli polynomials and a_n, $n = 0,1,\cdots,N$ are unknown coefficients (Gülsu et al., 2011).

2. Fundamental Matrix Relations

The approximate solution of Eq. (1) in terms of Bernoulli polynomials can be expressed as in Eq. (4):

$$x(t) = x_N(t) = \mathbf{B}(t)\mathbf{A} \tag{4}$$

where,

$$\mathbf{B}(t) = [B_0(t) \quad B_1(t) \quad \cdots \quad B_N(t)], \mathbf{A} = [a_0 \quad a_1 \quad \cdots \quad a_N]^T. \tag{5}$$

Here, the Bernoulli polynomials $B_n(x)$ is defined by

$$\frac{te^{xt}}{e^t - 1} = \sum_{n=0}^{\infty} \frac{B_n(x)}{n!} t^n$$

or

$$B_n(x) = \sum_{r=0}^{n} \binom{n}{r} b_r x^{n-r}, \text{ which } b_r = B_r(0) \text{ (Apostol, 1976).}$$

The first few Bernoulli polynomials with respect to t follows in Eq. (6):

$$\begin{aligned} B_0(x) &= 1, \\ B_1(x) &= t - \frac{1}{2}, \\ B_2(x) &= t^2 - t + \frac{1}{6}, \\ B_3(x) &= t^3 - \frac{3}{2}t^2 - \frac{1}{2}t, \\ &\vdots \end{aligned} \tag{6}$$

Then, by using the Bernoulli polynomials $B_n(t)$given by (6), we write the matrix form $\mathbf{B}(t)$ as follows in Eq. (7):

$$\mathbf{B}(t) = \mathbf{T}(t)\boldsymbol{\zeta}^T. \tag{7}$$

where,

$$\mathbf{T} = [1 \quad \mathrm{t} \quad \cdots \quad t^N]. \tag{8}$$

$$\boldsymbol{\zeta} = \begin{bmatrix} \binom{0}{0} b_0 & 0 & 0 & 0 & 0 & \cdots & 0 \\ \binom{1}{0} b_1 & \binom{1}{1} b_0 & 0 & 0 & 0 & \cdots & 0 \\ \binom{2}{0} b_2 & \binom{2}{1} b_1 & \binom{2}{2} b_0 & 0 & 0 & \cdots & 0 \\ \binom{3}{0} b_3 & \binom{3}{1} b_2 & \binom{3}{2} b_1 & \binom{3}{3} b_0 & 0 & \cdots & 0 \\ \binom{4}{0} b_4 & \binom{4}{1} b_3 & \binom{4}{2} b_2 & \binom{4}{3} b_1 & \binom{4}{4} b_0 & \cdots & 0 \\ \vdots & \vdots & \vdots & \vdots & \vdots & \ddots & \vdots \\ \binom{N}{0} b_N & \binom{N}{1} b_{N-1} & \binom{N}{2} b_{N-2} & \binom{N}{3} b_{N-3} & \binom{N}{4} b_{N-4} & \cdots & \binom{N}{N} b_0 \end{bmatrix}. \tag{9}$$

Using the matrix relations in Eq. (4) and Eq. (7), it follows that:

$$x_N(t) = \mathbf{T}(t)\boldsymbol{\zeta}^T\mathbf{A}. \tag{10}$$

For the matrix relation between $\mathbf{T}(t)$ and its k −th derivative $\mathbf{T}^{(k)}(t)$ as:

$$\mathbf{T}^{(k)}(t) = \mathbf{T}(t)\mathbf{E}^k. \tag{11}$$

where,

$$\mathbf{E} = \begin{bmatrix} 0 & 1 & 0 & \cdots & 0 \\ 0 & 0 & 2 & \cdots & 0 \\ \vdots & \vdots & \vdots & \ddots & \vdots \\ 0 & 0 & 0 & \cdots & N \\ 0 & 0 & 0 & \cdots & 0 \end{bmatrix}. \tag{12}$$

By substituting the matrix form Eq. (11) into Eq. (10), the following matrix relation is obtained:

$$x_N^{(k)}(t) = \mathbf{T}(t)\mathbf{E}^k\boldsymbol{\zeta}^T\mathbf{A}, \qquad k = 0,1,\cdots,m. \tag{13}$$

3. Bernoulli Collocation Method

By using the collocation points,

$$x_i = a + \frac{b-a}{N} i, \qquad i = 0,1,\cdots,N. \tag{14}$$

into Eq. (1) gives Eq. (15):

$$\sum_{k=0}^{m} P_k x^{(k)}(t_i) = f(t_i), \tag{15}$$

which can be written in matrix form as:

$$\boldsymbol{W} = [w_{pq}] = \sum_{k=0}^{m} P_k \boldsymbol{T}(t)\boldsymbol{E}^k \boldsymbol{\zeta}^T, p, q = 0,1,\cdots,N.$$

For the particular solution, Eq. (15) is written briefly as Eq. (16):

$$\mathbf{WX} = \mathbf{F} \text{ or } [\mathbf{W};\mathbf{F}] \tag{16}$$

where,

$$\mathbf{W} = [w_{pq}] = \sum_{k=0}^{m} P_k \mathbf{T}(t)\mathbf{E}^k \boldsymbol{\zeta}^T, p, q = 0,1,\cdots,N. \tag{17}$$

Therefore, unknown Bernoulli coefficients matrix is obtained as in Eq. (18):

$$\mathbf{X} = \mathbf{W}^{-1}\mathbf{F} \tag{18}$$

which yields the desired Bernoulli coefficients $x_n, n = 0,1,\cdots,N$ of the particular solution.

The matrix form of the initial conditions in Eq. (2) is obtained as in Eq. (19):

$$\mathbf{U_i A} = \lambda \text{ or } [\mathbf{U_i};\lambda_i], i = 0,1,\cdots,m-1 \tag{19}$$

where,

$$\mathbf{U_i} = \sum_{k=0}^{m-1} a_{ik} \mathrm{T}(a)\mathbf{E}^k \boldsymbol{\zeta}^T = [u_{i0} \quad u_{i1} \quad \cdots \quad u_{iN}]. \tag{20}$$

Now, to solve the problem, the following augmented matrix is constructed by replacing the last 2 rows of $[\mathbf{W};\mathbf{F}]$ by the 2-row matrix $[\mathbf{U_i};\lambda_i]$:

$$[\mathbf{W};\mathbf{F}] = \begin{bmatrix} w_{00} & w_{01} & \cdots & w_{0N} & ; & f_0(t) \\ w_{10} & w_{11} & \cdots & w_{1N} & ; & f_1(t) \\ \vdots & \vdots & \ddots & \ddots & \vdots & \vdots \\ w_{N-m,0} & w_{N-m,1} & \cdots & w_{N-m,N} & ; & f_{N-m}(t) \\ u_{00} & u_{01} & \cdots & u_{0N} & ; & \lambda_0 \\ u_{10} & u_{11} & \cdots & u_{1N} & ; & \lambda_1 \\ \vdots & \vdots & \ddots & \vdots & \vdots & \vdots \\ u_{m-1,0} & u_{m-1,1} & \cdots & u_{m-1,N} & ; & \lambda_{m-1} \end{bmatrix}. \tag{21}$$

4. Solution of the Problem with Bernoulli Collocation Method

In this study, the solution of the viscously damped single degree of freedom system subjected to harmonic excitation (Inman, 2001):

$$M\ddot{x} + C\dot{x} + Kx = F_0 coswt \tag{22}$$

with initial conditions,

$$\begin{aligned} x(0) &= \lambda_0 \\ \dot{x}(0) &= \lambda_1 \end{aligned} \tag{23}$$

will be examined. Eq. (22) is a second order differential equation so $m = 2$ in Eq (1). Also, the constants are

$$P_2 = M, P_1 = C, P_0 = K.$$

5. Particular Solution

For the particular solution of the problem in matrix form, Eq. (22) is written briefly in the form of Eq. (24):

$$M\ddot{x} + C\dot{x} + Kx = \sum_{k=0}^{2} P_k \mathbf{T}(t)\mathbf{E}^k \boldsymbol{\zeta}^T \mathbf{X} = \mathbf{F} \tag{24}$$

or shortly,

$$\mathbf{WX} = \mathbf{F} \text{ or } [\mathbf{W}; \mathbf{F}]$$

where,

$$\mathbf{W} = [w_{pq}] = \sum_{k=0}^{2} P_k \mathbf{T}(t)\mathbf{E}^k \boldsymbol{\zeta}^T, p, q = 0,1,\cdots,N, \tag{25}$$

So, the unknown Bernoulli coefficients $x_n, n = 0,1,\cdots,N$ are obtained as in Eq. (26):

$$\mathbf{X} = \mathbf{W}^{-1}\mathbf{F} \tag{26}$$

for the particular solution.

6. General Solution

For the general solution of the problem, the matrix form of the initial conditions Eq. (23) is written as in Eq. (27)

$$\mathbf{U_i} = \sum_{k=0}^{1} a_{ik} \mathrm{T}(a)\mathbf{E}^k \boldsymbol{\zeta}^T = [u_{i0} \quad u_{i1} \quad \cdots \quad u_{iN}] \; i = 0,1. \tag{27}$$

and the augmented matrix is obtained as in Eq. (28)

$$[\mathbf{W};\mathbf{F}]=\begin{bmatrix} w_{00} & w_{01} & \cdots & w_{0N} & ; & f_0(t) \\ w_{10} & w_{11} & \cdots & w_{1N} & ; & f_1(t) \\ \vdots & \vdots & \ddots & \ddots & \vdots & \vdots \\ w_{N-2,0} & w_{N-2,1} & \cdots & w_{N-2,N} & ; & f_{N-2}(t) \\ u_{00} & u_{01} & \cdots & u_{0N} & ; & \lambda_0 \\ u_{10} & u_{11} & \cdots & u_{1N} & ; & \lambda_1 \end{bmatrix}. \tag{28}$$

In Eq. (24), if $rank\mathbf{W}=rank[\mathbf{W};\mathbf{F}]=N+1$ then the coefficient matrix A is uniquely determined and so the solution of the problem (1-2) is obtained as in Eq. (29):

$$x_N(t)=\mathbf{B}(t)\mathbf{A} \text{ or } x_N(t)=\mathbf{T}(t)\boldsymbol{\zeta}^T\mathbf{A}. \tag{29}$$

7. Numerical Example

A spring-mass-damper system with a mass of $M=10$ kg, damping coefficient of $C=20\,kg/s$ and spring stiffness of $K=4000\,N/m$ subject to an excitation force of amplitude $F_0=100\,N$ and frequency $\omega=10\,rad/s$ rad/s is examined with initial conditions $x(0)=0.01, \dot{x}(0)=0$. Based on these parameters, Eq. (22) can be expressed as

$$10\ddot{x}+20\dot{x}+4000x=100\,cos10t.$$

The exact solution obtained by the method of undetermined coefficients is as follows (Inman, 2001)

$$x(t)=tan^{-1}\frac{x_0\omega_d}{v_0+\xi\omega_n x_0}, A=\frac{1}{\omega_d}\sqrt{(v_0+\xi\omega_n x_0)^2+(x_0\omega_d)^2}, x=0 \text{ for free response,}$$

and

$$x(t)=tan^{-1}\frac{\omega_d(x_0-xcos\theta)}{v_0+(x_0-xcos\theta)\xi\omega_n-\omega xsin\theta}, A=\frac{x_0-xcos\theta}{sin\phi}$$
$$\theta=tan^{-1}\frac{2\xi\omega_n\omega}{\omega_n^2-\omega^2}, x=\frac{f_0}{\sqrt{(\omega_n^2-\omega^2)^2+(2\xi\omega_n\omega)^2}} \quad \text{for forced response.}$$

Firstly, using Eq. (17) the fundamental matrix equations is written as Eq. (30):

$$10\mathbf{T}(t)\mathbf{E}^2\boldsymbol{\zeta}^T\mathbf{A}+20\mathbf{T}(t)\mathbf{E}\boldsymbol{\zeta}^T\mathbf{A}+4000\mathbf{T}(t)\boldsymbol{\zeta}^T\mathbf{A}=100cos10t \tag{30}$$

First, let us determine both the particular solution and the general solution for the equation when $N=5$. To accomplish this, we need to calculate the necessary matrix equations. For $N=5$, the matrix $\mathbf{W}$ and the augmented matrix $[\mathbf{W};\mathbf{F}]$ are defined as follows:

$$\mathbf{W}=\begin{bmatrix} 4000 & -1980 & \frac{2000}{3} & -20 & -\frac{340}{3} & -\frac{10}{3} \\ 4000 & -1180 & \frac{104}{3} & \frac{872}{5} & -\frac{1972}{75} & -\frac{6442}{75} \\ 4000 & -380 & -\frac{832}{3} & \frac{428}{5} & \frac{6764}{75} & -\frac{3586}{75} \\ 4000 & 420 & -\frac{808}{3} & -\frac{472}{5} & \frac{6576}{75} & \frac{158}{3} \\ 4000 & 1220 & \frac{176}{3} & -\frac{868}{5} & -\frac{2548}{75} & \frac{6326}{75} \\ 4000 & 2020 & \frac{2120}{3} & 40 & -\frac{340}{3} & -\frac{10}{3} \end{bmatrix},$$

$$[\mathbf{W};\mathbf{F}] = \begin{bmatrix} 4000 & -1980 & \frac{2000}{3} & -20 & -\frac{340}{3} & -\frac{10}{3} & ; & 100 \\ 4000 & -1180 & \frac{104}{3} & \frac{872}{5} & -\frac{1972}{75} & -\frac{6442}{75} & ; & -\frac{4536}{109} \\ 4000 & -380 & -\frac{832}{3} & \frac{428}{5} & \frac{6764}{75} & -\frac{3586}{75} & ; & -\frac{8432}{129} \\ 4000 & 420 & -\frac{808}{3} & -\frac{472}{5} & \frac{6576}{75} & \frac{158}{3} & ; & \frac{5665}{59} \\ 1 & -\frac{1}{2} & \frac{1}{6} & 0 & -\frac{1}{30} & 0 & ; & 0.01 \\ 0 & 1 & -1 & \frac{1}{2} & 0 & -\frac{1}{6} & ; & 0 \end{bmatrix}$$

As indicated in the method, the particular solution is obtained as follows after certain matrix operations

$$x_p(t) = 8.4282770393x^5 - 20.4809690511x^4 + 16.234587123x^3 - 4.34431040004x^2 + 0.0647716655134x + 0.0463976936726$$

Similarly, the general solution is as follows:

$$x_g(t) = -61.2945777462x^5 + 79.2335823084x^4 - 30.1164823672x^3 + 3x^2 + 1.18423789293 \times 10^{-15}x + 0.01$$

The problem has also been solved for $N = 50$, $N = 100$, and $N = 200$. To demonstrate the accuracy of the method, the exact solution has been compared with $x_{50}(t)$ in Figure 1, with $x_{100}(t)$ in Figure 2, and with $x_{200}(t)$ in Figure 3. The graphs demonstrate the accuracy and reliability of the proposed method, as the solutions closely correspond to the expected theoretical behavior.

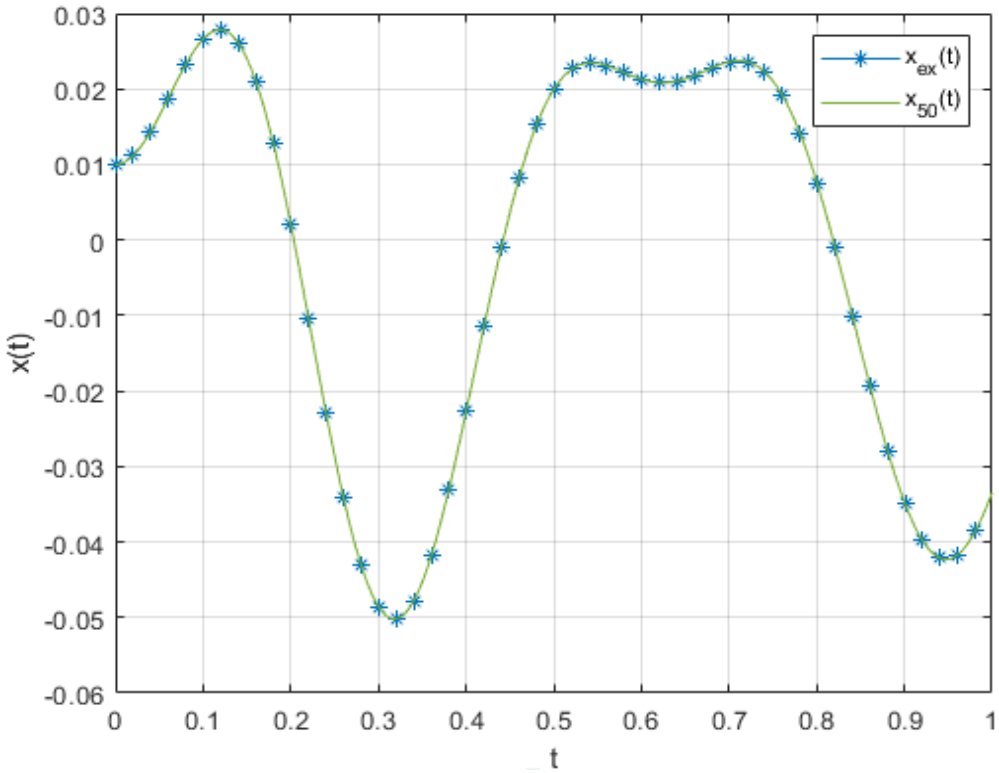

Figure 1. Comparison of the exact method and the approximate numerical method for the general solution of the problem for $N = 50$

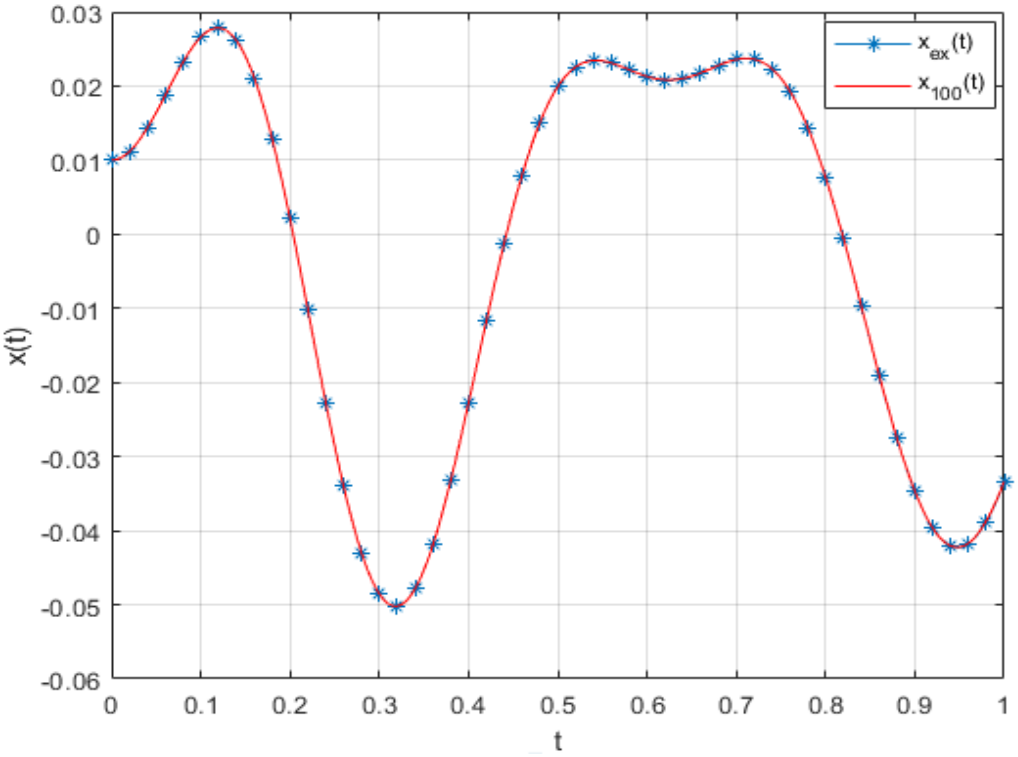

Figure 2. Comparison of the exact method and the approximate numerical method for the general solution of the problem for $N = 100$

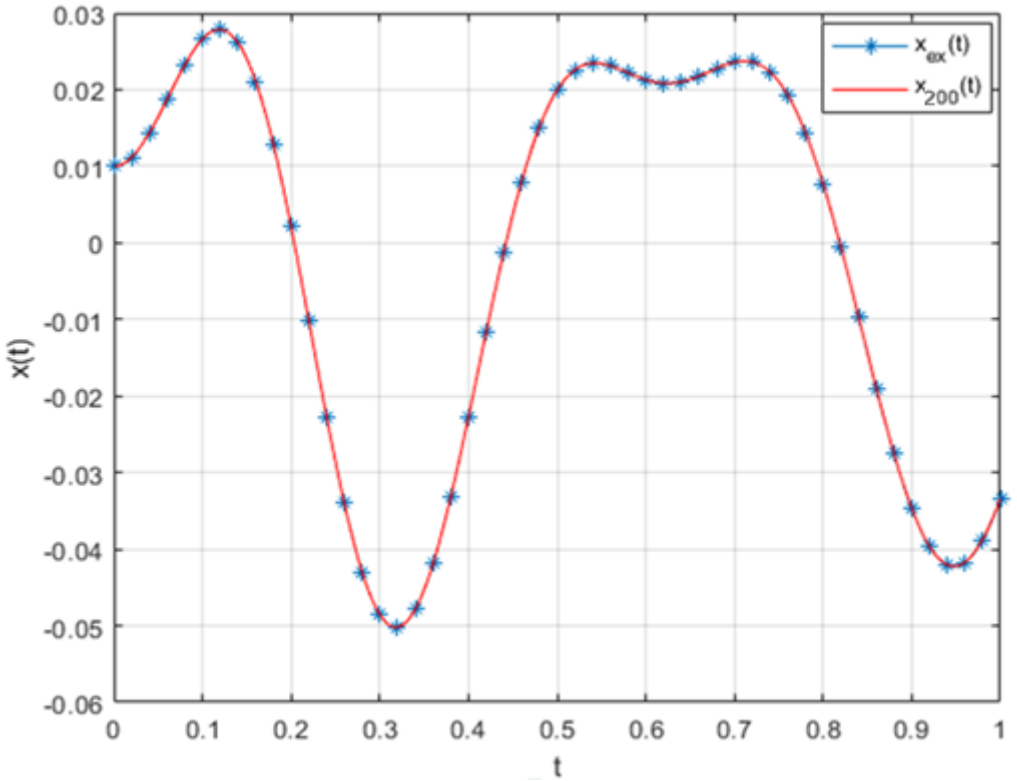

Figure 3. Comparison of the exact method and the approximate numerical method for the general solution of the problem for $N = 200$

8. Conclusions

In this study, Bernoulli polynomials are utilized to develop a novel method for solving the periodic motion of an underdamped single-degree-of-freedom spring-mass system subjected to harmonic excitation. This method is based on collocation points and matrix equations, offering a structured and computationally efficient approach. The problem is solved for different values of the system parameters, and the approximate solutions are illustrated graphically, demonstrating the method's practical applicability.

The results obtained through Matlab calculations highlight the accuracy and reliability of the proposed method, as the solutions closely align with expected theoretical behavior. Moreover, the method's ease of implementation and computational efficiency make it highly advantageous. Specifically, Bernoulli polynomials enable a reduction in computational complexity and provide high accuracy with fewer collocation points.

Beyond the specific application addressed in this study, the proposed approach has broader potential. It can be extended to solve higher-order systems of differential equations and other complex engineering or physical problems that exhibit periodic behavior. For instance, systems in vibration analysis, electrical circuit modeling, and wave mechanics could benefit from the enhanced computational efficiency and accuracy provided by this method.

In conclusion, this study underscores the utility of Bernoulli polynomials not only as a theoretical tool but also as a practical and efficient method for addressing real-world problems in engineering and physics. Their distinct advantages, such as ease of programming, computational efficiency, and adaptability to diverse problems, make them a promising alternative to traditional numerical methods. Future research could further explore these applications, solidifying Bernoulli polynomials as a cornerstone technique in applied mathematics and engineering problem-solving.

Author Statement

The author is solely responsible for the conceptualization, methodology, data collection, analysis, and manuscript preparation.

Conflict of Interest

The author declares no conflict of interest.

References

Apostol, T. M. (1976). Introduction to Analytic Number Theory. *Springer-Verlag*, Newyork.

Bahşi, M., Çevik, M., & Sezer, M. (2018). Jacobi polynomial Solutions of Volterra Integro-Differential Equations with Weakly Singular Kernel. *New Trends in Mathematical Sciences, 6*(3), 24-38.

Baykuş, N., & Sezer, M. (2017). Hybrid Taylor-Lucas Collocation Method for Numerical Solution of High-Order Pantograph Type Delay Differential Equations with Variables Delays. *Applied Mathematics and Information Sciences, 11*(6), 1795-1801.

Biçer, K.E., & Dağ, H.G. (2023). Numerical Solutions of Differential Equations Having Cubic Nonlinearity Using Boole Collocation Method. *Turkish Journal of Mathematics, 47*, 732-745.

Çayan, S., Özhan, B.B., & Sezer, M., (2022). Collocation Approaches to The Mathematical Model of an Euler–Bernoulli Beam Vibrations. *Mathematics and Computers in Simulation, 197*, 32-44.

Çevik, M., Bahşi, M.M., & Sezer, M. (2014). Solution of The Delayed Single Degree of Freedom System Equation by Exponential Matrix Method. *Applied Mathematics and Computation,* 242, 444-453.

Erdem Biçer, K., & Sezer, M. (2019). A Computational Method for Solving Differential Equations with Quadratic Nonlinearity by Using Bernoulli Polynomials. *Thermal Science, 23*(1), 275-283.

Erdem, K., & Yalçınbaş, S. (2012a). Bernoulli Polynomial Approach to High-Order Linear Differential-Difference Equations. *AIP Conf. Proc.,* 1479, 360-364.

Erdem, K., & Yalçınbaş, S. (2012b). Numerical Approach of Linear Delay Difference Equations with Variable Coefficients in Terms of Bernoulli Polynomials. *AIP Conf. Proc.,* 1493, 338-344.

Erdem, K., Yalçınbaş, S., & Sezer, M. (2013). A Bernoulli Polynomial Approach with Residual Correction for Solving Mixed Linear Fredholm Integro-Differential-Difference Equations. *Journal of Difference Equations and Applications*, 19, 1619-1631.

Gülsu, M., Yalman, H., & Sezer, M. (2011). A New Hermite Collocation Method for Solving Differential Difference Equations. *Applications and Applied Mathematics: An International Journal (AAM),* 6(1), 116-129.

Inman, D.J. (2001). Engineering Vibration, second ed. *Prentice-Hall*, New Jersey.

Kurt, N., & Çevik, M. (2008). Polynomial Solution of The Single Degree of Freedom System by Taylor Matrix Method. *Mechanics Research Communications*, *35*(8), 530-536.

Kürkçü, Ö.K., Aslan, E., & Sezer, M. (2016). A Numerical Approach with Error Estimation to Solve General Integro-Differential-Difference Equations Using Dickson Polynomials. *Applied Mathematics and Computation, 276*, 324-339.

Savaşaneril, N. B. (2018). Laguerre Series Solutions of The Delayed Single Degree of Freedom Oscillator Excited by an External Excitation and Controlled by a Control Force. *Journal of Computational and Theoretical Nanoscience*, *15*(2), 606-610.

Savaşaneril, N. B. (2023). Lucas Polynomial Solution of a Single Degree of Freedom System. *Sci. Res. Comm., 3*(1).

Sezer, M., & Kaynak, M. (1996). Chebyshev Polynomial Solutions of Linear Differential Equations. *Int. J. Mat. Educ. Sci. Technol, 27*(4), 607-618.

Yıldız, G., & Sezer, M. (2019). Truncated Bell Series Approach to Solve Systems of Generalized Delay Differential Equations with Variable Coefficients. *Turkish Journal of Mathematics and Computer Science, 11*, 105-113.

Yüzbaşı, Ş., Şahin, N., & Sezer, M. (2012). A Collocation Approach to Solving the Model of Pollution for a System of Lakes. *Mathematical and Computer Modelling, 55*(3-4), 330-341.

Yüzbaşı, Ş., & Karaçayır, M. (2017). An Exponential Galerkin Method for Solutions of HIV Infection Model of CD4+ T-Cells. *Computational Biology and Chemistry*, 67, 205-212.

Yüzbaşı, Ş., & Yıldırım, G. (2021). A Laguerre Approach for Solving of The Systems of Linear Differential Equations and Residual Improvement. *Computational Methods for Differential Equations, 9*(2), 553-576.

Scientific Research Communications

An Analysis of a Historical House in Alaçatı, Çeşme

Burcu Taşcı*

İzmir Kâtip Çelebi University, Department of Architecture, İzmir, Türkiye

Research Article

*Correspondence:
burcu.tasci@ikc.edu.tr

Received: 28 November 2024
Accepted: 8 January 2025
Published: 24 January 2025

Keywords
Cultural heritage
Conservation
Civil architecture
Architectural restoration
Alaçatı

Abstract

Alaçatı, located on the Çeşme Peninsula in Türkiye, is a historic and touristic coastal settlement. In recent years, despite the growing influence of tourism on its historic center, the settlement has managed to partially preserve its urban fabric and architectural heritage. In the historic center of the settlement, the civil architecture from the Ottoman period stands out as a prominent physical representation of cultural heritage. Historical houses are particularly significant for understanding the socio-cultural history of the settlement. Today, most of them have been restored and lost their original functions. On the other hand, some historical buildings hold a significant place in the city's memory, not only for their residential function but also for their commercial role in the settlement. A notable example is a two-storied stone house named "Yürük Grocery", situated in the Hacı Memiş Neighborhood, Alaçatı. Among the other historical houses, it stands out with its corner position, shared courtyard design and ground-floor function. This study aims to document the architectural features and cultural heritage values of this historical building, trace its evolution over time, and contribute to the literature. The methodology of this study includes documentation, literature review, archival research, fieldwork, and oral expressions. As a result, this study has identified three periods by examining the building's architectural features, history, construction techniques, and material characteristics in its evolution. In this way, the study contributes to maintain its historical identity.

1. Introduction

Çeşme Peninsula, located on the western coast of Türkiye in the İzmir Province, extends into the Aegean Sea. Çeşme, the town of Çeşme Peninsula, is known for its deep-rooted history, historical settlements and tourism activities. Alaçatı, located in the Çeşme district, is among the most prominent historic and touristic coastal settlements in Türkiye. The town center is located 7 km from Çeşme and 79 km from the center of İzmir. It is famous for its historic settlement, which reflects both Muslim and Greek Orthodox influences in its architecture and traditions, as well as its favorable climate for windsurfing and natural beauty. Although its historic center has become increasingly influenced by tourism in recent years, it has partially preserved its urban structure and architectural features. In the historic center of the settlement, the products of civil architecture belonging to the Ottoman period are seen as the most evident physical elements of cultural heritage.

How to cite this paper: Taşcı, B. (2025). An analysis of a historical house in Alaçatı, Çeşme. *Scientific Research Communications, 5*(1), 11–27. https://doi.org/10.52460/src.2025.002

Today, the historical houses of Alaçatı are located in three neighborhoods, in chronological order of historical development, the neighborhoods of Hacı Memiş, Tokoğlu, and Yeni Mecidiye (Figure 1) (Kocamanoğlu, 2010). The urban fabric is in a grid layout around Kemalpaşa Street, which runs east-west, and Mektep Street, which intersects it in a north-south direction. In the southern part of the area, in Hacı Memiş Neighborhood, which develops around Mithatpaşa Street, the layout is more organic. The commercial district of the settlement is located around Kemalpaşa Street and its surroundings (Yılmaz, 1983; Hersek; 1990). The buildings in this area have commercial functions on the ground floors and living spaces on the upper floors (Özgönül, 2010). Accordingly, it is vital to provide brief information about the evolution of the Hacı Memiş neighborhood as the oldest neighborhood of the settlement.

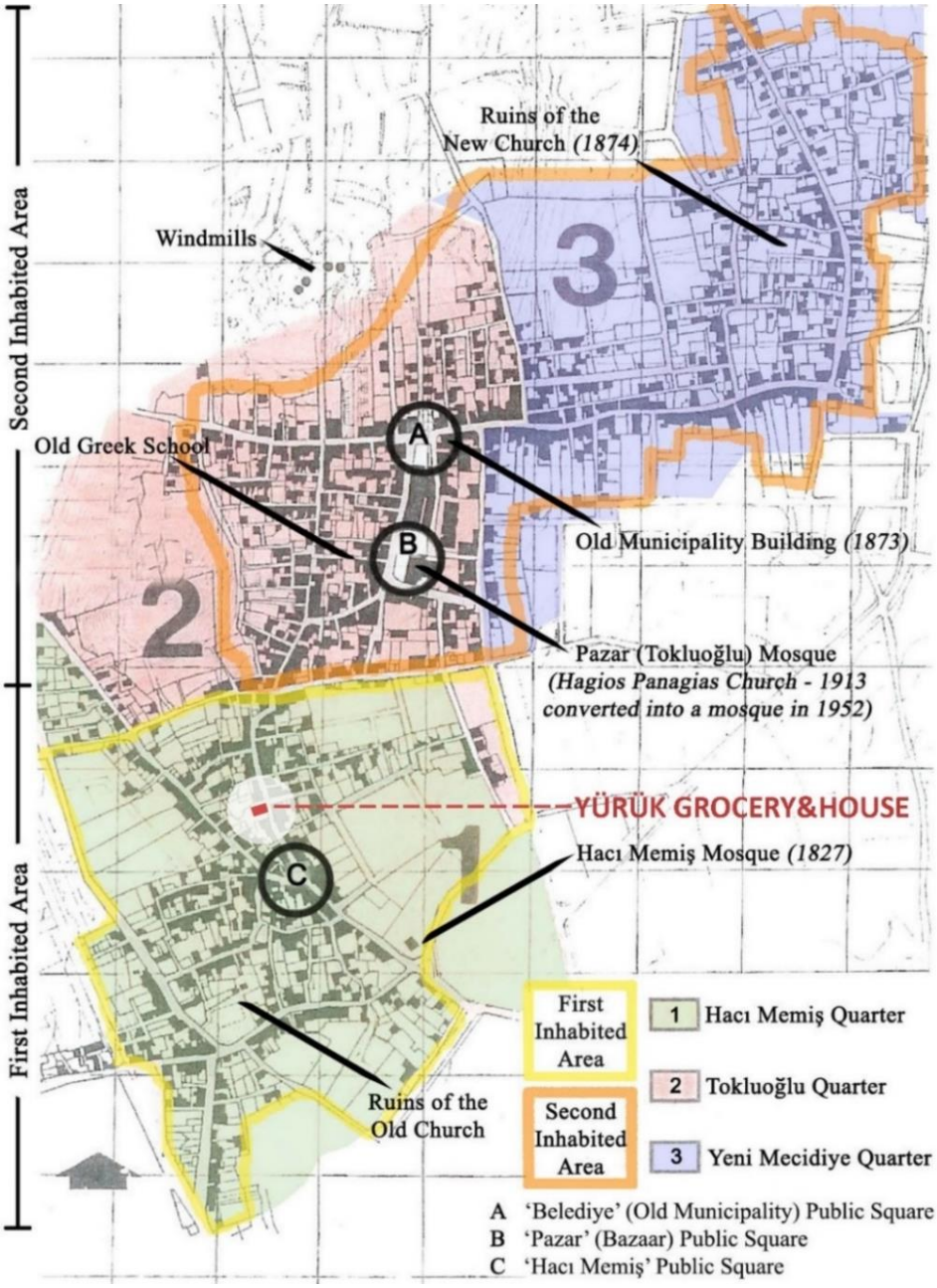

Figure 1. Location of the building (The map, obtained and revised by Akbaylar, 2008 from the Alaçatı Municipality archive, has been reorganized.)

Alaçatı has been an important place where various cultures and population movements have come together throughout history. In the 16th century, approximately 80% of the population was Muslim in Alaçatı. On the Çeşme Peninsula, especially from the second half of the 19th century to the early 20th century, the majority of the population began to be composed of Greek Orthodox Christians. The main reasons for this include earthquakes, epidemics, and decisions regarding land use. According to Baykara, deaths caused by epidemics led to a decrease in the population and created a significant labor shortage in the region. The ongoing population decline at the end of the 18th century presented an important opportunity for Greek workers, and during this period, the population balance shifted, increasing the Greek population on the peninsula (Baykara, 1990). Another reason is the 1881 earthquake, which devastated two-thirds of Chios (Sakız) Island, and because the Çeşme Peninsula was less affected, many displaced people from the island settled on the Çeşme Peninsula (Beyru, 2011). Additionally, it is understood that the foundations with large lands provided labor from the growing, job-seeking population on the islands to work the land (Şimşir, 2018).

Hacı Memiş Ağa, who had been a janissary in the Ottoman Empire, came to Çeşme and settled in Alaçatı at the end of the 18th century. Hacı Memiş Ağa became the owner of a great part of Alaçatı. The south of Alaçatı was totally boggy until 1850's (Atilla and Öztüre, 2006). From the beginning of the 19th century, Greeks living in Chios Island came to Alaçatı in order to work in the fields of Hacı Memiş. Hacı Memiş Ağa took the lead in drying of the bogs at the southern part with a project of opening canals reaching the natural port at the south. He then built the Muslim district at this southern area. Muslim neighborhood was settled down extends from southern of Alaçatı to the port of Alaçatı around the Hacı Memiş Mosque in today's Hacı Memiş District (Gezgin, 2007).

Hacı Memiş neighborhood, as the oldest neighborhood of Alaçatı, has historical residential buildings dating back to the mid-19th century and the early 20th century. Historical houses that are built from stone are important for understanding the socio-cultural background of the settlement. However, most of the historic houses have been restored to serve the tourism industry and have lost their original functions. On the other hand, some historical buildings hold a significant place in the city's memory not only for their residential function but also for their commercial role in the settlement. In Alaçatı, one such example is the "Yürük Grocery" (Turkish: "Yürük Bakkal"), located in the Hacı Memiş Neighborhood. The owner of "Yürük Grocery" and the house was a prominent local figure, with both the grocery store and the home serving as central hubs for the community of Alaçatı. The building is a corner building with two stories and a shared rear courtyard. In its original state, the ground floor is dedicated to commercial and storage purposes, while the upper floor is used for living space. This historical building is noteworthy because, in addition to its residential function, it is one of the few groceries in Alaçatı, and such commercial buildings are often important places for gathering, commerce, and community life in traditional settlements like Alaçatı. Among the other historical houses, it stands out with its corner position with a shared courtyard scheme and its ground floor function. The aim of this study is to document the architectural features and cultural heritage values of a historical building, trace its evolution over time, and contribute to the literature.

2. Method

This study examines a listed historic building in Alaçatı, focusing on its historical and architectural characteristics while documenting its evolution over time. The research methodology integrates several components, including documentation, literature review, archival research, field studies, and oral testimonies. Historical photographs, maps, drawings, legal documents, physical traces from the building, and comparative studies made on the buildings from the same period in the vicinity were utilized to reconstruct the building's

original state. Site surveys were conducted in September 2021, December 2021, and October 2024.

3. Yürük House and Grocery

The historical building is located in the city of İzmir, in Çeşme district, at the address of Alaçatı Neighborhood, Block 129, Parcel 7, at the corner where 12012 Street (formerly Mithatpaşa Street) intersects with the dead-end street continuing from 2019 Street (formerly Uludağ Court -*Uludağ Çıkmazı*) (Figures 1,2). In 2012, Alaçatı was designated a neighborhood of Çeşme under the 6360 Law. However, throughout its history, the building was originally located in the Hacı Memiş Neighborhood, as detailed above. The building has two façades oriented to Mithatpaşa Main Street and Uludağ Court and has a corner chamfer in the area where these streets meet. The building is surrounded by historical houses, both adjacent to it and across from it.

Figure 2. Ownership pattern of the building (URL1)

Today, the building is located within the boundaries of the 'Urban Conservation Area' declared in 1997 and expanded in 2004 by İzmir No 1 Regional Conservation Council of Cultural and Natural Entities (numbered 6766, dated 10.04.1997; dated 04.06.2004). In 2006, the building has been listed as the second group immovable cultural asset to be preserved within the urban conservation boundaries of Alaçatı (numbered 1314, dated 31.03.2016, İzmir No 1 Regional Conservation Council of Cultural and Natural Entities decision).

3.1. Periods of the Building

It was determined that the building has three periods in the historical process, and in this study, these three periods will be examined in detail.

First Period of the Building

The first period represents the time when the building was constructed (Figure 6). The exact date of the building is not known since there are no inscriptions and dates related to the history of the building, inside and outside the building. However, the building dates back to the second half of the 19th century based on the plan and façade typologies (Özgönül, 1996; Çetinel, 2021).

It is known that, like most buildings in Alaçatı at the time, this building belonged to a non-Muslim family. The current owner has confirmed similar information. However, there is limited information about its original Greek Orthodox owners.

In 19th-century Alaçatı, the ground floor and first-floor plans of local residential architecture were designed entirely independent of one another. Accordingly, the houses are categorized into three different typologies based on the ground floor layout: first type (ground floor with commercial functions), second type (ground floor used for production and storage) and third type (ground floor with residential use) (Kocamanoğlu, 2010). Accordingly, this building belongs to the first type of building group. The ground floor and first floor plans of this building have also been designed separately. The building had a residential and commercial function, reflecting a ground floor with a commercial function and an upper floor plan with hall (sofa). The simplest floor plan is observed during this period. Due to its corner location, the eastern façade is angled, and it is believed that the reason for the angled design on the western façade is the water well located in the shared garden/courtyard, which was crucial for water supply.

In this period, based on the literature review and traces from the building, it was determined that the section located to the west of the two-story main building, which includes a warehouse, workshop, and toilet, is a single-story structure. Above these spaces, there is a terrace (*taraça*). Thus, in the early period, it was understood that the building had a terrace located near the kitchen, which is commonly seen at the rear façades of almost all houses in Alaçatı (Yılmaz, 1983; Hersek, 1990; Kocamanoğlu, 2010). The shop (*mağaza*) opening to the street on the ground floor consists of a single, large space. It contains a fireplace located at the corner of the space. In this period, the service areas of the shop, such as the workshop, warehouse, and toilet, were located in the western part of the building. Written sources indicate that toilets were positioned in the garden in the early period (Hersek, 1990; Kocamanoğlu, 2010). However, in this building, which has a shared courtyard/garden, it is thought that these service areas are associated with the garden (Figure 3).

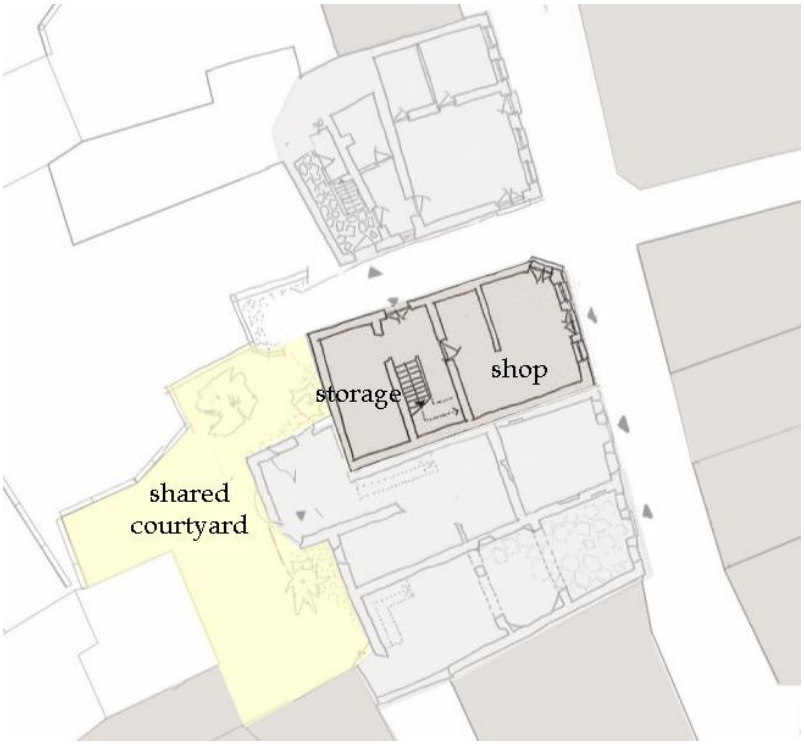

Figure 3. Schematic plan drawing of "Yürük Grocery" in 2011 (Kocamanoğlu, 2010)

Access to the residential entrance and service areas is provided directly from a side street. The entrance hall (*taşlık*) has a staircase leading up to the first floor. This stone staircase leads to a hall (*sofa)* on the upper floor, which has residential function. In these plan types, the rooms and kitchen are arranged around the hall. The staircase is positioned against the wall in the planning. The main room and kitchen are accessed from the hall. According to the traces from the building, it has been shown that the original kitchen wall continues and meets the stone wall at an angle (slanted), dividing the hall and indicating that the front part of the building was used as the main room. It is thought that this wall, which starts from the kitchen, is original and made of wooden frame up to the section where it angles. The connection of this wall with the balcony door, which was converted into a window by the users, also supports this idea. The main room is a spacious room with openings on both façades of the corner of the building and a balcony. The fireplace inside the kitchen is directed toward the terrace. Access to the terrace, which overlooks the shared courtyard, is also provided from the hall.

Second Period of the Building

In the second period, after the population exchange, non-Muslim residents left Alaçatı. The Yürük family, who are the current owners of the building, began living here. The ancestors of the present users migrated from Kınalı village, Kavala and Thessaloniki to Alaçatı in 1924 (Aslankan, 2008). The residential and commercial functions continued in this period. During this period, the ground floor was used as a grocery store. "Yürük Grocery" has been one of the few grocery stores in Alaçatı and a well-known commercial space (Figures 4-6). In this period, various changes were made to the upper floor, particularly to the terrace and the main room, to meet housing needs.

In this period, a part of the terrace was enclosed and used as a kitchen and a toilet/bath. It has been found that the toilets were removed from the garden after the Greeks migrated. The toilet/ritual bath that was originally located on the ground floor was added to the terrace in this period, and the workspace/stable area on the ground floor was expanded. Additionally, based on traces from the building, a storage area was added under the stone staircase to serve as a shop/store space. On the first floor, it was understood that the users divided the main room into two parts, creating an additional room.

Figure 4. "Yürük Grocery" in the early 1990s; (a) the window at the corner converted into a door, (b) eastern façade (URL2)

In the recent period when the building was used as a grocery store, changes were made to the ground floor façade. While the original wooden door was preserved, the windows were fitted with double-winged iron frames and fixed iron grille. The original window on the corner was enlarged and turned into a double-winged iron-framed door. The front façade of the structure is covered with a large ivy. On the upper floor, the balcony usage was canceled by the users, or the demolished balcony was replaced with a window instead of a door opening. The wooden shutters have disappeared, and as seen in old photographs, the windows were originally double-winged, unglazed, and wooden. The wall and chamfered section of the north façade of the main room were repaired and renewed after damage and demolition to the original wall. Traces from the building, oral history research, and old photographs show that the kitchen and toilet were renewed with modern construction techniques after damage and demolition to the original walls and flooring. These areas feature concrete flooring and ceramic tiles.

Figure 5. Main entrance of "Yürük Grocery" in 2011 (URL3)

Third Period of the Building

In the third period (probably after 2010s), the building gained its current function of accommodation (boutique hotel) and commerce (café), reaching its present physical state (Figure 7). This period describes the building's current condition (Figure 6).

Today, the ground floor of the building, used for commercial purposes, was open for use as a café until the implementation of the restoration project began, while the upper floor has been unused for a long time. Implementation of restoration project of the building will be started on 2025.

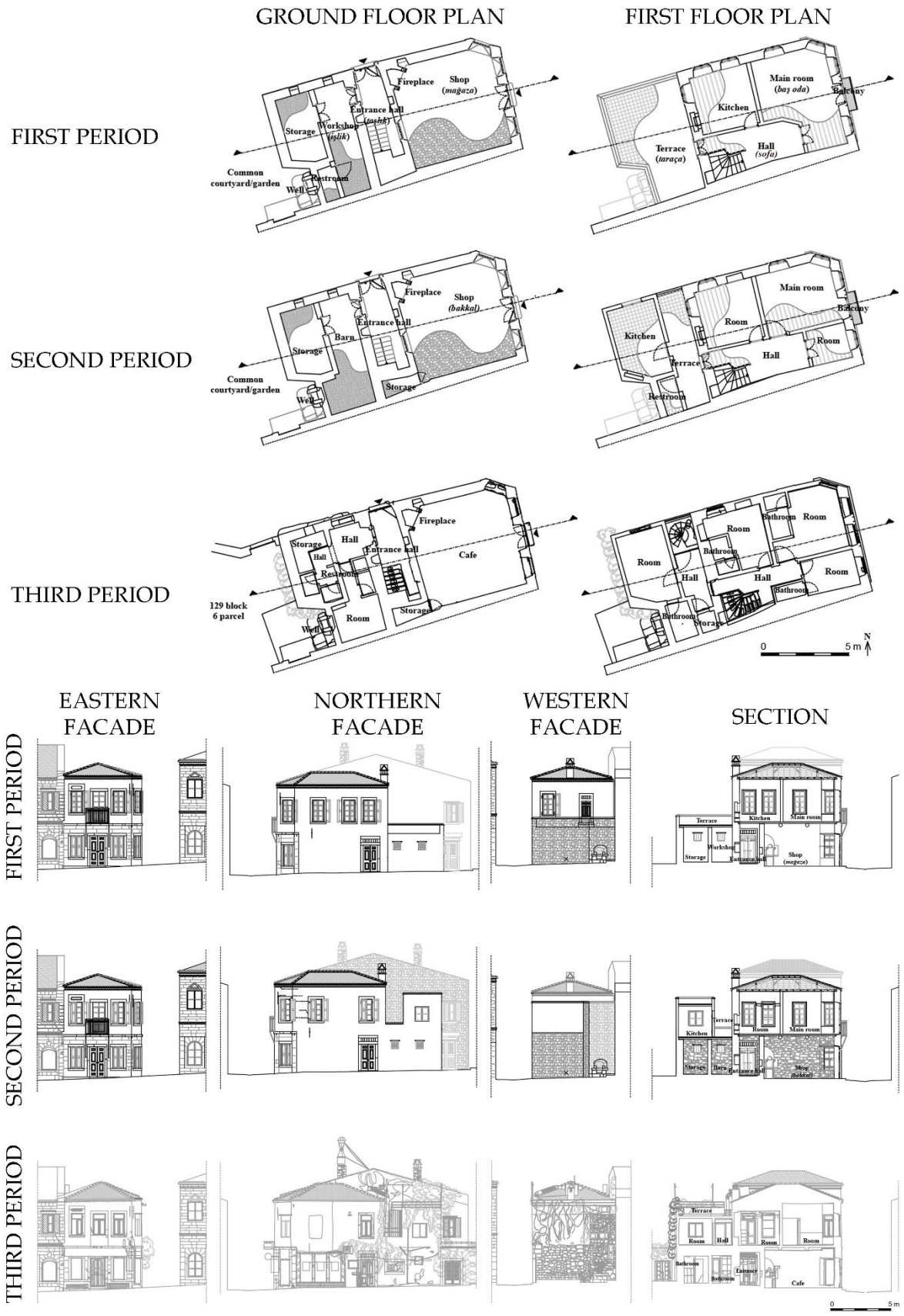

Figure 6. Drawings showing the three periods of the building

Figure 7. Façade view of the building in 2015 (Yandex, 2015)

3.2. The Plan Characteristics of the Building

The plan characteristics of the building will be examined on a room-by-room basis, separated into the ground floor and first floor, based on its current condition.

Ground Floor

The ground floor consists of a shop (*mağaza*), entrance hall (*taşlık*), workshop (*işlik*), storage/barn, and restroom.

Shop

The stone-framed door and window openings leading from the street to the shop are original. It has been found from traces in the building and oral history research that the shop is connected to the entrance hall through a window opening. It has been determined through traces from the structure and oral history research that the shop was connected to the entrance hall by a window opening. There is an original stone fireplace located at the corner of the shop (Figure 8). Right next to this fireplace, there is an original niche in the wall. The shop features original iron hook eyes belonging to the doors and windows. Based on traces from the building and comparative studies with surrounding buildings, it has been determined that the stone-framed, stone-silled windows were covered with wooden shutters. The stone-framed door, as seen in old photographs of the building, is a double-winged wooden door. It is known from traces in the building, old photographs, and oral sources that the original window at the corner was converted into a door for a period, but it has been restored as a window today. According to written sources and comparative studies with surrounding buildings, the walls are made of unplastered stone. On the opposite wall of the entrance door, on the western wall of the space, there is a trace that protrudes from the wall. According to information obtained from oral sources, this trace belongs to the opening that connects the entrance hall with the shop. This opening is believed to have a stone frame and wooden shutters based on comparative studies within the building. The original flooring of the shop has been identified as stone, based on traces from the building and information from written sources. The two wooden beam rafters in the ceiling are original (Figure 8). In the second period, according to traces from the building, a storage area was added under the stone staircase to serve the shop. Additionally, changes were made to the ground floor façade while the building was used as a grocery store. While the original wooden door was preserved, double-winged iron frames and fixed iron grilles were installed on the windows instead of wooden shutters. The original window at the

corner was enlarged and converted into a double-winged iron-framed door. The ivy on the front façade is notable in this period (Figure 4).

Figure 8. In 2021, (a) shop used as a café and (b) fireplace

Entrance hall

The stone-framed, double-winged wooden door with a vent on top, providing access from the side street to entrance hall, is original (Figure 9). In the entrance hall, there are two original stone niches facing each other. Access to the service spaces, including the workspace, storage, and toilet, is provided through the original stone-framed opening. Based on a comparative study in the building, this opening has been closed with a double-winged wooden door. The original L-shaped stone staircase in the entrance hall leads to the living floor (Figure 10).

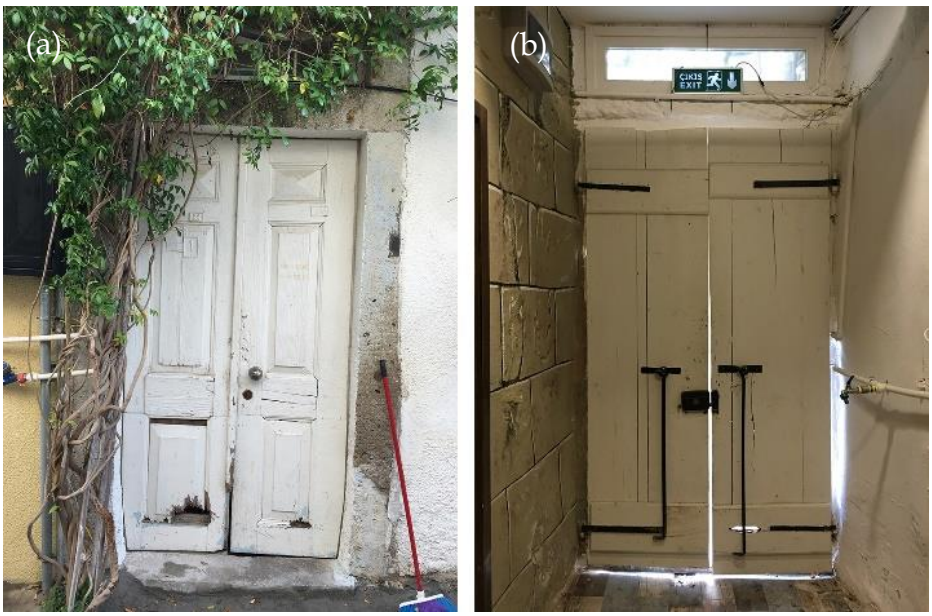

Figure 9. Original wooden door in the entrance hall (a) front, (b) the back

The walls, according to information from written sources and comparative studies with surrounding buildings, are made of unplastered stone. The original flooring of the entrance

hall, as seen in old photographs and written sources, is made of stone. The original ceiling, according to a comparative study within the building and information from written sources, consists of wooden beams. The walls of the entrance hall, as seen in old photographs, are plastered and painted.

Figure 10. Entrance hall with (a) stone staircase and (b) wooden balustrade, in 2021

Workshop

The shape of the workshop has been determined based on traces from the building (due to deformation in the stone wall of the storage/stable, located at the corner). The window opening on the north façade has been created based on traces from the building and a comparative study within the building. The window opening has been closed with a wooden shutter on the interior and a wrought iron grille on the façade, based on a comparative study with surrounding buildings. According to information obtained from written sources and based on a comparative study with the surrounding area, the walls are made of unplastered stone and the original flooring is compressed earth. The ceiling, based on traces from the building, is made of wooden beams. In the second period, the toilet/ritual bath was added to the terrace, and the workshop/stable area on the ground floor was expanded.

Storage/Barn

Access to the storage/barn is provided through an original stone-framed opening. This opening has been closed with a wooden door, based on a comparative study with the surrounding area. There is an original window opening on the north façade. The window opening has been closed with a wooden shutter on the interior and a wrought iron grille on the façade, based on a comparative study with surrounding buildings. The walls, according to information from written sources and comparative studies with surrounding buildings, are made of unplastered stone. According to information obtained from written sources, the original flooring is compressed earth. The ceiling, based on traces from the building and a comparative study within the building, consists of wooden beams. During the period when the building gained its function as a boutique hotel and café/restaurant, several wet areas and storage rooms were added to this area, divided by brick walls.

Restroom

In this building, which does not have a garden, the restroom is located in relation to the ground floor service areas based on information obtained from written sources and architectural requirements. Access to the toilet is provided through a wooden door, based on a comparative study of the surrounding area. The walls, according to information from written sources and comparative studies with surrounding buildings, are made of unplastered stone. The floor, according to information obtained from written sources, is compressed earth. The ceiling, based on traces from the building and a comparative study within the building, consists of wooden beams.

First Floor

The first floor is comprised of one main room (*baş oda*), kitchen, hall *(sofa),* and terrace (*taraça*).

Main room

The double-leaf wooden door providing access from the hall to the main room was determined based on a comparative study with the surrounding area (Figure 11). Based on traces from the building, it is clearly understood that one corner of the main room has a beveled edge (as the original wall continues in a beveled manner). In the main room, the vented window directly opposite the door, along with the vented door opening to the terrace, serves the purpose of ventilation (Terim, 2011). There is a window opening on the north façade that was later closed by the users. Based on a comparative study with the surrounding area, in its original state, the double-leaf wooden windows facing the front and side façades are wooden shuttered, with wooden sills (as determined in a comparative study within the building) and stone jambs. The original iron hinges for the wooden shutters are located on the façade. In the main room, based on traces from the building, oral history research, and a comparative study with the surrounding area, it is understood that there was a balcony. The original stone-framed door leading to the balcony was later closed by the users and converted into a window. A double-leaf wooden door was placed in this opening, based on a comparative study with the surrounding area. The balcony, based on a comparative study with the surrounding area, is framed with iron railing and its floor is covered with timber. The walls were originally plastered and painted. The original floor, based on a comparative study within the building, consists of timber. The original ceiling, according to information from written sources and a comparative study with surrounding buildings, is a wooden beam ceiling. In the second period, it is believed that the users divided the main room into two (by demolishing most of the beveled wall) with a brick wall to create an additional room. The entrance to the main room, based on traces from the building, is through a single-leaf wooden door. The balcony in the main room has either been removed or its use discontinued, with the door opening converted into a window. Additionally, the wall facing the north façade of the main room and the beveled part has undergone repairs and restoration after damage and destruction to the original wall. The original window in this wall has been closed. Other windows, as seen in old photographs, are double-leaf and wooden.

Kitchen

The kitchen is accessed from the hall through a single-leaf wooden door placed in the original opening (Figure 11). In its original state, the kitchen had a window opening facing the terrace. However, when the building was converted into a boutique hotel, the window was closed and transformed into a niche. Based on oral history research, it has been determined that there was a fireplace in the same wall that was closed by the users. The placement of the fireplace in the kitchen was confirmed by combining this information with the projection of the original chimney on the roof and data obtained from written sources. When the building was converted into a boutique hotel, the fireplace was closed, and a bathroom was added in front of it. The wooden shelf niche in the kitchen, as seen in elevation photo dated 2015, was created

in the second period by closing the original window. The original wooden sill of the stone-framed window facing the north façade is still present. Based on a comparative study with the surrounding area, the kitchen windows, in their original state, are double-leaf wooden windows, with wooden shutters, wooden, and stone jambs. The original iron hinges for the wooden shutters are present on the façade. The walls were originally plastered and painted. The original floor, as determined by a comparative study within the building, is made of timber. The original ceiling, according to information from written sources and a comparative study with surrounding buildings, is a wooden beam ceiling. In the second period, based on traces from the building and oral history research, it is observed that the kitchen was moved to the terrace, and the window in the north wall was closed, converting the wooden shelf niche into a cupboard. Based on written sources and oral history research, it is known that the kitchen section was repaired and renovated with modern techniques following the damage and destruction in the wooden-frame walls filled with stone.

Figure 11. (a) Main room, and (b) kitchen used as a room, in 2021

Hall

The hall is accessed via the original stone staircase. There is an original niche in the staircase wall. In the hall, there is an original wooden railing with a wooden baluster from the staircase. The walls are plastered and painted. The floor of the hall, based on traces from the building, is made of timber. The original ceiling, according to information from written sources and a comparative study with surrounding buildings, is a wooden beam ceiling.

Terrace

The vented opening with stone jambs, which provides the transition from the hall to the terrace, has been closed with a double-leaf wooden door as a result of the comparative study within the building. This door has its original iron hinge eyes. The presence of a ventilated door and window on this façade confirms that the hall opens to an open area like a terrace. In Alaçatı, terraces are typically found on the rear façades of nearly all traditional houses. In this building, the open terrace is surrounded by a stone parapet, as confirmed by a comparative study with the surrounding area. The original floor is believed to be made of tile mosaic based on information from written sources and architectural requirements due to climatic conditions. In the second period, it was determined through traces from the building and oral history research that users added a kitchen and bathroom/restroom to the terrace. In the second period, a wooden-frame wall with stone filling was built on the terrace to add a kitchen. Access to the kitchen is provided through a single-leaf wooden door, determined through a comparative study with the surrounding area. The floor is tiled with mosaic, the walls are

plastered and painted, and the ceiling has wooden beam construction. Based on oral history research, the location of the fireplace in the kitchen is referenced by the angled stone wall. The wooden window with plastered sills on the north façade of the kitchen was added based on old photographs and traces from the building.

In the phase when the upper floor was converted into a boutique hotel, a room with a bathroom and storage were added, with access to the terrace roof via a round metal staircase.

3.3. Façade properties

Eastern façade

The eastern façade of the building is covered with cut stone on the ground floor (Figure 12). The upper floor, due to traces of plaster and paint visible in old photos and based on information from written sources and comparative studies with nearby buildings, is determined to be plastered and painted. The stone jambs and stone floor cornice on the eastern façade are original. On the upper floor, the demolished balcony and the balcony door, which was converted into a window, have been replaced with a balcony featuring an iron railing. The balcony is supported by a wrought iron element, according to traces in the structure and data obtained from written sources. In old photos, double-winged iron windows and iron railings are visible on the ground floor. In the angled section, the original window has been converted into an iron door. As a result of the balcony's demolition, the balcony door has been closed and turned into a window by the users. The windows on the first floor, as seen in old photos, are double-winged, without divisions, and wooden. In the angled section, Ottoman-style roof tiles eaves cornices have disappeared and been replaced with plaster eaves cornice.

Figure 12. Façade views of the building, (a, b) eastern, (c) northern, and (d) western

Northern façade

The northern façade (except for the cut stone-clad angled ground floor) is considered to be plastered and painted based on comparative studies with surrounding buildings (Figure 12). The stone jambs on this façade, where the original residential entrance is located, are original. Traces of a closed window are visible on the façade. It has been determined through comparative studies with the surrounding area that the windows of the workshop and storage have iron grilles. Based on traces from the building and comparative study in the building, it is believed that eaves cornices on this façade were originally made of Ottoman-style roof tiles.

Due to repairs, the eaves cornices made of Ottoman-style roof tiles have disappeared from the first floor of the building, and traces of the closed window are visible. The façade of the

renovated kitchen is plastered and painted, and its wooden window, as seen in old photographs, is divided into three sections. The terrace is surrounded by a mosaic parapet.

Western façade

Today, the western façade is largely covered with ivy; however, in its original state, the façade was made of unplastered rubble stone on the ground floor, and plastered and painted on the upper floor (Figure 12). A terrace with a stone parapet is visible on the upper floor. The stone jambs of the vented door leading to the terrace on the western façade are original. In this stone-arched opening, a wooden, double-leaf door has been identified through comparative analysis. This façade also features a stone-arched, wooden shuttered, double-leaf wooden window. Based on traces from the building and internal comparative analysis, it is believed that there was Ottoman-style roof tiles eaves cornice. The chimney of the kitchen fireplace is visible on this façade. It is known that traditional houses in Alaçatı commonly had wells in either shared or individual gardens, which were crucial for water supply. It is believed that the space created by the western façade was intended for a well, important for water provision in the shared garden. The ground in front of the well, which belongs to the building, is paved with stone. The façade of the kitchen added to the terrace in the second phase is plastered and painted, while the restroom façade is made of unplastered rubble stone.

3.4. Construction technique and material

The load-bearing stone walls that form the structural system of the main building on the ground and upper floors are original elements. The original partition walls made of wooden framework on the upper floor provide the division of rooms. The brick walls added to the service areas on the ground floor to create wet spaces, are not original. On the upper floor, the spatial organization of the master room was altered by the users, and the space was divided into two with a brick wall. The roof covering material in its original state was Ottoman-style roof tile, as determined through traces found in the building, data from written sources, and comparative studies with nearby structures. In the second phase, the kitchen and toilet added to the terrace, with a stone parapet flat roof, were identified based on oral history research and traces from the building. The ground floor is covered with mosaic tiles as per architectural requirements, and the terrace is surrounded by stone parapet. Access to this terrace was provided by a portable wooden staircase when necessary. Later, the terrace area, renovated with modern materials, now features the use of a terrace roof on a reinforced concrete floor. In this period, the ground floor is covered with ceramic tiles, and the terrace is surrounded by mosaic parapet as per architectural requirements. When the building was converted into a boutique hotel, the original roof covered with Ottoman-style roof tiles was replaced with a roof covered with Marseille tiles, with the first row still covered in Ottoman-style roof tiles on the east and north façades. Based on traces from the building, it is observed that there is eaves molding made of Ottoman-style roof tiles on the east façade. It is believed that this eaves molding continues the north and west façades, as determined through comparative studies within the building. Additionally, the iron ties found on the façades are original.

4. Conclusions

A notable example of a historical building is the two-story stone house known as “Yürük Grocery,” located in the Hacı Memiş Neighborhood of Alaçatı. Its distinctive corner position, shared courtyard design, and ground-floor commercial function distinguish it from other traditional houses in the area. This building has hosted both a non-Muslim family and a Muslim family over time and was also well-known in Alaçatı for serving as a grocery store. Its documentation is important as it reflects the integration of both cultures, providing valuable insights into the cultural dynamics of the region. The building’s historical and architectural significance is further underscored by the way it encapsulates the societal transitions of the

area. It has served as a testament to the blending of distinct communities and their lifestyles throughout different periods. This study identifies three distinct periods by examining the building's architectural features, history, construction techniques, and material characteristics throughout its evolution. It highlights the layered history of the structure, offering a glimpse into the changing socio-economic and cultural environment of Alaçatı. Although the historical building has undergone changes in its layout and additions over the years, it is clear that its front façade character, in particular, has not been lost. The careful preservation of its front elevation underscores the building's enduring cultural importance. In the second phase, the spaces added by enclosing the terrace were of low quality and diminished the spatial and cultural value of the building. Despite these alterations, the study reveals the importance of maintaining the building's authentic features to ensure its historical identity is preserved. In this way, the study not only highlights the architectural evolution of "Yürük Grocery," but also contributes to the broader understanding of preserving historical landmarks in the face of modern development, ensuring that they remain valuable cultural assets for future generations.

Authorship Contribution Statement

The author confirms sole responsibility for the following: study conception and design, data collection, analysis and interpretation of results, and manuscript preparation.

Conflict of Interest

The authors declare no conflict of interest.

References

Akbaylar, İ. (2008). *Documentation of a historical house with close range digital photogrammetry* (Master Thesis). Izmir Institute of Technology.

Aslankan, A. (2008). *Reflections of cultural capital on exchange of populations: The case of Çesme and Alaçatı* (Master Thesis). Middle East Technical University.

Atilla, A. N. & Öztüre, N. (2006). *Alaçatı / Agrilia'dan Günümüze Bir Mübadele Kasabası.* Öztüre Kültür Yayını.

Baykara, T. (1990). Çeşme Kalesi. *Belleten*, 54/210, 603-630.

Beyru, R. (2011). *19. Yüzyılda İzmir Kenti*. Literatür Yayıncılık.

Çetinel, S. (2021). *Alaçatı evlerinin cephe tipolojisi* (Expertise Thesis). Kültür ve Turizm Bakanlığı Kültür Varlıkları ve Müzeler Genel Müdürlüğü.

Hersek, C. M. (1990). Alaçatı Kasabasında Koruma ve Sağlıklaştırma. *Ankara Üniversitesi Dil ve Tarih-Coğrafya Fakültesi Dergisi*, *34* (1-2), 395-404.

Gezgin, İ. (2007). *Alacaat'tan Alaçatı'ya / Rüzgarlı Bir Köyün Hikayesi.* Sel Yayıncılık.

Kocamanoğlu, N. M. (2010). *Alaçatı 19. yy. ve 20. yy. konut mimarisi* (Master Thesis). Mimar Sinan Fine Arts University.

Özgönül, N. (1996). *A method for restructuring the interrelation between tourism and usage of traditional / historic settlements - Case study: Alaçatı* (Doctoral Thesis). Middle East Technical University.

Özgönül, N. (2010). Alaçatı'da Yaşam. *Ege Mimarlık Dergisi*, 72, 18-25.

Şimşir, N. (2018). Osmanlı Arşiv Belgelerine Göre Osmanlı Hukukunda "Paftos Meselesi" ve Sonuçları (Çeşme Kazası Örneği). *XVIII. Türk Tarih Kongresi Kongreye Sunulan Bildiriler (III. Cilt*) Osmanlı Tarihi ve Medeniyeti, Türk Tarih Kurumu, 1243-1270.

Terim, B. (2011). *Climatic considerations in traditional built environments: The effect of natural ventilation on thermal comfort in Alaçatı, İzmir, Turkey* (Doctoral Thesis). Izmir Institute of Technology.

Yılmaz, T. (1983). *17-19. yüzyıllarda Batı Anadolu'da Osmanlı-Türk şehir dokuları: Bu dokuları oluşturan evler ve korumaları* (Doctoral Thesis). Mimar Sinan Fine Arts University.

URL1: Tapu ve Kadastro Genel Müdürlüğü Parsel Sorgu Uygulaması. (Access: 15 December 2024). https://parselsorgu.tkgm.gov.tr/

URL2: Eskimeyen İzmir Fotoğrafları-Ageless Izmir Photographs. (Access: 10 December 2024). https://www.facebook.com/groups/1708798419390384/?locale=tr_TR

URL3: Alaçatı'da Hayat. (Access: 15 November 2024). https://alacatidahayat.wordpress.com/2011/02/19/sarmasik-bakkal/

Scientific Research Communications

Novel Fullerene-Based Dyes for Solar Cells Applications: Insights from Density Functional Theory and Time Dependent Density Functional Theory Investigations

Ismail Muhammad[1,2] *, Hamisu Ibrahim[2], Muhammad S. Sallau[2], Zaharaddeen N. Garba[2], Şule Erten Ela[3]

[1] Umaru Musa Yar'adua University, Ibrahim Shehu Shema Center for Renewable Energy Research, Katsina, Nigeria
[2]Ahmadu Bello University, Faculty of Physical Sciences, Chemistry Department, Zaria, Nigeria
[3]Ege University, Institute of Solar Energy, Bornova, İzmir, Türkiye

Research Article

*Correspondence: ismail.muhammad@umyu.edu.ng

Received: 20 December 2024
Accepted: 20 January 2025
Published: 24 January 2025

Keywords
Molecular design
Optimization
Fullerene
Organic dyes
TD-DFT

Abstract

Fullerene-based organic dyes hold significant promise for advancing solar cell technologies due to their exceptional optoelectronic properties. This study investigates two novel fullerene-based dyes, Fullerene Dye 1 and Fullerene Dye 2 (FD1 and FD2), using Density Functional Theory (DFT) and Time-Dependent Density Functional Theory (TD-DFT) to evaluate their potential for solar cell applications. The electronic properties, including the Highest Occupied Molecular Orbital (HOMO), Lowest Unoccupied Molecular Orbital (LUMO), and HOMO-LUMO (H-L) energy gaps, were analyzed using the B3LYP functional with a 6-31G basis set, incorporating solvation effects with dichloromethane (DCM) in the Polarizable Continuum Model (PCM). FD1 exhibited a HOMO of -5.123 eV, a LUMO of -3.458 eV, and an H-L gap of 1.665 eV, while FD2 showed a slightly larger gap of 1.807 eV with a HOMO of -5.261 eV and a LUMO of -3.454 eV. Time-dependent DFT analysis revealed maximum absorption wavelengths (λmax) of 997.10 nm and 995.16 nm for FD1 and FD2, respectively, with corresponding oscillator strengths of 0.0075 and 0.0048. The light-harvesting efficiencies, LHEs of FD1 and FD2 were 0.018 and 0.012, respectively. Both dyes demonstrated favorable reorganization energy, λ=0.15eV, driving force for charge injection, ΔG_{inj} = 0.542eV for FD1 and 0.546 eV for FD2, and low driving force for charge recombination (ΔG_{CR}), indicating strong potential for efficient charge separation. These findings provide valuable insights into the electronic, optical, and charge transfer properties of fullerene-based dyes, with FD1 exhibiting a more balanced performance. The study highlights the potential of these dyes for enhancing the efficiencies of organic, dye-sensitized solar cells (DSSCs) and provides a foundation for future experimental validation and optimization.

How to cite this paper: Muhammad, I., Ibrahim, H., Sallau, M. S., Garba, Z. N., & Erten Ela, Ş. (2025). Novel fullerene-based dyes for solar cell applications: Insights from density functional theory and time-dependent density functional theory investigations. *Scientific Research Communications*, *5*(1), 28-38. https://doi.org/10.52460/src.2025.03

1. Introduction

The exploration of fullerene-based organic dyes for solar cell applications has garnered significant attention in recent years, primarily due to their unique electronic properties and potential for enhancing photovoltaic efficiency. Fullerenes, a class of carbon allotropes, exhibit remarkable light absorption characteristics and electron-accepting capabilities, making them ideal candidates for use in organic solar cells. The theoretical modeling of these materials, particularly through DFT and TD-DFT, has emerged as a crucial approach in understanding and optimizing their performance in solar energy conversion systems (Babu, 2022). DFT and TD-DFT provide insights into the electronic structure, optical properties, and charge transfer dynamics of fullerene-based dyes, thereby facilitating the design of more efficient organic solar cells. Recent advancements in computational methods have significantly enhanced our ability to model the optoelectronic properties of fullerene derivatives. For instance, studies have demonstrated that DFT can effectively predict the electronic band structure and optical absorption spectra of various fullerene compounds, enabling researchers to identify promising candidates for solar cell applications (Fuhrer et al., 2020). The ability to simulate the interactions between fullerene-based dyes and semiconductor materials further allows for the optimization of charge transfer processes, which are critical for improving the overall efficiency of organic solar cells (Kim and Kim, 2012), (Ku et al., 2011). Moreover, the integration of TD-DFT in these studies provides a dynamic view of excited-state properties, essential for understanding the photophysical behavior of these materials under solar irradiation (Labat et al., 2012).

The role of fullerene-based dyes in enhancing the performance of organic solar cells cannot be overstated. Their incorporation into bulk heterojunction (BHJ) architectures has been shown to improve exciton dissociation and charge transport, leading to higher power conversion efficiencies (Paul and Birol, 2019), (Petrus et al., 2017). The unique structural characteristics of fullerenes, such as their spherical shape and conjugated π-systems, contribute to their effectiveness as electron acceptors in DSSCs (Sahoo et al., 2022; Tamighang, 2023). Furthermore, the development of novel fullerene derivatives through synthetic chemistry has opened new avenues for tailoring their electronic properties to meet specific application requirements (Fuhrer et al., 2020), (Sahoo et al., 2022). In addition to their promising optoelectronic properties, the stability and environmental compatibility of fullerene-based organic dyes are critical factors influencing their practical application in solar cells. Recent studies have focused on the stability of these materials under operational conditions, highlighting the importance of molecular design in mitigating degradation pathways (Zhu et al., 2020), (Petrus et al., 2017). The theoretical insights gained from DFT and TD-DFT calculations play a pivotal role in guiding the synthesis of more robust fullerene derivatives that maintain their performance over extended periods (Tamighang, 2023).

The future of fullerene-based organic dyes in solar cell applications appears promising, with ongoing research aimed at further enhancing their efficiency and stability. The integration of advanced computational techniques, such as machine learning and multi-scale modeling, alongside DFT and TD-DFT, is expected to accelerate the discovery of new materials and optimize existing ones (Paul and Birol, 2019). As the demand for renewable energy sources continues to grow, the development of efficient and sustainable solar cell technologies will rely heavily on the insights provided by theoretical modeling of materials like fullerene-based organic dyes.

The advances in theoretical modeling of fullerene-based organic dyes for solar cell applications represent a significant stride towards optimizing photovoltaic technologies. The application of DFT and TD-DFT has proven invaluable in elucidating the electronic and optical properties of these materials, paving the way for the design of high-performance organic solar cells. As research progresses, the continued exploration of fullerene derivatives and their integration

into solar cell architectures will be essential for achieving the next generation of efficient and sustainable energy solutions. Conducting DFT and TD-DFT analyses before synthesizing light-absorbing dyes for application in solar cells is essential to ensure the efficient use of resources and minimize chemicals waste. In this study, we explore the key electronic and optical properties of fullerene-based dyes that make them suitable candidates for solar cell applications, as revealed by theoretical modeling using DFT and TD-DFT.

The methodological approach used in this research distinguishes it from existing literatures, which often neglects the impact of solvation on electronic properties. The quantitative insights provided by this study, including the HOMO-LUMO energy levels, absorption wavelengths, oscillator strengths, and light-harvesting efficiencies, are crucial for understanding the performance of FD1 and FD2 in DSSCs. The HOMO-LUMO gap is a vital parameter that influences the light absorption capabilities and charge transfer efficiency of the dyes (Sutradhar and Misra, 2019), (Ji et al., 2022). Additionally, the study discusses critical parameters such as reorganization energy and the driving forces for charge injection and recombination, which are essential for evaluating the operational efficiency of the dyes in solar cells (Wang et al., 2013), (Kavitha et al., 2017). The balance between light absorption, charge transfer, and recombination resistance is particularly emphasized, with FD1 demonstrating superior performance metrics compared to FD2, which aligns with findings in the literature that highlight the importance of optimizing these parameters for enhanced photovoltaic efficiency (Karthikeyan and Lee, 2013), (Ren and Zhang, 2015). Moreover, this research bridges the gap between theoretical insights and practical photovoltaic applications, paving the way for experimental validation and optimization of DSSCs. The direct correlation between computational predictions and experimental outcomes is a significant contribution to the field, as it facilitates the design of more efficient dye sensitizers (Li, 2012). By linking quantum chemistry with renewable energy innovation, the study not only enhances the understanding of dye performance mechanisms but also contributes to the ongoing development of sustainable energy technologies.

2. Materials and Methods

All calculations were performed using the Gaussian 09 software package. DFT and TD-DFT were employed for the electronic structure and optical property investigations.

2.1. Design of organic photosensitizers

The design of two organic photosensitizers, FD1 and FD2, was systematically carried out to incorporate key functional components: fullerene as the acceptor, ethyl hexyl groups for stability, a TPD (triphenylamine derivative) as the π-bridge, and cyanoacrylic acid groups for anchoring to TiO_2. This approach was guided by the design principles outlined by Kim and Kim (2012), emphasizing the specific functional roles of each moiety to enhance the photosensitizer's overall performance. The schematic of the design process is shown in Figure 1, while the resulting photosensitizer dyes are depicted in Figure 2.

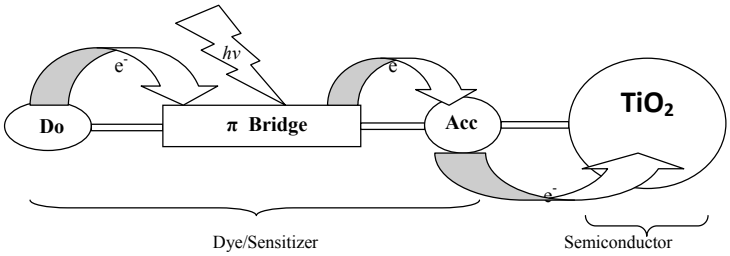

Figure 1. Design principle of photosensitizer dye

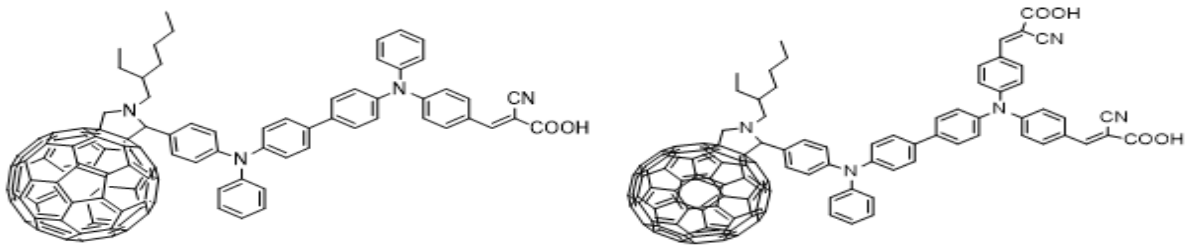

FD1 FD2

Figure 2. Design fullerene dyes

2.2. Computational details

The methodology used for studying the two fullerene-based dyes (FD1 and FD2) involved a step-by-step approach to ensure accurate analysis of their structural and electronic properties. First, the ground-state geometries of the dyes were optimized using the B3LYP functional, which combines Becke's three-parameter nonlocal-exchange functional with the Lee–Yang–Parr correlation method, along with a 6-31G (d) basis set for all atoms (Mennucci, 2012). To verify that these optimized geometries represented true energy minima, frequency calculations were performed at the same level of theory, ensuring the absence of imaginary frequencies and confirming the stability of the structures (Skora et al., 2014). Next, the solvent effects were considered by analyzing the geometries in DCM using the PCM at the same B3LYP/6-31G (d) level, which accounts for the influence of the solvent environment (Mennucci, 2012). Finally, the UV-visible absorption properties of the dyes were investigated using TD-DFT with the CAM-B3LYP functional. This approach provided more accurate predictions of excitation energies and absorption spectra (Guido et al., 2015).

3. Results and Discussions

3.1. Photosensitizer design

Figure 1 displays the structures of a novel category of dyes FD1 and FD2. These dyes were designed with specific molecular components to enhance their functionality. Fullerene was introduced as an electron acceptor due to its excellent electron mobility and ability to stabilize charge-separated states. Its incorporation aimed to enhance the electron transport and overall efficiency of the dye-sensitized system. (Paul et al., 2020). The introduction of ethyl hexyl groups improves solubility and film-forming properties while minimizing dye aggregation, thus promoting stability and performance (Majid et al., 2020). TPD serves as the electron donor, characterized by high hole mobility, facilitating charge transfer and ensuring robust interactions with both the fullerene acceptor and the anchoring group (Saccone et al., 2016). Cyanoacrylic acid acts as an anchoring group, providing strong binding to semiconductor surfaces like TiO_2, while its electron-withdrawing nature enhances charge injection efficiency (Movahedi et al., 2019). This structural design optimizes light absorption, charge transport, and dye-semiconductor interactions, which are crucial for maximizing the performance of organic photosensitizers in photovoltaic applications (Xie et al., 2022). Figure 3 shows the optimized 3D structures of the dyes prior to DFT and TD-DFT.

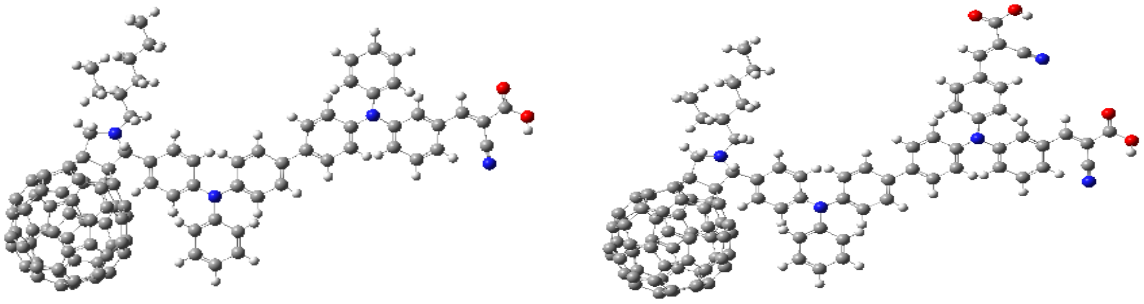

Figure 3. Optimized geometries of dyes FD1 and FD2. Gray, white, blue, red, colors represents carbon atom, hydrogen atom, nitrogen atom and, oxygen atom, respectively.

3.2. Electronic properties

Figures 4 and 5 illustrate the distributions of the HOMO and the LUMO for fullerene dyes FD1 and FD2, where fullerene acts as a strong electron acceptor. In both systems, the HOMO is predominantly localized on the donor group, while the LUMO is primarily concentrated on the fullerene. This spatial arrangement indicates effective charge separation, as electrons move from the donor to the fullerene upon excitation. The presence of cyanoacrylic acid as the anchoring group enhances this electron transfer by withdrawing electron density from the donor and facilitating its flow toward the fullerene. The electron-withdrawing nature of cyanoacrylic acid improves the coupling between the donor and fullerene, enabling efficient charge transfer. Fullerene's high electron affinity and ability to stabilize delocalized electrons further contribute to its role as a strong acceptor. Regardless of whether one (FD1) or two (FD2) cyanoacrylic acid groups are used, the LUMO remains primarily localized on the fullerene, indicating that nearly all transferred electrons are stabilized there. This highlights fullerene's dominant role in driving electron transfer and maintaining charge separation, making it an excellent component in donor-acceptor systems.

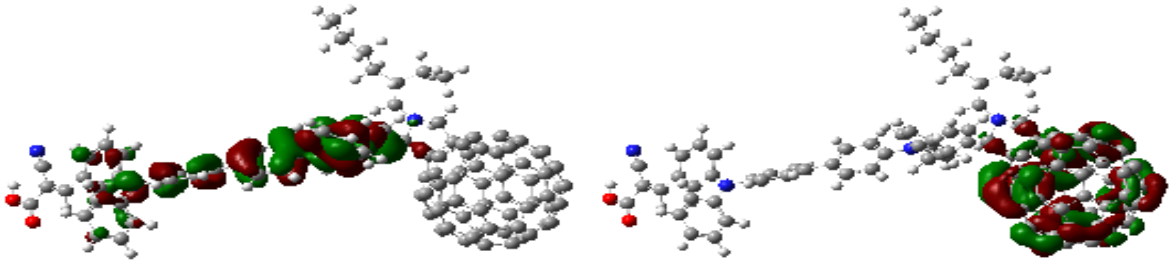

Figure 4. FD1 HOMO (Left) and LUMO (Right)

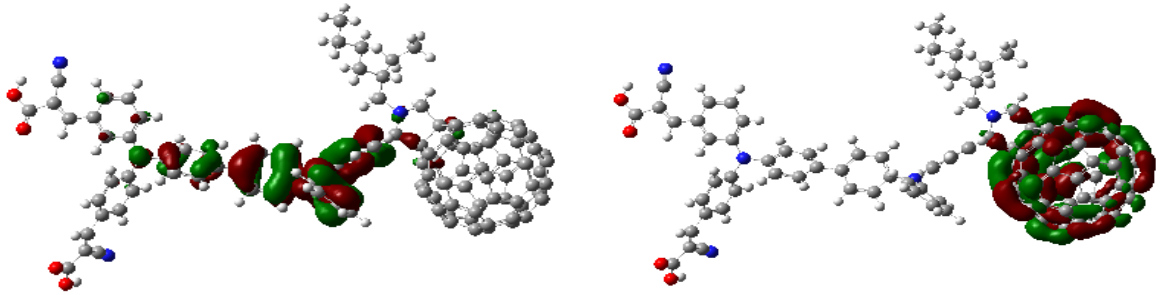

Figure 5. FD2-HOMO (Left) and LUMO (Right)

3.3. Energy levels

The data presented in Table 1 and Figure 6 illustrates the energy levels of the HOMO and LUMO for the two different dyes. The energy levels of the HOMO and the LUMO are critical in determining the charge transfer capabilities of DSSCs. The HOMO energy levels of FD1 (-5.123 eV) and FD2 (-5.261 eV) indicate that FD1 has a higher oxidation potential, suggesting a better capacity for charge donation during regeneration by the redox mediator. Both dyes exhibit LUMO levels (-3.458 eV for FD1 and -3.454 eV for FD2) that are favorable for electron injection into the conduction band of titanium dioxide (TiO_2), which is positioned at approximately -4.0 eV (Yang et al., 2015). The smaller HOMO-LUMO gap (H-Lgap) of FD1 (1.665 eV) compared to FD2 (1.807 eV) implies enhanced light absorption and electron transfer efficiency, making FD1 more advantageous for DSSC applications (Wei et al., 2015). The structural variations, particularly the number of cyanoacrylic acid groups, significantly influence the electronic properties, highlighting the importance of chemical design in optimizing dye performance (Ji et al., 2012).

Table 1. Simulated and calculated parameters of the dyes

Dyes	HOMO (eV)	LUMO (eV)	H-L gap (eV)	λ_{max} (nm)	f	LHE	λ (eV)	ΔG_{inj} (eV)	ΔG_{CR} (eV)
FD1	-5.123	-3.458	1.665	997.10	0.0075	0.018	0.15	0.542	1.665
FD2	-5.261	-3.454	1.807	995.16	0.0048	0.012	0.15	0.546	1.807

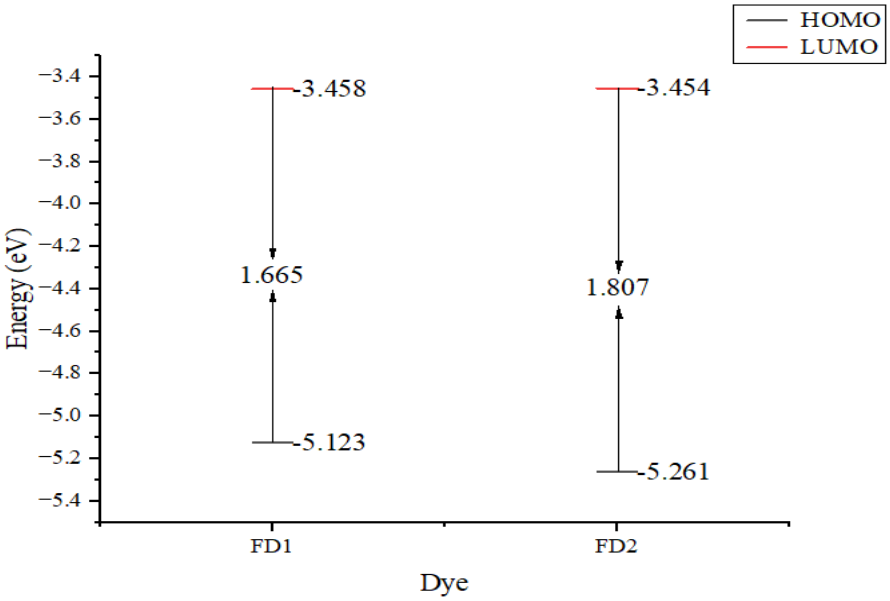

Figure 6. Energy band gaps of the dyes

3.4. Absorption spectra

The UV-Vis spectra of fullerene dyes FD1 and FD2 in Table 1 and Figure 7 reveal absorption peaks in the near-infrared (NIR) region, specifically at 997 nm for FD1 and 995 nm for FD2. Notably, FD1 demonstrates a higher absorption intensity compared to FD2, correlating with their respective molar extinction coefficients (f-values) of 0.0075 for FD1 and 0.0048 for FD2. These low f-values indicate that both dyes exhibit relatively weak electronic transitions, which

is characteristic of fullerene-based compounds (Chen et al., 2012). The absorption peaks in the NIR region suggest potential applications in optoelectronic devices and photovoltaic systems, particularly for solar energy harvesting, where strong electron-accepting properties are advantageous (Zhang et al., 2017). The slight difference in peak wavelengths may be attributed to minor structural variations affecting electronic transitions (Vitnik et al., 2017). Overall, the UV-Vis data indicate that FD1 and FD2 are promising candidates for applications requiring efficient light absorption and electron transfer, with FD1 showing slightly superior performance (Zatsikha et al., 2019).

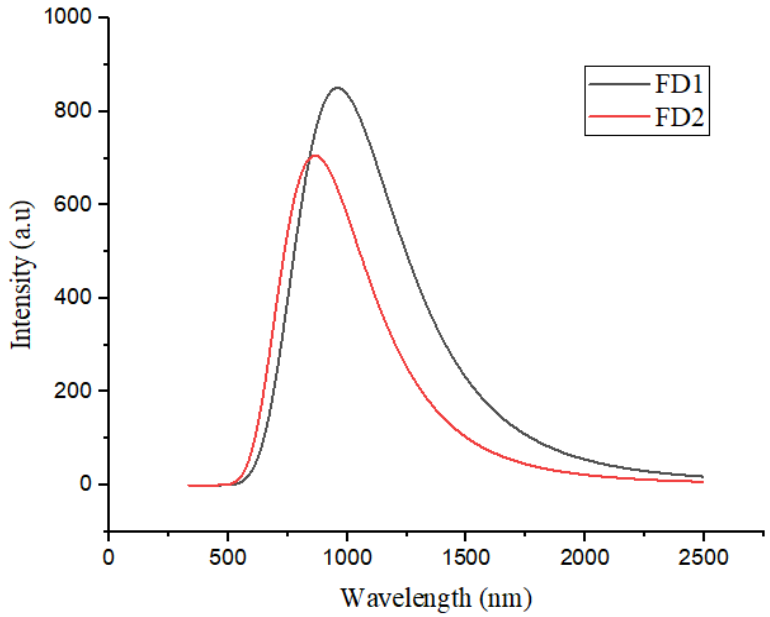

Figure 7. Theoretical UV- Vis of Dyes

3.5. Light Harvesting Efficiency (LHE), Reorganization Energy (λ), Driving Force for Charge Injection (ΔG_{inj}) and Recombination (ΔG_{CR})

LHE was calculated using the formula:

$$LHE = 1 - 10^{-f} \quad (1)$$

where f is the oscillator strength of the dye.

The FD1 outperforms FD2 in LHE, with values of 0.018 and 0.012, respectively. While these values are low due to small oscillator strengths, FD1's higher LHE suggests better light absorption (Griffith et al., 2012).

λ was typically calculated using:

$$\lambda = \lambda_{internal} + \lambda_{external} \quad (2)$$

We assume that $\lambda_{external}$ is negligible, and the internal component depends on molecular-level calculations of geometry and energy. We can assume a plausible range based on literature values for fullerene-based dyes, $\lambda_{internal}$~0.1−0.2eV (Selim and Mohamed, 2017).Both dyes demonstrate low reorganization energy λ=0.15eV, which is favorable for efficient charge transfer, minimizing energy losses during electron injection into the TiO_2 conduction band (Brauer et al., 2015).

ΔG_{inj} was calculated as:

$$\Delta Ginj = E_{LUMO}^{Dye} - E_{CB}^{TiO2} \quad (3)$$

Here, conduction band edge of TiO_2 is typically around −4.0eV.

In terms of charge injection; both dyes exhibit thermodynamically favorable values, with FD1 at 0.542 eV and FD2 slightly higher at 0.546 eV, indicating efficient electron transfer (Imahori et al., 2010).

ΔG_{CR} was calculated as:

$$\Delta GCR = E_{LUMO}^{Dye} - E_{HOMO}^{Dye} \quad (4)$$

However, FD1 has a lower driving force for charge recombination ΔG_{CR}=1.665 eV compared to FD2, 1.807eV. This suggests FD1 is less prone to back-electron transfer, a critical factor for maintaining high photocurrents and overall device efficiency (Selim and Mohamed, 2017).

4. Conclusions

This study explores the potential of two novel fullerene-based dyes, FD1 and FD2, for application in DSSCs through comprehensive computational analysis using DFT and TD-DFT methodologies. The findings underscore the exceptional optoelectronic properties of these dyes, particularly their efficient charge separation and favorable energy parameters. FD1, with its balanced H-L gap, strong light-harvesting efficiency, and optimal driving forces for charge injection and recombination, demonstrates slightly superior performance metrics compared to FD2. These insights not only affirm the viability of fullerene-based dyes in advancing solar cell technologies but also establish a robust foundation for further experimental validation and material optimization. By addressing the intricate interplay between electronic, optical, and charge transfer properties, this work contributes significantly to the design and development of next-generation organic and dye sensitized solar cells materials. Future studies should focus on experimental synthesis and testing to validate and refine these computational predictions, paving the way for real-world applications.

Authorship Contribution Statement

Each author contributed significantly to the study. IM and ŞEE: study conception and design; IM, HI, MSS and ZNG analysis and interpretation of results. All authors reviewed the results and approved the final version of the manuscript.

Conflict of Interest

The authors declare no conflict of interest.

References

Babu, N. (2022). *Applications of current density functional theory (DFT) methods in polymer solar cells*. IntechOpen. https://doi.org/10.5772/intechopen.100136

Brauer, J., Marchioro, A., Paraecattil, A., Oskouei, A., & Moser, J. (2015). Dynamics of interfacial charge transfer states and carrier separation in dye-sensitized solar cells: A time-resolved terahertz spectroscopy study. *The Journal of Physical Chemistry C, 119*(47), 26266–26274. https://doi.org/10.1021/acs.jpcc.5b06911

Chen, N., Beavers, C., Mulet-Gas, M., Rodríguez-Fortea, A., Munoz, E., Li, Y., & Echegoyen, L. (2012). Sc_2S@Cs(10528)-C_{72}: A dimetallic sulfide endohedral fullerene with a non-

isolated pentagon rule cage. *Journal of the American Chemical Society, 134*(18), 7851–7860. https://doi.org/10.1021/ja300765z

Fuhrer, T., Snelgrove, J., Corley, C., & Iacono, S. (2020). Density functional theory investigation of fulvene-derivatized fullerenes as candidates for organic solar cells. *The Journal of Physical Chemistry A, 124*(49), 10324–10329. https://doi.org/10.1021/acs.jpca.0c06469

Griffith, M., Sunahara, K., Wagner, P., Wagner, K., Wallace, G., Officer, D., & Mozer, A. (2012). Porphyrins for dye-sensitised solar cells: New insights into efficiency-determining electron transfer steps. *Chemical Communications, 48*(35), 4145. https://doi.org/10.1039/c2cc30677h

Guido, C., Jacquemin, D., Adamo, C., & Mennucci, B. (2015). Electronic excitations in solution: The interplay between state-specific approaches and a time-dependent density functional theory description. *Journal of Chemical Theory and Computation, 11*(12), 5782–5790. https://doi.org/10.1021/acs.jctc.5b00679

Imahori, H., Yusuke, M., Hiroaki, I., Tomokazu, U., Yoshihiro, M., Seigo, I., Marja, N., Nikolai, V. T., & Helge, L. (2010). Effects of *meso*-diarylamino group of porphyrins as sensitizers in dye-sensitized solar cells on optical, electrochemical, and photovoltaic properties. *The Journal of Physical Chemistry C, 114*(23), 10656–10665. https://doi.org/10.1021/jp102486b

Ji, J., Lee, H., Zhou, H., Eom, Y., Kim, C., & Kim, H. (2022). Influence of the π-bridge-fused ring and acceptor unit extension in d−π–a-structured organic dyes for highly efficient dye-sensitized solar cells. *ACS Applied Materials & Interfaces, 14*(47), 52745–52757. https://doi.org/10.1021/acsami.2c13331

Ji, Z., Li, H., Sun, S., Geng, Y., Wu, Y., & Su, Z. (2012). Density functional theory characterization and design of high-performance diarylamine-fluorene dyes with different π spacers for dye-sensitized solar cells. *Journal of Materials Chemistry, 22*(2), 568–576. https://doi.org/10.1039/c1jm13028e

Karthikeyan, S., & Lee, J. (2013). Zinc-porphyrin based dyes for dye-sensitized solar cells. *The Journal of Physical Chemistry A, 117*(42), 10973–10979. https://doi.org/10.1021/jp408473k

Kavitha, S., Praveena, K., & Lakshmi, M. (2017). A new method to evaluate the feasibility of a dye in DSSCs application. *International Journal of Energy Research, 41*(14), 2173–2183. https://doi.org/10.1002/er.3778

Kim, J., & Kim, Y. (2012). Molecular design and computation of dye sensitizers with multiple electron donor for DSSC. *Molecular Crystals and Liquid Crystals, 567*(1), 71–77. https://doi.org/10.1080/15421406.2012.702393

Ku, J., Lansac, Y., & Jang, Y. (2011). Time-dependent density functional theory study on benzothiadiazole-based low-band-gap fused-ring copolymers for organic solar cell applications. *The Journal of Physical Chemistry C, 115*(43), 21508–21516. https://doi.org/10.1021/jp2062207

Labat, F., Bahers, T., Ciofini, I., & Adamo, C. (2012). First-principles modeling of dye-sensitized solar cells: Challenges and perspectives. *Accounts of Chemical Research, 45*(8), 1268–1277. https://doi.org/10.1021/ar200327w

Li, Y. (2012). Molecular design of photovoltaic materials for polymer solar cells: Toward suitable electronic energy levels and broad absorption. *Accounts of Chemical Research, 45*(5), 723–733. https://doi.org/10.1021/ar2002446

Majid, A., Sana, M., Khan, S., & Ahmad, N. (2020). Time-dependent density functional theory investigations on structural modification in carbazole-based organic photosensitizers to improve electron injection in dye-sensitized solar cell. *International Journal of Quantum Chemistry, 120*(15). https://doi.org/10.1002/qua.26253

Mennucci, B. (2012). Polarizable continuum model. *Wiley Interdisciplinary Reviews: Computational Molecular Science, 2*(3), 386–404. https://doi.org/10.1002/wcms.1086

Movahedi, J., Haratizadeh, H., Falah, N., & Hosseinnezhad, M. (2019). Investigation of effect of thiophene-2-acetic acid as an electron anchoring group for a photovoltaic device. *Opto-Electronics Review, 27*(4), 334–338. https://doi.org/10.1016/j.opelre.2019.11.001

Paul, A., & Birol, T. (2019). Applications of DFT + DMFT in materials science. *Annual Review of Materials Science, 49*(1), 31–52. https://doi.org/10.1146/annurev-matsci-070218-121825

Paul, D., Dua, H., & Sarkar, U. (2020). Confinement effects of a noble gas dimer inside a fullerene cage: Can it be used as an acceptor in a DSSC? *Frontiers in Chemistry, 8*. https://doi.org/10.3389/fchem.2020.00621

Petrus, M., Schlipf, J., Cheng, L., Gujar, T., Giesbrecht, N., Müller-Buschbaum, P., & Docampo, P. (2017). Capturing the sun: A review of the challenges and perspectives of perovskite solar cells. *Advanced Energy Materials, 7*(16). https://doi.org/10.1002/aenm.201700264

Ren, X., & Zhang, J. (2015). Theoretical studies of electronic structure and photophysical properties of a series of indoline dyes with triphenylamine ligand. *Journal of Nanomaterials, 2015*(1). https://doi.org/10.1155/2015/605728

Saccone, D., Galliano, S., Barbero, N., Quagliotto, P., Viscardi, G., & Barolo, C. (2016). Polymethine dyes in hybrid photovoltaics: Structure–properties relationships. *European Journal of Organic Chemistry, 2016*(13), 2244–2259. https://doi.org/10.1002/ejoc.201501598

Selim, Y., & Mohamed, A. (2017). Role of dyestuff in improving dye-sensitized solar cell performance. *Renewable Energy and Sustainable Development, 3*(1), 79–82. https://doi.org/10.21622/resd.2017.03.1.079

Sahoo, S., Murmu, M., Banerjee, P., Pathan, H., & Salunke-Gawali, S. (2022). Tailoring benzo[α]phenoxazine moiety for efficient photosensitizers in dye-sensitized solar cells via the DFT/TD-DFT method. *New Journal of Chemistry, 46*(31), 15155–15167. https://doi.org/10.1039/d2nj02589b

Škorňa, P., Rimarčík, J., & Klein, E. (2014). Solvation enthalpies of the electron in polar and non-polar solvents: Theoretical study. *Acta Chimica Slovaca, 7*(1), 31–33. https://doi.org/10.2478/acs-2014-0006

Sutradhar, T., & Misra, A. (2019). Enhancement of nonlinear optical properties of indole-based dyes through electron acceptor and π-linker for dye-sensitized solar cell applications. *ChemistrySelect, 4*(13), 3697–3705. https://doi.org/10.1002/slct.201803992

Tamighang, R. (2023). A DFT and TD-DFT study of two hydralazine derivatives for organic solar cells and nonlinear optical applications. *Journal of Chemistry*, 1–12. https://doi.org/10.1155/2023/2162991

Vitnik, V., Vitnik, Ž., Božić, B., Valentić, N., Dilber, S., Mijin, D., & Uščumlić, G. (2017). Experimental and theoretical insight into the electronic properties of 4-aryl-5-arylazo-3-cyano-6-hydroxy-2-pyridone dyes. *Coloration Technology, 133*(3), 223–233. https://doi.org/10.1111/cote.12271

Wang, J., Cong, S., Wen, S., Yan, L., & Su, Z. (2013). A rational design for dye sensitizer: Density functional theory study on the electronic absorption spectra of organoimido-substituted hexamolybdates. *The Journal of Physical Chemistry C, 117*(5), 2245–2251. https://doi.org/10.1021/jp3106452

Wei, T., Sun, X., Li, X., Ågren, H., & Xie, Y. (2015). Systematic investigations on the roles of the electron acceptor and neighboring ethynylene moiety in porphyrins for dye-sensitized solar cells. *ACS Applied Materials & Interfaces, 7*(39), 21956–21965. https://doi.org/10.1021/acsami.5b06610

Xie, X., Zhang, Y., Ren, Y., He, L., Yuan, Y., Zhang, J., & Wang, P. (2022). Semitransparent dye-sensitized solar cell with 11% efficiency and photothermal stability. *The Journal of Physical Chemistry C, 126*(27), 11007–11015. https://doi.org/10.1021/acs.jpcc.2c03162

Yang, Z., Liu, C., Shao, C., Chen, L., & Liu, Y. (2015). First-principles screening and design of novel triphenylamine-based d−π–a organic dyes for highly efficient dye-sensitized solar cells. *The Journal of Physical Chemistry C, 119*(38), 21852–21859. https://doi.org/10.1021/acs.jpcc.5b0574

Zatsikha, Y., Swedin, R., Healy, A., Goff, P., Didukh, N., Blesener, T., & Nemykin, V. (2019). Synthesis, characterization, and electron-transfer properties of ferrocene–bodipy–fullerene near-infrared-absorbing triads: Are catecholopyrrolidine-linked fullerenes a good architecture to facilitate electron-transfer? *Chemistry - A European Journal, 25*(35), 8401–8414. https://doi.org/10.1002/chem.201901225

Zhang, X., Jia, Y., Zhao, D., Gou, F., Gao, H., Xu, C., & Jing, H. (2017). Substituted and anchoring groups improve the efficiency of dye-sensitized solar cells. *ChemistrySelect, 2*(14), 4084–4091. https://doi.org/10.1002/slct.201700494

Zhu, W., Spencer, A., Mukherjee, S., Alzola, J., Sangwan, V., Amsterdam, S., & Marks, T. (2020). Crystallography, morphology, electronic structure, and transport in non-fullerene/non-indacenodithienothiophene polymer: Y6 solar cells. *Journal of the American Chemical Society, 142*(34), 14532–14547. https://doi.org/10.1021/jacs.0c05560

Zou, X., Wen, G., Hu, R., Dong, G., Zhang, C., Zhang, W., & Dang, W. (2020). An insight into the excitation states of small molecular semiconductor Y6. *Molecules, 25*(18), 4118. https://doi.org/10.3390/molecules25184118

Scientific Research Communications

New Amperometric Glucose Biosensors Based On Nafion Nanofibers

Sawssen Ghannouchi*, Elif Merve Özer, Pınar Çamurlu

Akdeniz University, Department of Chemistry, Antalya, Türkiye

Research Article

*Correspondence:
sawssen.sawssen24@gmail.com

Received: 12 December 2024
Accepted: 18 January 2025
Published: 24 January 2025

Keywords
Amperometric biosensor
Electrospinning
Gold nanoparticles
Glucose oxidase
Nafion
Nanofiber

Abstract

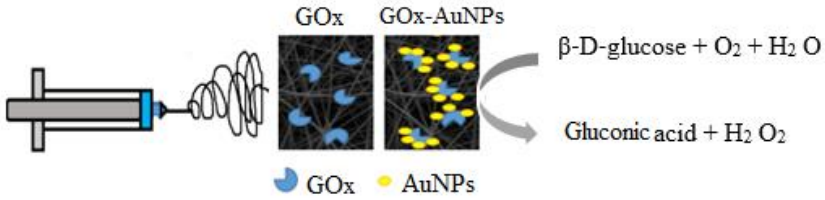

In this study, we present new amperometric glucose biosensors based on Nafion nanofibers. Nafion possesses a number of desirable properties, including stability, thermal, mechanical, physio-chemical and biocompatibility, which make it a competitive polymer for use in glucose biosensors. Nafion nanofibers were produced using a low-cost electrospinning method, and their morphology was characterized via scanning electron microscopy (SEM). The biosensors were fabricated by loading glucose oxidase (GOx) and GOx-AuNPs (10 nm) on the Nafion-Cellulose Acetate nanofibers (Nafion-CA Nfs) (461.53 ± 30.34 nm) on the surface of a platinum electrode, followed by cross-linking using glutaraldehyde. The biosensors operating at 0.6 V demonstrated lower LODs with wider linear ranges, enhanced stability, elevated sensitivity, and improved selectivity. For Pt/Nafion-CA NFs/GOx biosensor demonstrated remarkable sensitivity, with values of 68.67 $\mu A.mM^{-1}cm^{-2}$ and 18.38 $\mu A.mM^{-1}.cm^{-2}$, respectively, and a limit of detection (LOD) of 1.36 µM. Meanwhile, the Pt/Nafion-CA NFs/ GOx-AuNPs biosensor achieved sensitivities of 55.56 µA.mM-1.cm² and 28.49 µA/mM ·cm², respectively. It also exhibited a broad linear range of up to 12.81 mM and an LOD of 10.8 µM, with no observable interference effects. The present studies highlight the potential of Nafion nanofibers as a suitable matrix for immobilizing GOx and GOx-AuNPs, thereby demonstrating their viability as interference-free, easy-to-use sensors with good sensitivity, LOD and stability for commercialization.

1. Introduction

Nanofibers (NFs) and nanoparticles (NPs) represent the fundamental building blocks of nanotechnology. Nanofibers exhibit a range of morphologies, with diameters spanning from micrometers to hundreds of nanometers and lengths that can extend to several meters. Nanofibers have been produced by a number of different processing techniques, including

How to cite this paper: Ghannouchi, S., Özer, E. M., & Çamurlu, P. (2025). New amperometric glucose biosensors based on Nafion nanofibers. *Scientific Research Communications*, *5*(1), 39–58. https://doi.org/10.52460/src.2025.004

drawing (Ondarcuhu et al., 1998), template synthesis (Feng et al., 2002; Martin, 1996), phase separation (Ma and Zhang, 1999), self-assembly (Liu et al., 1999; Whitesides and Grzybowski, 2002) and electrospinning (Deitzel et al., 2001; Islam et al., 2019). The history of electrospinning (ES) as a scientific technique spans approximately one century, it is only in recent decades that this process has gained popularity in both academic and industrial contexts (Nascimento et al., 2015). ES has proven to be a simple, versatile, and low-cost approach to fabricating electrospun nanofibers using a range of materials, including natural and synthetic polymers, liquid crystals, solid particle suspensions, ceramics, and emulsions (Pakravan et al., 2011).

Nanofibers have attracted considerable interest from a number of academic disciplines for a multitude of applications, including regenerative medicine and tissue engineering (Schiller and Scheibel, 2024; Guarino et al., 2018), drug delivery (Muratoglu et al., 2024; Ozkizilcik et al., 2018), sensors (Shooshtari, 2025; Yıldız et al., 2024; Liu et al., 2018), power generation and energy storage (Sarangika, et al., 2024; Yuriar-Arredondo et al., 2018), filtration (Akduman, 2021; Feng et al., 2024), catalysis (Din et al 2018; Gupta et al., 2018), textiles (Barhoum et al., 2018; Yan et al., 2023), defense and security (Suja and Mathiya, 2024 ; Mondal et al., 2023).

The excellent properties of these nanofibers, including straightforward production process control, a large surface area (Wang et al., 2021; Zhang et al., 2023), flexible surface characteristics, a small and adjustable pore size, high and interconnected porosity (Yue et al., 2024), intrinsic 3D topography and superior mechanical properties (Zhao et al., 2023), high bio-immobilization activity (Smith et al., 2020) and faster electron transfer compared to nanoparticle-based films of the same material, make them highly versatile and valuable materials (Choi et al., 2023; Vargas-Molinero et al., 2023).

Nanoparticles have been described as “breakthrough materials”. The material offers a vast surface area within the constraints of the nanoscale, providing an optimal platform for a multitude of chemical and biological detection applications, including drug delivery, biolabeling, protein detection, gene delivery, and body probing. Furthermore, DNA, molecule purification (Hynes et al., 2021), and the potential to address numerous health concerns are additional areas of interest. A substantial body of research has been conducted to develop nanoparticles comprising noble metals (e.g., gold, silver, platinum, and palladium), oxides (e.g., copper oxide, copper oxide, nickel oxide, and iron oxide), and bimetallic systems (e.g., gold-platinum and copper-silver) for use in biological, medical, and biosensing applications (Lipińska et al., 2021).

At present, gold nanoparticles (AuNPs) are the subject of considerable interest in the field of glucose biosensors, largely due to the favorable characteristics they possess. These include the capacity to be modified by altering their shape, size, aggregation, and surface electron enrichment, which collectively affords a large specific surface area and a conducting label for the detection of the target. Furthermore, it facilitates a specific modification of the electrode surface, resulting in a notable enhancement of the response current. AuNPs exhibit a strong interaction with various functional groups, including amino acids in the outer and exposed areas of proteins. This interaction occurs through the binding of the AuNPs to the sulfhydryl (SH) group of cysteine (Maguteeswaran et al., 2024), as well as its oxidized S–S cystine group (Shokri et al., 2017). Additionally, AuNPs can interact with CH– NH groups (Lyu et al., 2024; Hernández et al., 2018), such as those found in amino acids. Additionally, the NH groups (Hernández et al., 2018; Dadadzhanov et al., 2020), carboxylates (Courrol and Matos, 2016), glutamic and aspartic acids have the capacity to regulate the negatively charged glucose oxidase (GOx), and there are π interactions between the aromatic rings of phenylalanine and tyrosine (Roy, 2017). Furthermore, the impact of AuNPs on the enzymatic activity of GOx has been meticulously examined, along with the dimensions and expansion of AuNPs in the oxidation of glucose catalyzed by the GOx enzyme (Guo et al., 2023; Ramanavicius et al., 2017). Glucose oxidase is an enzyme that is widely employed in the design of biosensors for the

detection of glucose in the blood of diabetic patients and in the food industry. It exhibits relatively high stability, catalytic turnover, and specificity (Tu et al., 2019). It has been demonstrated that the enzyme can maintain its activity within a pH range of between 2 and 8, depending on the strain of origin and the extent to which it can be immobilized on solid surfaces (Hecht et al., 1993; Yan et al., 2022), allowing it to bind and spread. The enzyme is a homodimer, comprising two flavin adenine dinucleotide (FAD) cofactors (Samukaite-Bubniene et al., 2020; Tu et al., 2024) which catalyze the reduction of molecular oxygen through the oxidation of β-D-glucose to form hydrogen peroxide and gluconic acid.

$$\beta\text{-D-glucose} + O_2 + H_2O \rightarrow \text{gluconic acid} + H_2O_2$$

Among the materials explored to optimize glucose oxidase immobilization and activity, Nafion has emerged as a critical component due to its unique chemical and physical characteristics.

Nafion is a perfluorinated anionic polymer that exhibits excellent biocompatibility, thermal, mechanical and chemical stability, as well as high water-saturated proton conductivity. Consequently, it has been explored in a number of applications, including chlor-alkali electrolysers (Carvela et al., 2021; Thummar et al., 2022), sensors (Shen et al., 2023; Choo et al., 2022), super acid catalysts (Rong et al., 2022; Chen et al., 2023) and in particular, as a polymer and ionomer electrolyte membrane in hydrogen fuel cells (Song et al,, 2024; Yurova et al., 2021). It has been employed as an electrode modifier to immobilize cationic redox species or electrocatalysis systems, and as a matrix to immobilize GOx in glucose biosensors (Fortier et al., 1992). The low viscosity, inadequate chain entanglement and the presence of aggregates in the micellar structures in a typical solution render the formation of pure Nafion nanofibers by electrospinning a challenging process (Welch et al., 2012). It is therefore necessary to add a secondary polymer to the Nafion solution in order to prevent the formation of aggregates, increase chain entanglement and promote the successful electrospinning of Nafion nanofibers (Dong et al., 2010). Commonly, polyacrylic acid (PAA) (Chen et al., 2008; Hwang et al., 2019), polyethylene oxide (PEO) (Ballengee and Pintauro, 2011; Choi et al., 2010), polyacrylonitrile (PAN) (Han et al., 2015; Sharma et al., 2014), polyvinyl alcohol (PVA) (Zizhou et al., 2021) polyvinyl prolidone (PVP) (Sun et al., 2019) and Cellulose Acetate (CA) (Bostancı et al., 2019) are employed as carrier polymers for Nafion electrospinning. The utilization of Nafion nanofibers has recently been demonstrated in the development of DNA biosensors and a biosensor for the electrochemical detection of hydrogen peroxide (Devados et al., 2013). Despite the successful production of Nafion nanofibers and their pervasive deployment in biosensors, their applications remain constrained in biosensors designed for the detection of analytes such as glucose, urea, and cholesterol (Ding et al., 2010; Gideon et al., 2024; Singh et al., 2022).

This study introduces new amperometric glucose biosensors utilizing Nafion nanofibers as an innovative immobilization platform for both glucose oxidase (GOx) and GOx-AuNPs. To enhance the sensitivity of traditional biosensors based on Nafion films; this research integrated the enzyme with gold nanoparticles (AuNPs) prior to immobilization within the Nafion matrix. This strategy led to the development of sensors exhibiting a high surface area-to-volume ratio, increased enzyme loading capacity, and faster response times. This work focused on the systematic investigation of GOx-AuNPs (10 nm) immobilization onto Nafion nanofibers. The synthesis of Nafion nanofibers involved incorporating cellulose acetate (CA) into a Nafion solution, where CA acted as the carrier polymer. The nanofibers were fabricated through an optimized electrospinning process. Subsequently, biosensors were prepared by immobilizing a solution containing GOx and GOx-AuNPs onto the synthesized Nafion nanofibers. The performance of the fabricated biosensors was assessed under conditions conducive to hydrogen peroxide production. Amperometric measurements were employed to

determine key performance parameters, including the linear range, sensitivity, operational stability, and limit of detection (LOD). A comparative analysis was conducted between Pt/Nafion-CA NFs/GOx and Pt/Nafion-CA NFs/GOx-AuNPs biosensors to elucidate the influence of AuNPs on the catalytic activity of the GOx enzyme.

2. Experimental

2.1. Materials and instrumentation

15 wt % Cellulose Acetate powder (Mn ~30.000 CA), Nafion (~ 5 wt % in mixture of lower aliphatic alcohols and water solution), Glucose oxidase (b-D-Glucose: oxygen 1-oxidoreductase) from Aspergillus niger (type X-S, lyophilized powder, 135 200 U/g), glutaraldehyde (50 wt% in H_2O), D-glucose (99%), sucrose (99%), citric acid (99%), ascorbic acid (99%), sodium dodecyl sulfate (SDS) (ACS reagent, 99.0%), lactic acid (99%), fructose (99%), uric acid (99%), NaCl, KCl, disodium hydrogen phosphate, sodium dihydrogen phosphate, acetone (99% purity) and colloidal gold nanoparticles (10nm, stabilized in PBS) were purchased from Sigma-Aldrich. Blood serum samples were obtained from a local clinic. The ultrapure water (18.2 mX/cm was from a Direct-Q_ Water Purification System (Merck Millipore). All other chemicals were of analytical grade and used without any purification.

2.2. Electrospinning of Nafion-Cellulose Acetate (Nafion-CA) nanofibers

Cellulose Acetate (CA) with a weight ratio of 15% was dissolved in acetone under gentle stirring. Subsequently, the previously received Nafion solution was added to the CA/acetone solution, maintaining a Nafion/CA volume ratio of 1:4, and magnetically stirred overnight until a suitable homogeneous and transparent solution was obtained. The solution was electrospun into a nanofiber structure using the optimal electrospinning parameters, namely 20 kV, 1 mL/h, and 20 cm. For morphological characterization, the nanofibers were electrospun onto an aluminum foil. For biosensor construction, a platinum disk electrode was utilized. The morphology of the Nafion-CA nanofibers was characterized using scanning electron microscopy (SEM), with analysis conducted on a Zeiss LEO 1430 scanning electron microscope. All chronoamperometric measurements were conducted using the GAMRY potentiostat (600 ™). The experiment was conducted using a Gamry Instruments Inc. 600 potentiostat and the resulting data were analyzed using the Gamry Echem Analysis Software. The three-electrode cell configuration comprised a platinum disk electrode acting as the working electrode, a platinum wire as the counter electrode and an Ag/AgCl (3 KCl saturated with AgCl as an internal solution, BASi) reference electrode.

2.3. Preparation of Pt/Nafion- CA NFs/GOx and Pt/Nafion- CA NFs/GOx-AuNPs enzyme electrodes

After electrospinning on the surface of the Pt disk electrode and subsequently drying, enzyme was immobilized by cross-linking. For Pt/Nafion- CA NFs/GOx biosensor glucose oxidase solution (5 µL in ultrapure water) equivalent to 47.72 U was dropped on the surface of electrode and allowed to dry at room temperature. For Pt/ Nafion- CA NFs/GOx-AuNPs biosensor enzyme electrode has been prepared by mixing GOx enzyme in 35 µL AuNPs(10nm) solution ,then 5 µL of GOx-AuNPS (10 nm) (equivalent to 47.72U GOx and 3.0 10^{10} gold particles) was dropped onto surface of Pt electrode and allowed to dry at room temperature. Both enzyme electrodes was cross-linked by dropping 10µ L of 2.5% glutaraldehyde solution and left to dry again at room conditions. Prepared biosensors were stored in buffer solution PBS at pH 7 and in the refrigerator at +4 °C to be used later in electrochemical analyzes.

2.4. Amperometric studies on the Pt/Nafion-CA NFs /GOx and Pt/Nafion-CA NFs /GOx-AuNPs biosensors

Some operational parameters such as the pH value of buffer solution and applied potential can affected the performance of biosensors. Therefore, before the amperometric measurement optimum pH and using potential for the biosensors must be determined. For this purpose, for the Pt/Nafion-CA NFs /GOx biosensors buffer solutions at different pH values (in the 5.5–7.5) range were used in order to determine the optimum pH by measuring the current response to a 0.02 mM glucose solution at 0.6 V. Figure 1(a) shows the effect of the pH value on the Pt/Nafion-CA NFs /GOx biosensors, where the maximum response was determined at a pH of 7 which is consistent with that of most GOx-based glucose biosensors. Figure 1(b) shows the effect of applied potential on the Pt/Nafion-CA NFs /GOx biosensor, where the maximum current response was achieved at 0.6 V; at pH 7. Hence, the potential of 0.6 V and pH 7 were found to be the optimum conditions for Pt/Nafion-CA NFs /GOx biosensors.

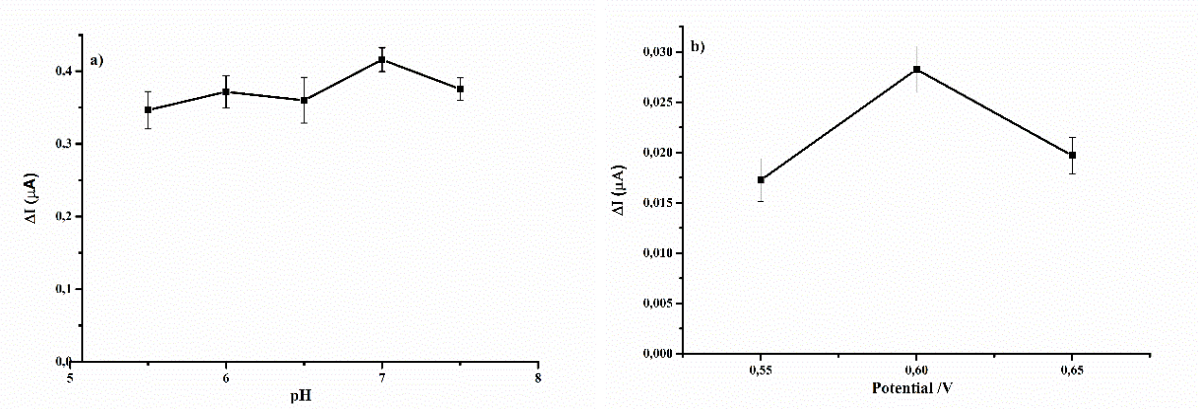

Figure 1. The effect of (a) pH and (b) potential on the response of the Pt/Nafion-CA NFs/GOx biosensor to 0.02mM of glucose in 0.1M PBS at 25°C

For the Pt/Nafion-CANFs /GOx-AuNPs biosensors a buffer solution at different pH values (in the 5.5–8) range were used in order to determine the optimum pH by measuring the current response to a 0.5 mM glucose solution at 0.6 V. Figure 2(a) shows the effect of the pH value on the Pt/Nafion-CA NFs /GOx-AuNPs biosensors, where the maximum response was determined at a pH of 7.5. Immobilized GOx can retain its activity under wide pH conditions, indicating that nanofibers and AuNPs provide a biocompatible microenvironment conducive to GOx survival (Zheng et al., 2011). The presence of gold nanoparticles ensures the stability of biosensors. This effect should be attributed to the fact that gold nanoparticles can strongly adsorb the enzyme and thus prevent enzyme leakage (Luo et al., 2004). The binding of enzymes on the nanoparticles surface involves electrostatic forces and therefore depends on both the pH of the suspension and the isoelectric point of the enzyme (Sotnikov et al., 2019). To determine the appropriate pH for optimal enzymes-gold conjugation, various approaches have been used such as spectrophotometric determination of absorption isotherms, isoelectric focusing and radio assay (Teichroeb et al., 2009). The effect of pH onto GOx-AuNPs was studied by Wang et al. (2011). They showed that the increases of pH value of the GOx-AuNPs related to the adsorption and co-adsorption in template monolayer to multilayer of the enzyme on the gold nanoparticles (Wang et al., 2016). The shift from monolayer to multilayer protein immobilization can be either a consequence of a change in the sorption properties of the nanoparticles, or a spontaneous aggregation of the proteins with an increase in the pH of the medium (Sotnikov et al., 2019). Figure 2(b) shows the effect of applied potential on the Pt/Nafion-CA NFs /GOx-AuNPs biosensor, where the maximum current response was

achieved at 0.6 Vat pH 7.5. Hence, the potential of 0.6 V and pH 7.5 were found to be the optimum conditions for Pt/Nafion-CA NFs /GOx-AuNPs biosensors.

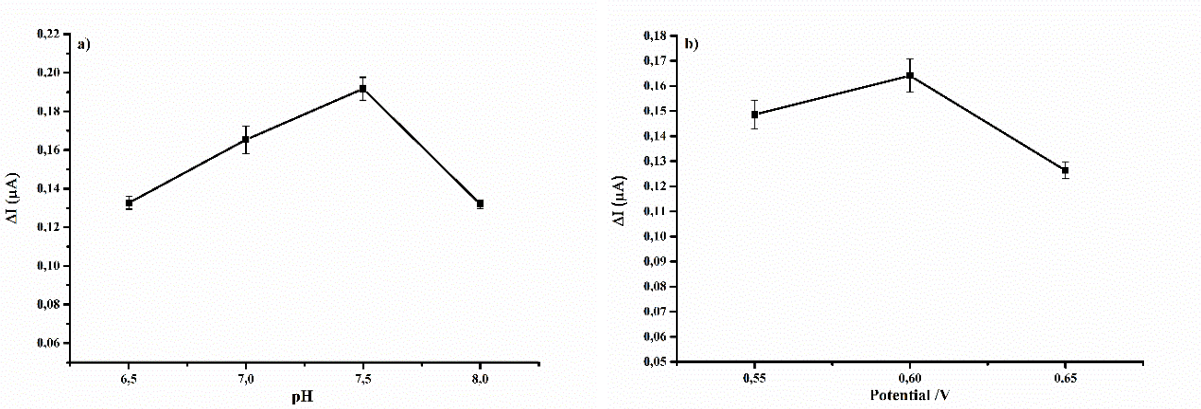

Figure 2. The effect of (a) pH and (b) potential on the response of the Pt/Nafion-CA NFs/GOx-AuNPs biosensor to 0.5mM of glucose, in 0.1M PBS at 25°C

2.5. Principles of measurements

For prepared biosensors all chronoamperometric measurements were carried out under controlled magnetic stirring (200 rpm) under conditions optimized for the detection of glucose (0,6 V vs Ag/AgCl). Increasing concentrations of glucose were added under steady state conditions in working medium (10 mL, 0.1 M PBS) until the slope between the substrate concentration and the current response deviated from the straight line. The LOD was calculated using the 3Sb/m criterion, (m: slope of the calibration curve and Sb: standard deviation of the responses at the minimum concentration (n = 10) (Shrivastava and Gupta, 2011)). Interference studies were carried out with an interfering compound: glucose ratio of 1:10. The applicability of the developed biosensors in real samples was tested by measuring glucose levels in two samples of human serum without pretreatment or dilution.

3. Results and Discussion

3.1. Morphology characterization of Nafion- CA nanofibers

Figure 3 represents the SEM images of Nafion-CA nanofibers. As can be seen, all the nanofibers have a well-defined, bead free, homogeneous morphology with optimum diameters was around 461,53l ±30,34nm. Obtained nanofibers were founded smaller than Nafion-PEO nanofibers 700nm (Okafor et al., 2014) 900nm (Ballengee and Pintauro, 2010). We notice that the diameters of the Nafion nanofibers depend on the nature of the carrier polymers as well as on the ratio of the electrospun solution (Bostancı et al., 2019) and the electrospinning parameters.

3.2. Chronoamperometric measurements

Chronoamperometric measurements on the Pt/Nafion-CA NFs /GOx

As it is known, the working principle of the first generation glucose biosensors is generally based on monitoring the oxidation of the H_2O_2 product formed as a result of the enzymatic reaction or the reduction of the O_2 consumed in this enzymatic reaction. A comparative study was conducted to understand the effect of gold nanoparticle use on the enzymatic action of GOx enzyme in amperometric biosensors based on Nafion film and nanofibers. An important part of the literature studies are studies in which enzymatic reactions are followed, and linear

range and sensitivity values are calculated in a significant part (Table 1). Nafion film has been used frequently in several fields for a long time, but in biosensor for glucose detection is very rare (Fortier et al., 1992; Tsai et al., 2005). Nafion film was used as a matrix to immobilize the enzyme glucose as well modified enzyme with nanoparticles for detection of glucose (Zhao et al., 2006; Thibault et al., 2008).

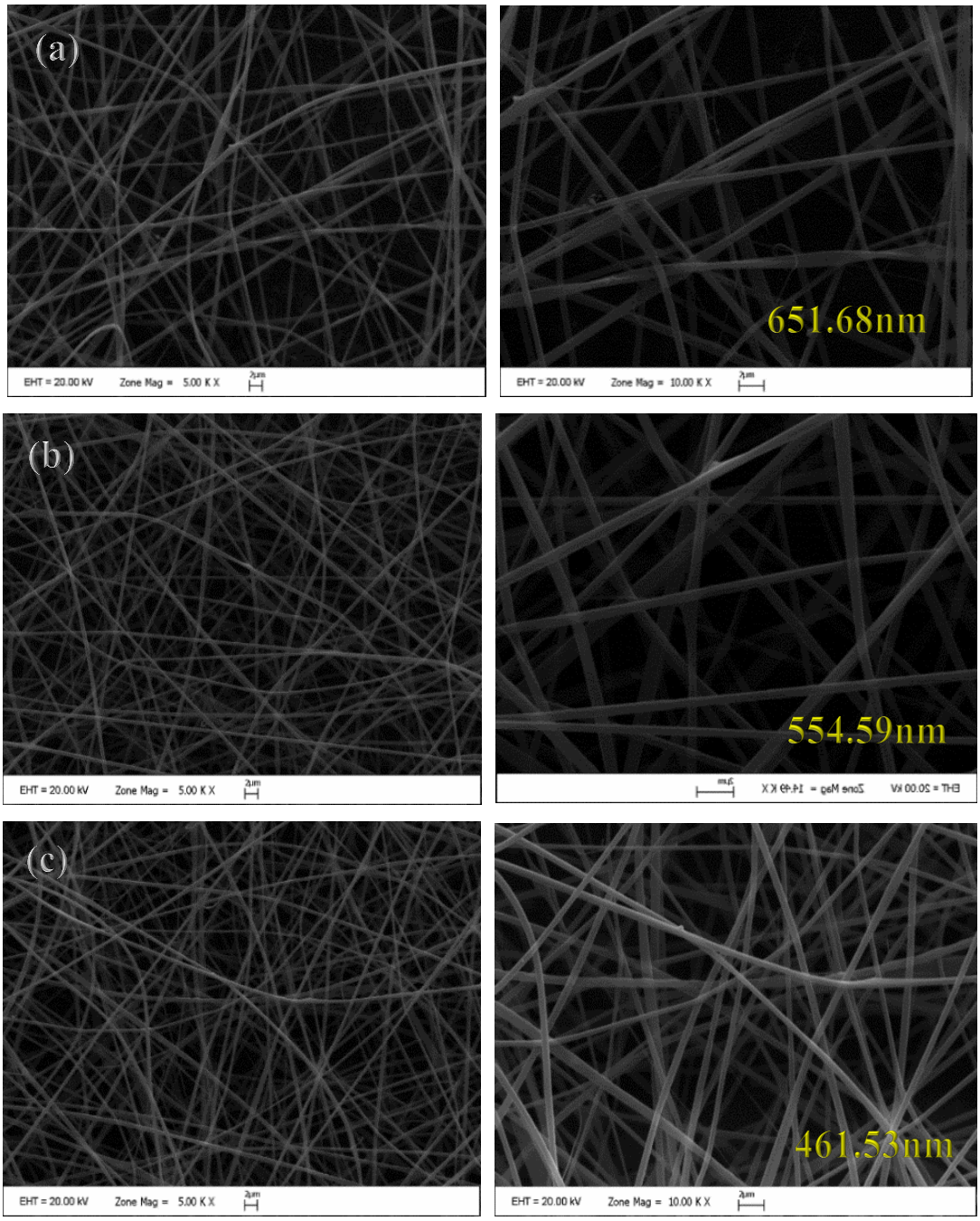

Figure 3. SEM images of Nafion-CA nanofibers with Potential, Distance, Flow rate: (a) 18 kV, 15 cm, 1 ml/h. (b) 18 kV, 20 cm, 1 ml/h. (c) 20 kV, 20 cm, 1 ml/h

In our study Nafion nanofibers were used to prepare amperometric glucose biosensors. Figure 4(a) shows the amperometric response of the Pt/Nafion-CA NFs /GOx biosensor on the successive addition of glucose (from 0.01 mM to 20.39 mM). The response current increased upon an increase in the glucose concentration and the biosensor became saturated at about

9.39 mM (Figure 4(b)). Two linear ranges of the calibration curve were identified: 0.01–0.2 mM and 0.3–9.93 mM, with sensitivities calculated as 68.67 µA mM^{-1} ·cm^2 and 18.38 µA mM^{-1} ·cm^2, respectively. The Pt/Nafion-CA NFs /GOx biosensor reached a steady state in less than 10 s.

Table 1. Comparison of glucose enzymatic and non-enzymatic electrodes

Biosensor	LOD	Sensitivity	Linear range	Reference
Nafion-GOx	–	–	5µM -10 mM	Wang et al., 2016
MWNT-Nafion-GOx	4 µM	330 nA mM^{-1}	2 mM	Fortier et al., 1992
Nafion/GOx-AuNPs/GC	0.34 µM	6.5 µA mM^{-1} cm^{-2}	6 mM	Tsai et al., 2005
Nafion/GOx-AuNPs/GC	370 µM	0.4 µA mM^{-1} cm^{-2}	20 mM	Zhao et al., 2006
PEDOT-NFs/GOx-3	2.9 µM	74.22 µA.mM^{-1}.cm^2	0.01-1.7 mM	Thibault et al., 2008
PPy-NFs/GOx-1	7.8 µM	68.95 µA.mM^{-1}.cm^2	0.01–3.5mM	Çetin and Camurlu, 2017
Pristine PAN	4.2 µM	39.5 ± 0.5 µA.mM^{-1}.cm^2	0.01 - 2 mM	Çetin and Camurlu, 2018
PAN/Fc/MWCNT-COOH	4.0 µM	27.167 µA.mM^{-1}.cm^2	8 m M	Apetrei and Camurlu, 2020
FTO-CNTs/PEI/GOx	–	63.38 µA.mM^{-1}.cm^2	70–700 µM	Lin et al., 2022
MN array w/Au/Fc-PAMAM/GOx	660 µM	0.1622 µA.mM^{-1}.cm^2	1–9 mM	Dervisevic et al., 2022
Electrospun fiber w/PEDOS: PSS	3.31 mM	0.386 µA mM^{-1} cm^{-2}	0–30 mM	Seufert et al., 2024
Pt/Nafıon-CA NFs/ GOx	1.36 µM	68.67 µA. mM^{-1}.cm^{-2} 18.38 µA.mM^{-1}.cm^2	0.01-0.2mM 0.3-9.39 mM	**This work**
PVA/BTCA/β-CD/ GOx/AuNPs	10 µM	47.2 µA mM^{-1}	0.1- 0.5 mM	Guven et al., 2021
MWCNT–AuNano/GCE	10.0	0.55 ± 0.03 µA.mM^{-1}.cm^2	0.1–25 mM	Branagan and Breslin, 2019
PB/GO*x*-AuNPs-CS	1.62 µM	40.41µA ·mM^{-1} ·cm^{-2} 8.90µA ·mM^{-1} ·cm^{-2}	0.025–2.00 mM 2.00–6.50 mM	Peng et al., 2023
AuNR/GCE	1.58 mM	13.7 µA mM^{-1}.cm^2	5–160 µM	Nazish et al., 2024
Electrospun electrode w/AuNFs/PB	1.01 mM	31.94 µA $(lg(mM))^{-1}$ cm^{-2}	1–30 mM	Tang et al., 2024
GOx/AuNPs/PMMA/PET	330 ± 50 µM	3.10 ± 0.06 µA.mM^{-1}.cm^2	8 mM	Aldea et al., 2021
Pt/Nafıon- CA Nfs /GOx-AuNPs	10.8µM	55.78µA.mM^{-1}.cm^2 28.49µA.mM^{-1}.cm^2	0.01-1.11 mM 1.51-12.89 mM	**This work**

This demonstrated the fast electron exchange and good electrocatalytic oxidative behavior of the nanofibers. By comparing the results obtained for the biosensors based on Nafion nanofibers and that based on Nafion film (Fortier et al., 1992; Tsai et al., 2005), we find that the generated Pt/Nafion-CA NFs/GOx biosensors have the good results in terms of sensitivity and LOD value. The lowest LOD data of the Pt/Nafion-CA Nfs/GOx biosensor, which was examined by monitoring H_2O_2, stood out as (1.36 µM) and high linear range data (0.01-0.2 mM and 0.3-9.39 mM) respectively. The low LOD values in question were found to be better than the other results of biosensor based on nanofibers (Çetin and Camurlu, 2017; Çetin and Camurlu, 2018; Apetrei and Camurlu, 2020; Guven et al., 2021) and good sensitivity values.

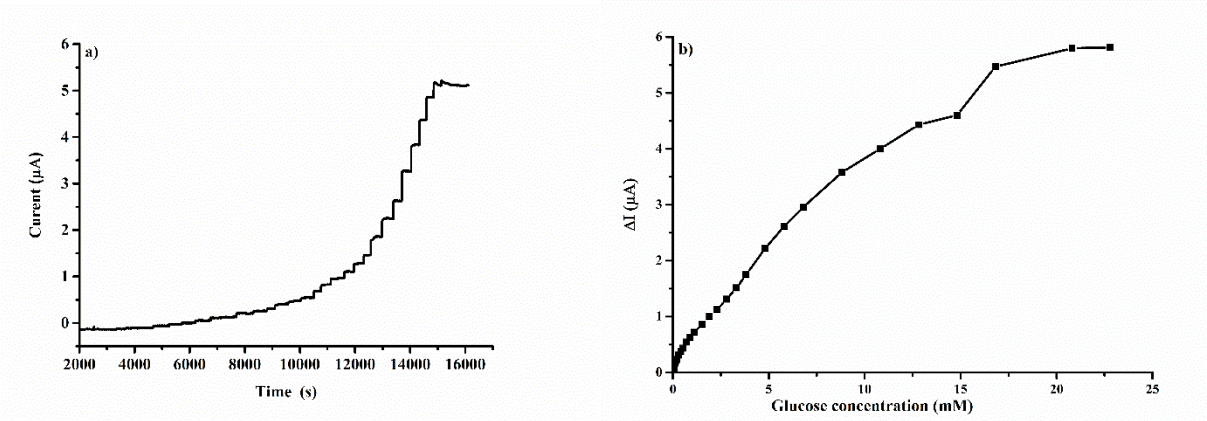

Figure 4. (a) Amperometric response of the Pt/Nafion-CA NFs /GOx biosensor to the addition of glucose and (b) The calibration curve.

Chronoamperometric measurements on the Pt/Nafion-CA NFs /GOx-AuNPs

Figure 5(a) illustrates the amperometric response of the Pt/Nafion-CA NFs/GOx-AuNPs biosensor upon successive additions of glucose, ranging from 0.01 mM to 56.81 mM. A consistent increase in the response current was observed with increasing glucose concentration, with sensor saturation occurring at approximately 12.81 mM (Figure 5(b)). The calibration curve exhibited two distinct linear ranges: 0.01-1.11 mM and 1.51-14.81 mM, with calculated sensitivities of 55.56 µA $mM^{-1} \cdot cm^2$ and 28.49 µA $mM^{-1} \cdot cm^2$, respectively. The Pt/Nafion-CA NFs/GOx-AuNPs biosensor demonstrated rapid response times, reaching a steady-state within 7 seconds. This rapid response time signifies efficient electron transfer and excellent electrocatalytic oxidative behavior of the GOx enzyme, facilitated by the presence of AuNPs and the unique structure of the Nafion nanofibers. The limit of detection (LOD) was determined to be 10.8 µM (signal-to-noise ratio of 3, with five replicates), establishing it as the lowest LOD reported among glucose biosensors employing GOx-AuNPs immobilized on nanofibers. For instance, Kim and Kim (2020) reported a PVA/BTCA/β-CD/GOx/AuNP nanofiber hydrogel biosensor with a sensitivity of 47.2 µA mM^{-1} cm^{-2} a narrow linear range of 0.1 mM - 0.5 mM, and an LOD of 10 µM. Similarly, Aldea et al. (2021) described a GOx/Au/PMMA/PET biosensor characterized by a significantly lower sensitivity of 3.10 ± 0.06 µA mM^{-1} cm^{-2} and a linear range extending up to 8 mM. In comparison to these reported results, the newly developed Pt/Nafion-CA NFs/GOx-AuNPs biosensor based on Nafion nanofibers emerges as a superior platform for the immobilization of GOx-AuNPs.

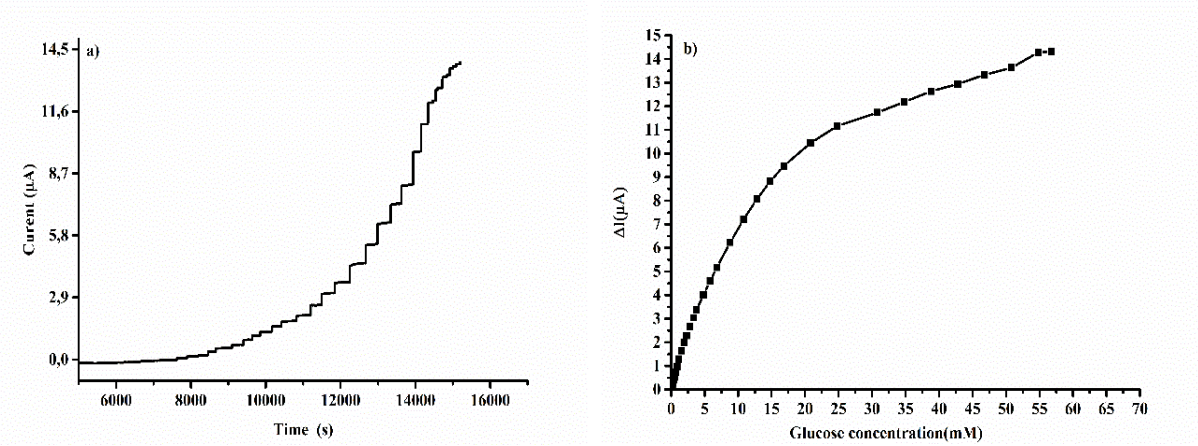

Figure 5. (a) Amperometric response of the Pt/Nafion-CA NFs /GOx-AuNPs biosensor to the addition of glucose and (b) The calibration curve.

Comparison between Pt/ Nafion- CA Nfs /GOx and Pt/Nafion- CA Nfs /GOx-AuNPs biosensors

The generated glucose biosensors Pt/Nafion-CA Nfs/GOx and Pt/Nafion-CA Nf/GOx-AuNPs were compared to evaluate the sensor sensitivity of the glucose biosensor in the presence and absence of gold nanoparticles with the same amount of enzyme. The sensor containing gold nanoparticles demonstrated a broader glucose concentration range, as shown in Figure 6(a, b). This effect can be attributed to the expanded linear range and amplified response current, resulting from the high conductivity of gold nanoparticles. Additionally, the nanoparticles enhanced the specific modification of the enzyme on the platinum electrode surface, thereby improving the glucose oxidase (GOx) target detection capability. As showed the speed of response of the biosensor with the GOx enzyme modified with gold nanoparticles is the fastest (< 7 s) biosensor due to the specificity and their ability to intensify direct electrons transfer between the active site of the enzyme and the surface of the electrode. Concerning the sensitivity of the biosensors, it was noticed that the presence of AuNPs makes it possible to increase the sensitivity of the second liner range with a slight decrease in the first sensitivity of the primary liner range.

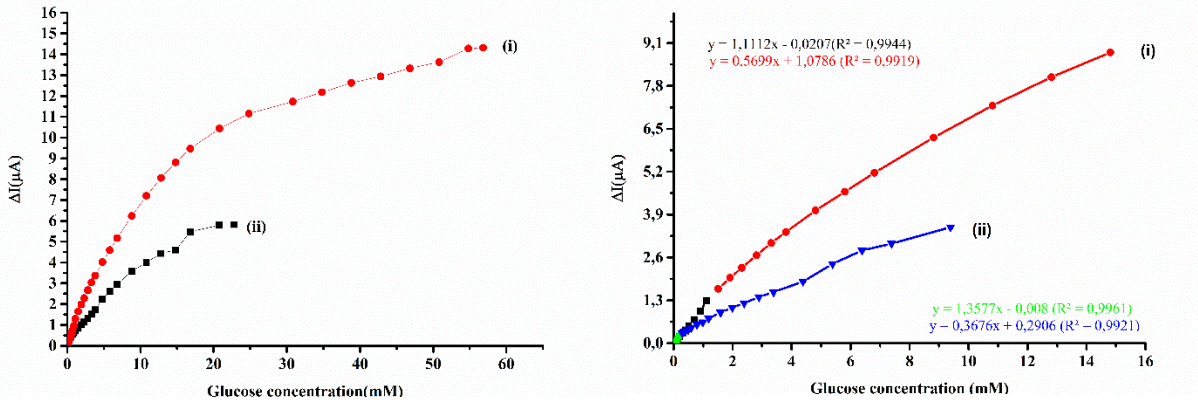

Figure 6. Evolution of the observed current values of (i) Pt/Nafion-CA Nf/GOx-AuNPs (0.01-56.81 mM) and (ii) Pt/Nafion-CA Nf/GOx (0.01-20.39 mM) with (a) the glucose concentration and (b) their linear ranges

3.3. Interference study

To assess the selectivity of the biosensors, an interference study was conducted on both Pt/Nafion-CA NFs/GOx and Pt/Nafion-CA NFs/GOx-AuNPs biosensors. Potential interferents, including ascorbic acid (AA), sucrose (Su), fructose (Fru), citric acid (CA), lactic acid (LA), uric acid (UA), urea, NaCl, KCl, and paracetamol (Parac), were evaluated using 0.5 mM solutions. Figures 7 (a,b) illustrate the amperometric responses of the Pt/Nafion-CA NFs/GOx biosensor to glucose, Su, Fru, CA, and AA. The results demonstrated minimal or negligible interference from these common interferents compared to the well-defined glucose signal, aligning with previous studies (Thota, Ganesh, 2014; Jia et al., 2009). The biosensor exhibited insignificant interference from Su, Fru, CA, UA, urea, NaCl, KCl, and paracetamol. However, the Nafion-CA NF/GOx biosensor demonstrated a response to 2.5% AA (Figure 7(a)) and 10.78% LA (Figure 7(b)). In contrast, the Pt/Nafion-CA NFs/GOx-AuNPs biosensor exhibited negligible interference from all tested substances (Figure 8). However, a slight response to 9.83% LA was observed in the presence of glucose.

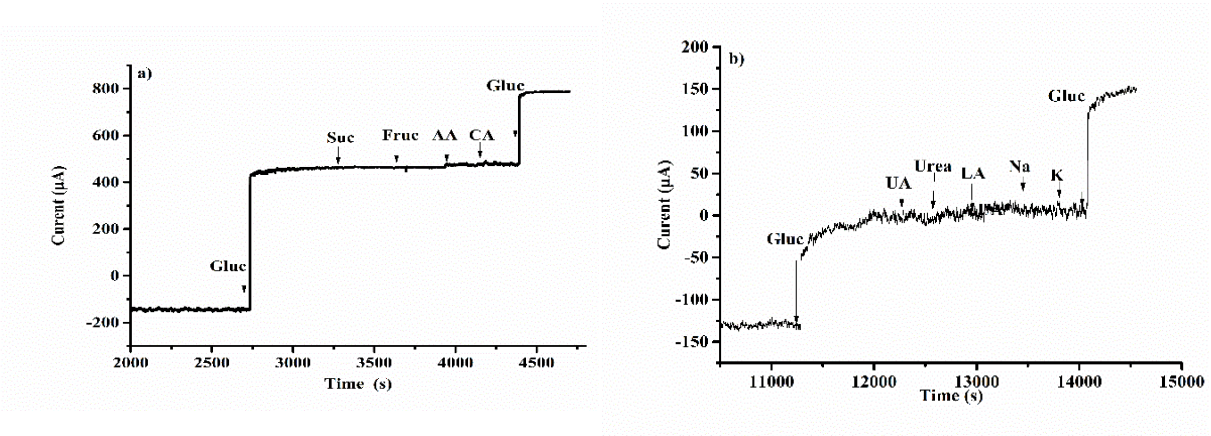

Figure 7. (a,b) Interference effect of Pt/Nafion- CA Nfs /GOx biosensor

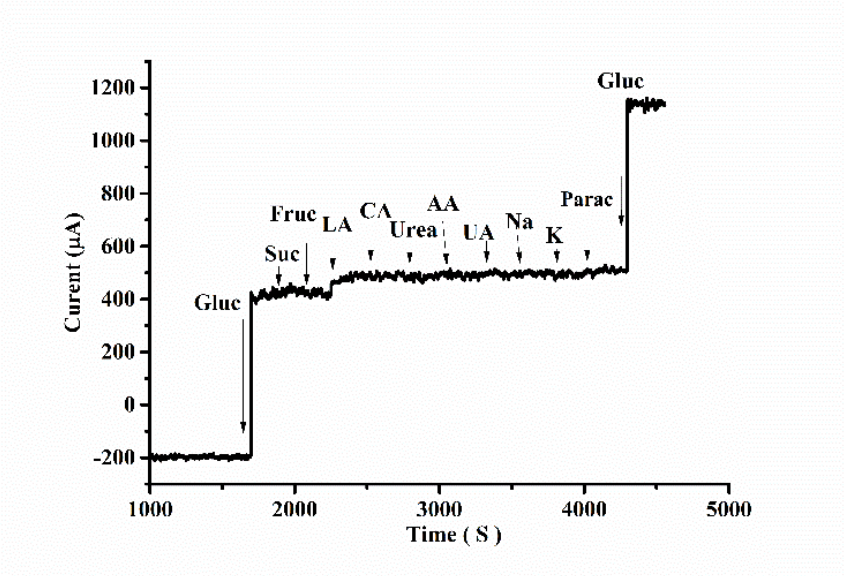

Figure 8. Interference effect of Pt/Nafion- CA Nfs /GOx AuNPs biosensor

3.4. Stability of biosensors

To evaluate operational stability, both Pt/Nafion-CA NFs/GOx and Pt/Nafion-CA NFs/GOx-AuNPs biosensors were subjected to repeated measurements with 0.5 mM glucose. Figure 9(a) demonstrates that the Pt/Nafion-CA NFs/GOx biosensor retained approximately 86.5% of its initial response after 14 consecutive measurements, exhibiting a standard deviation of ±0.024 and a relative standard deviation (RSD) of 8.38%. The reusability of Pt/Nafion-CA NFs/GOx-AuNPs biosensors was assessed under ambient conditions (25°C) by performing 14 measurements within a single day. The results revealed a standard deviation of ±0.073 and an RSD of 11.89%. As shown in Figure 9(b), the Pt/Nafion-CA NFs/GOx-AuNPs biosensor maintained 80.6% of its initial activity after the 14th measurement. Both Pt/Nafion-CA NFs/GOx and Pt/Nafion-CA NFs/GOx-AuNPs biosensors exhibited commendable operational stability, likely attributed to the biocompatibility of the porous Nafion-CA nanofibers. This porous structure may effectively preserve the structural integrity of the GOx molecules and GOx-AuNPs, thereby minimizing enzyme deactivation.

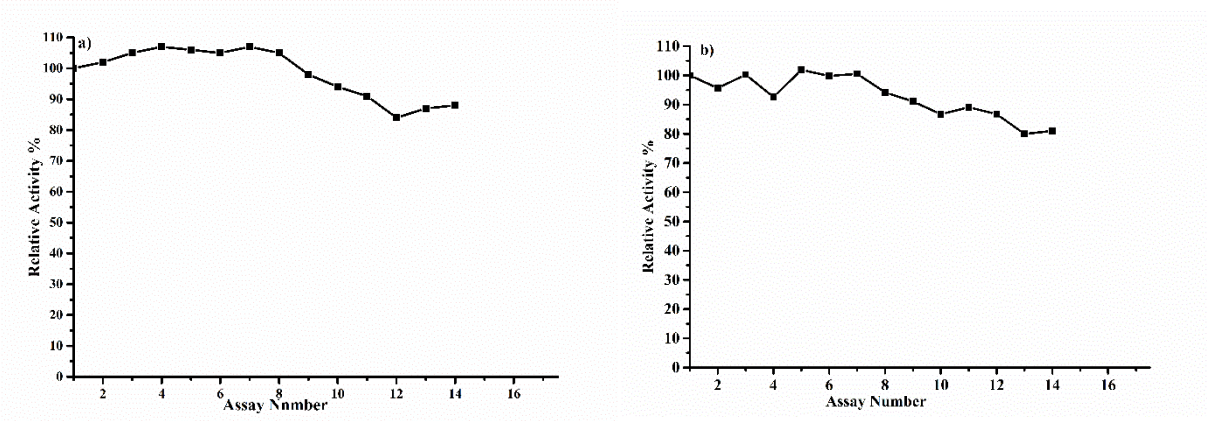

Figure 9. (a) Relative activity of Pt/Nafion-CA NFs/GOx and (b) Pt/Nafion- CA Nfs/GOx AuNPs biosensors.

3.5. Determination of glucose in real samples

To assess the applicability of the Pt/Nafion-CA NFs/GOx and Pt/Nafion-CA NFs/GOx-AuNPs biosensors in real-world scenarios, the sensors were employed to quantify glucose levels in spiked human blood samples. Recovery assays were performed to evaluate the accuracy of the biosensor measurements. Spiked blood serum samples at two different concentrations were directly introduced into a 0.1 M PBS buffer without any dilution steps. Following each sample addition, the corresponding current changes were measured and correlated to glucose concentration using the pre-established calibration curves. Table 2 summarizes the results, which represent the average of three consecutive measurements for each sample, alongside the corresponding data obtained from high-performance liquid chromatography (HPLC) analysis.

Table 2. Recovery rates of the developed biosensors for glucose detection in human blood serum samples

Biosensor	Human blood serum concentration (mg/dL)	Recovery (%)
Pt/Nafion- CA Nfs /GOx	89 mg/dL	104
Pt/Nafion- CA Nfs /GOx-AuNPs	126 mg/dL	103.7

4. Conclusion

This study describes the generation of a new amperometric biosensor based on bead-free, homogeneous Nafion nanofibers with a diameter of 461.31 ± 36 nm. The biosensors were constructed by loading GOx and GOx-AuNPs onto the Nafion-CA nanofibers and then employing glutaraldehyde to cross-link the enzyme and nanoparticles within the nanofiber matrix. The biosensors were employed for the measurement of hydrogen peroxide production at an operating potential of 0.6 V. Calibration curves were constructed for each biosensor, plotting the current response (ΔI) versus glucose concentration (mM). From these, the sensitivity, linear range and LOD values were determined. The stability of all sensors was also investigated. Nafion's nanofiber-based biosensors exhibit good sensitivity, low LOD values and reproducibility, which are superior to those of Nafion's film-based glucose biosensors. This is attributable to the intrinsic characteristics of Nafion's nanofibers, which facilitate the provision of a biocompatible milieu for the enzyme, thereby ensuring the preservation of its intrinsic activity and structural integrity. Conversely, the incorporation of gold with the enzyme immobilized on Nafion nanofibers has been observed to enhance the measurement range and linear range of glucose, as evidenced by an increase in the intensity of the current response. This is attributed to the favorable conductivity of gold and its capacity to enhance analytical detection without compromising the morphology and activity of the enzyme. Nafion nanofibers have demonstrated efficacy as a novel matrix for immobilizing GOx and GOx-AuNPs, yielding favorable outcomes in amperometric glucose detection biosensors relative to nanofiber-based biosensors. With regard to this topic, the electrochemical sensors developed based on Nafion nanofibers are particularly well-suited for monitoring other enzymatic reactions, exhibiting excellent sensitivity and stability.

Authorship Contribution Statement

Each author made significant contributions to the study. SG conducted the experimental work, was responsible for the data collection and analysis, drafted the manuscript, and contributed to the methodology. EMŞ led the conceptualization and methodology. PÇ supervised the manuscript preparation and review. All authors have read and approved the final manuscript.

Conflict of Interest

The authors declare no conflict of interest.

Acknowledgments

The author are grateful to the Akdeniz University Research Fund (FBA-2017-2516) for supporting this study.

References

Akduman, C. (2021). Cellulose acetate and polyvinylidene fluoride nanofiber mats for N95 respirators. *Journal of Industrial Textiles*, *50*(8), 1239-1261.

Aldea, A., Leote, R. J. B., Matei, E., Evanghelidis, A., Enculescu, I., & Diculescu, V. C. (2021). Gold coated electrospun polymeric fibres as new electrode platform for glucose oxidase immobilization. *Microchemical Journal*, *165*, 106108.

Apetrei, R. M., & Camurlu, P. (2020). The effect of montmorillonite functionalization on the performance of glucose biosensors based on composite montmorillonite/PAN nanofibers. *Electrochimica Acta*, *353*, 136484.

Ballengee, J. B., & Pintauro, P. N. (2011). Composite fuel cell membranes from dual-nanofiber electrospun mats. *Macromolecules*, *44*(18), 7307-7314.

Ballengee, J., & Pintauro, P. (2010). Morphological Control of Electrospun Nafion Nanofiber Mats. *ECS Transactions*, *33*(1), 647.

Barhoum, A., Rasouli, R., Yousefzadeh, M., Rahier, H., & Bechelany, M. (2018). Nanofiber technology: History and developments. In *Handbook of Nanofibers* (pp. 1-42). Springer International Publishing AG.

Bostancı, A., Tanık, N. A., & Aykut, Y. (2019). Cellulose monoacetatenafion (CMA/N) hybrid nanofibers as interface for electrochemical DNA biosensors. *Textile and Apparel*, *29*(3), 228-236.

Branagan, D., & Breslin, C. B. (2019). Electrochemical detection of glucose at physiological pH using gold nanoparticles deposited on carbon nanotubes. *Sensors and Actuators B: Chemical*, *282*, 490-499.

Carvela, M., Lobato, J., & Rodrigo, M. A. (2021). Chloralkali low temperature PEM reversible electrochemical cells. *Electrochimica Acta*, *387*, 138542.

Cetin, M. Z., & Camurlu, P. (2017). Utilization of polypyrrole nanofibers in glucose detection. *Journal of The Electrochemical Society*, *164*(12), B585.

Chen, J., Shen, C., & Gao, S. (2023). Nafion-like structured perfluoropoly (diphenylene) graft polymers microphase separated anion exchange membranes. *Desalination*, *557*, 116600.

Choi, J., Lee, K. M., Wycisk, R., Pintauro, P. N., & Mather, P. T. (2010). Nanofiber composite membranes with low equivalent weight perfluorosulfonic acid polymers. *Journal of Materials Chemistry*, *20*(30), 6282-6290.

Choi, S., Raja, I. S., Selvaraj, A. R., Kang, M. S., Park, T. E., Kim, K. S., ... & Park, J. C. (2023). Activated carbon nanofiber nanoparticles incorporated electrospun polycaprolactone scaffolds to promote fibroblast behaviors for application to skin tissue engineering. *Advanced Composites and Hybrid Materials*, *6*(1), 24.

Choo, T. F., Saidin, N. U., Zali, N. M., & Kok, K. Y. (2022). Hydrogen and humidity sensing characteristics of Nafion, Nafion/graphene, and Nafion/carbon nanotube resistivity sensors. *Journal of Nanoparticle Research*, *24*(7), 152.

Courrol, L. C., & de Matos, R. A. (2016). Synthesis of gold nanoparticles using amino acids by light irradiation. *Catalytic application of nano-gold catalysts*, *83*.

Çetin, M. Z., & Camurlu, P. (2018). An amperometric glucose biosensor based on PEDOT nanofibers. *RSC advances*, *8*(35), 19724-19731.

Dadadzhanov, D. R., Vartanyan, T. A., Dadadzhanova, A. I., & Karabchevsky, A. (2020, January). Surface-enhanced near-infrared absorption (SENIRA) of CH and NH groups with gold nanoarray. In *Quantum Sensing and Nano Electronics and Photonics XVII* (Vol. 11288, pp. 190-195). SPIE.

Deitzel, J. M., Kleinmeyer, J. D., Hirvonen, J. K., & Tan, N. B. (2001). Controlled deposition of electrospun poly (ethylene oxide) fibers. *Polymer*, *42*(19), 8163-8170.

Dervisevic, M., Alba, M., Yan, L., Senel, M., Gengenbach, T. R., Prieto-Simon, B., & Voelcker, N. H. (2022). Transdermal electrochemical monitoring of glucose via high-density silicon microneedle array patch. *Advanced Functional Materials*, *32*(3), 2009850.

Devadoss, A., Han, H., Song, T., Kim, Y. P., & Paik, U. (2013). Gold nanoparticle-composite nanofibers for enzymatic electrochemical sensing of hydrogen peroxide. *Analyst*, *138*(17), 5025-5030.

Din, I. U., Shaharun, M. S., Naeem, A., Tasleem, S., & Johan, M. R. (2018). Carbon nanofibers based copper/zirconia catalysts for carbon dioxide hydrogenation to methanol: Effect of copper concentration. *Chemical Engineering Journal*, *334*, 619-629.

Ding, B., Wang, M., Wang, X., Yu, J., & Sun, G. (2010). Electrospun nanomaterials for ultrasensitive sensors. *Materials today*, *13*(11), 16-27.

Dong, B., Gwee, L., Salas-de La Cruz, D., Winey, K. I., & Elabd, Y. A. (2010). Super proton conductive high-purity nafion nanofibers. *Nano letters*, *10*(9), 3785-3790.

Feng, K., Ma, W., Zhou, F., Si, C., Zheng, P., Sun, P., ... & Jiang, W. (2024). Antifouling amidoximated polyacrylonitrile-regenerated cellulose acetate composite nanofibrous membranes for oil/water separation: Membrane fabrication, performance and fouling mechanism. *Desalination*, *577*, 117411.

Feng, L., Li, S., Li, H., Zhai, J., Song, Y., Jiang, L., & Zhu, D. (2002). Super-hydrophobic surface of aligned polyacrylonitrile nanofibers. *Angewandte Chemie-International Edition*, *41*(7), 1221-1223.

Fortier, G., Vaillancourt, M., & Bélanger, D. (1992). Evaluation of nafion as media for glucose oxidase immobilization for the development of an amperometric glucose biosensor. *Electroanalysis*, *4*(3), 275-283.

Gideon, O., Samuel, H. S., & Okino, I. A. (2024). Biocompatible materials for next-generation biosensors. *Discover Chemistry*, *1*(1), 34.

Guarino, V., Bonadies, I., & Ambrosio, L. (2018). Fabrication of nanofibers and nanotubes for tissue regeneration and repair. In *Peptides and Proteins as Biomaterials for Tissue Regeneration and Repair* (pp. 205-228). Woodhead Publishing.

Guo, C., Liu, D., Xu, W., He, L., & Liu, S. (2023). Accelerating the peroxidase-and glucose oxidase-like activity of Au nanoparticles by seeded growth strategy and their applications for colorimetric detection of dopamine and glucose. *Colloids and Surfaces A: Physicochemical and Engineering Aspects*, *658*, 130555.

Gupta, V. K., Fakhri, A., Agarwal, S., Bharti, A. K., Naji, M., & Tkachev, A. G. (2018). Preparation and characterization of TiO2 nanofibers by hydrothermal method for removal of benzodiazepines (diazepam) from liquids as catalytic ozonation and adsorption processes. *Journal of Molecular Liquids*, *249*, 1033-1038.

Guven, N., Apetrei, R. M., & Camurlu, P. (2021). Next step in 2nd generation glucose biosensors: Ferrocene-loaded electrospun nanofibers. *Materials Science and Engineering: C*, *128*, 112270.

H.Chen, J. D. Snyder, Y.A. Elabd, Electrospinning and Solution Properties of Nafion and Poly (Acrylic Acid), *Macromolecules,* 41 (2008) 128-135.

Han, M., Zhao, H., Ding, M., Gao, P., & Liu, B. (2015). Study on Sponge-Nafion Membranes Prepared by Electro Spinning Method. *Integrated Ferroelectrics*, *162*(1), 55-61.

Hecht, H. J., Kalisz, H. M., Hendle, J., Schmid, R. D., & Schomburg, D. (1993). Crystal structure of glucose oxidase from Aspergillus niger refined at 2·3 Å reslution. *Journal of molecular biology*, *229*(1), 153-172.

Hernández, B., Tinacci, L., Coïc, Y. M., Chenal, A., Cohen, R., Sanchez-Cortes, S., & Ghomi, M. (2018). Tryptophan tight binding to gold nanoparticles induces drastic changes in indole ring Raman markers. *The Journal of Physical Chemistry C*, *122*(24), 13034-13046.

Hwang, M., Karenson, M. O., & Elabd, Y. A. (2019). High production rate of high purity, high fidelity nafion nanofibers via needleless electrospinning. *ACS Applied Polymer Materials*, *1*(10), 2731-2740.

Hynes, N. R. J., Sankaranarayanan, R., & Kumar, J. P. S. (2021). Nanoparticles and medicine. *Nanomedicine manufacturing and applications*, 21-37.

Islam, M. S., Ang, B. C., Andriyana, A., & Afifi, A. M. (2019). A review on fabrication of nanofibers via electrospinning and their applications. *SN Applied Sciences*, *1*, 1-16.

Jia, W., Guo, M., Zheng, Z., Yu, T., Rodriguez, E. G., Wang, Y., & Lei, Y. (2009). Electrocatalytic oxidation and reduction of H2O2 on vertically aligned Co3O4 nanowalls electrode: Toward H2O2 detection. *Journal of Electroanalytical Chemistry*, *625*(1), 27-32.

Kim, G. J., & Kim, K. O. (2020). Novel glucose-responsive transparent nanofiber hydrogel patches as a wearable biosensor via electrospinning. *Scientific Reports, 10,* 18858.

LF Nascimento, M., S. Araujo, E., R. Cordeiro, E., HP de Oliveira, A., & P. de Oliveira, H. (2015). A literature investigation about electrospinning and nanofibers: historical trends, current status and future challenges. *Recent patents on nanotechnology*, *9*(2), 76-85.

Lin, M. H., Gupta, S., Chang, C., Lee, C. Y., & Tai, N. H. (2022). Carbon nanotubes/polyethylenimine/glucose oxidase as a non-invasive electrochemical biosensor performs high sensitivity for detecting glucose in saliva. *Microchemical Journal*, *180*, 107547

Lipińska, W., Grochowska, K., & Siuzdak, K. (2021). Enzyme immobilization on gold nanoparticles for electrochemical glucose biosensors. *Nanomaterials*, *11*(5), 1156.

Liu, G., Ding, J., Qiao, L., Guo, A., Dymov, B. P., Gleeson, J. T., ... & Saijo, K. (1999). Polystyrene-block-poly (2-cinnamoylethyl methacrylate) nanofibers—Preparation, characterization, and liquid crystalline properties. *Chemistry–A European Journal*, *5*(9), 2740-2749.

Liu, L., Wang, Z., Yang, J., Liu, G., Li, J., Guo, L., ... & Guo, Q. (2018). NiCo2O4 nanoneedle-decorated electrospun carbon nanofiber nanohybrids for sensitive non-enzymatic glucose sensors. *Sensors and Actuators B: Chemical*, *258*, 920-928.

Luo, X. L., Xu, J. J., Du, Y., & Chen, H. Y. (2004). A glucose biosensor based on chitosan–glucose oxidase–gold nanoparticles biocomposite formed by one-step electrodeposition. *Analytical biochemistry*, *334*(2), 284-289.

Lyu, Y., Becerril, L. M., Vanzan, M., Corni, S., Cattelan, M., Granozzi, G., ... & Scrimin, P. (2024). The interaction of amines with gold nanoparticles. *Advanced Materials*, *36*(10), 2211624.

Ma, P. X., & Zhang, R. (1999). Synthetic nano-scale fibrous extracellular matrix. *Journal of Biomedical Materials Research: An Official Journal of The Society for Biomaterials, The Japanese Society for Biomaterials, and The Australian Society for Biomaterials*, *46*(1), 60-72.

Maguteeswaran, R., Evarshini, A., Samuel, V. R., & Pondurai, S. (2024). A label free nano biosensor for the detection of E. coli using cysteine capped gold nanoparticle. *Physica Scripta*, *99*(5), 055527.

Martin, C. R. (1996). Membrane-based synthesis of nanomaterials. *Chemistry of materials*, *8*(8), 1739-1746.

Mondal, S., Adak, B., & Mukhopadhyay, S. (2023). 11 Functional and smart textiles for military and defence applications. *Smart and Functional Textiles*, 397.

Muratoglu, S., Inal, M., Akdag, Y., Gulsun, T., & Sahin, S. (2024). Electrospun nanofiber drug delivery systems and recent applications: An overview. *Journal of Drug Delivery Science and Technology*, 105342.

Nazish, Y., Sabahat, S., Saleem, R. S. Z., Saira, F., & Yaqub, A. (2024). Effect of nano-morphologies on catalysis and non-enzymatic glucose sensing. *Journal of Materials Research*, *39*(4), 649-662.

Okafor, C. N., Maaza, M., & Mokrani, T. A. E. (2014). Nafion Nanofiber Composite Membrane Fabrication for Fuel Cell Applications. *International Journal of Chemical and Molecular Engineering*, *8*(5), 418-421

Ondarcuhu, T., & Joachim, C. (1998). Drawing a single nanofibre over hundreds of microns. *Europhysics letters*, *42*(2), 215.

Ozkizilcik, A., Williams, R., Tian, Z. R., Muresanu, D. F., Sharma, A., & Sharma, H. S. (2018). Synthesis of biocompatible titanate nanofibers for effective delivery of neuroprotective agents. *Neurotrophic Factors: Methods and Protocols*, 433-442.

Pakravan, M., Heuzey, M. C., & Ajji, A. (2011). A fundamental study of chitosan/PEO electrospinning. *Polymer*, *52*(21), 4813-4824.

Peng, Z., Li, Z., Liao, J., Zhang, Z., Song, Y., Xia, C., ... & Wang, Z. (2023). Study of electrochemical biosensor for determination of glucose based on Prussian blue/gold nanoparticles-chitosan nanocomposite film sensing interface. *Measurement Science and Technology*, *35*(1), 015125.

Ramanavicius, A., German, N., & Ramanaviciene, A. (2017). Evaluation of electron transfer in electrochemical system based on immobilized gold nanoparticles and glucose oxidase. *Journal of The Electrochemical Society*, *164*(4), G45.

Rong, X., Liu, W., Wang, X., Li, M., Wang, J., Lin, Z., ... & Yuan, Y. (2022). A photoelectrochemical sensor for highly sensitive detection of H_2O_2 based on [Fcmim][$N(CN)_2$]@Nafion® film modified GaN through a parallel catalysis strategy. *Sensors and Actuators B: Chemical*, *365*, 131914.

Samukaite-Bubniene, U., Mazetyte-Stasinskiene, R., Chernyakova, K., Karpicz, R., & Ramanavicius, A. (2020). Time-resolved fluorescence spectroscopy based evaluation of stability of glucose oxidase. *International Journal of Biological Macromolecules*, *163*, 676-682.

Sarangika, H. N. M., Senadeera, G. K. R., & Dissanayake, M. A. K. L. (2024). Preparation of electrospun polyacrylonıtrile (PAN) nanofıber membrane gel electrolyte and its application in TiO_2-based electrochromic devices. *Ionics*, *30*(3), 1627-1638.

Schiller, T., & Scheibel, T. (2024). Bioinspired and biomimetic protein-based fibers and their applications. *Communications Materials*, *5*(1), 56.

Seufert, B., Thomas, S., & Takshi, A. (2024). Stretchable Nanofiber-Based Felt as a String Electrode for Potential Use in Wearable Glucose Biosensors. *Sensors*, *24*(4), 1283.

Sharma, D. K., Shen, J., & Li, F. (2014). Reinforcement of Nafion into polyacrylonitrile (PAN) to fabricate them into nanofiber mats by electrospinning: characterization of enhanced mechanical and adsorption properties. *RSC advances*, *4*(74), 39110-39117.

Shen, C. H., Chang, Y. N., Chen, Y. L., & Kung, C. W. (2023). Sulfonate-grafted metal–organic framework─ a porous alternative to Nafion for electrochemical sensors. *ACS Materials Letters*, *5*(7), 1938-1943.

Shokri, E., Hosseini, M., Davari, M. D., Ganjali, M. R., Peppelenbosch, M. P., & Rezaee, F. (2017). Disulfide-induced self-assembled targets: a novel strategy for the label free colorimetric detection of DNAs/RNAs via unmodified gold nanoparticles. *Scientific reports*, *7*(1), 45837.

Shooshtari, M. (2025). Ammonia gas sensors based on multi-wall carbon nanofiber field effect transistors by using gate modulation. *Colloids and Surfaces A: Physicochemical and Engineering Aspects*, *704*, 135563.

Shrivastava, A., & Gupta, V. B. (2011). Methods for the determination of limit of detection and limit of quantitation of the analytical methods. *Chron. Young Sci*, *2*(1), 21-25.

Singh, A., Ahmed, A., Sharma, A., & Arya, S. (2022). Graphene and its derivatives: Synthesis and application in the electrochemical detection of analytes in sweat. *Biosensors*, *12*(10), 910.

Smith, S., Goodge, K., Delaney, M., Struzyk, A., Tansey, N., & Frey, M. (2020). A comprehensive review of the covalent immobilization of biomolecules onto electrospun nanofibers. *Nanomaterials*, *10*(11), 2142.

Song, S., He, H., Chai, S., & Li, H. (2024). Advanced Nafion/nanofiller composite proton exchange membranes for fuel cell applications. *Polymer*, 127241.

Sotnikov, D. V., Berlina, A. N., Ivanov, V. S., Zherdev, A. V., & Dzantiev, B. B. (2019). Adsorption of proteins on gold nanoparticles: One or more layers?. *Colloids and Surfaces B: Biointerfaces*, *173*, 557-563.

Suja, S. K., & Mathiya, S. (2024). Nanotechnology in Defense and Social Justice: Opportunities and Risks. In *Nanotechnology in Societal Development* (pp. 439-479). Singapore: Springer Nature Singapore.

Sun, Y., Cui, L., Gong, J., Zhang, J., Xiang, Y., & Lu, S. (2019). Design of a catalytic layer with hierarchical proton transport structure: the role of nafion nanofiber. *ACS Sustainable Chemistry & Engineering*, *7*(3), 2955-2963.

Tang, Z., Jian, J., Guo, M., Liu, S., Ji, S., Li, Y., ... & Ren, T. (2024). All-Fiber Flexible Electrochemical Sensor for Wearable Glucose Monitoring. *Sensors*, *24*(14), 4580

Teichroeb, J. H., McVeigh, P. Z., & Forrest, J. A. (2009). Influence of nanoparticle size on the pH-dependent structure of adsorbed proteins studied with quantitative localized surface plasmon spectroscopy. *The European Physical Journal E*, *30*(2), 157-164.

Thibault, S., Aubriet, H., Arnoult, C., & Ruch, D. (2008). Gold nanoparticles and a glucose oxidase based biosensor: an attempt to follow-up aging by XPS. *Microchimica Acta*, *163*, 211-217.

Thota, R., & Ganesh, V. (2014). Chemically modified flexible strips as electrochemical biosensors. *Analyst*, *139*(18), 4661-4672.

Thummar, K., Abang, R., Menzel, K., & de Groot, M. T. (2022). Coupling a Chlor-alkali membrane electrolyzer cell to a wind energy source: dynamic modeling and simulations. *Energies*, *15*(2), 606.

Tsai, Y. C., Li, S. C., & Chen, J. M. (2005). Cast thin film biosensor design based on a nafion backbone, a multiwalled carbon nanotube conduit, and a glucose oxidase function. *Langmuir*, *21*(8), 3653-3658.

Tu, T., Wang, Y., Huang, H., Wang, Y., Jiang, X., Wang, Z., ... & Luo, H. (2019). Improving the thermostability and catalytic efficiency of glucose oxidase from Aspergillus niger by molecular evolution. *Food chemistry*, *281*, 163-170.

Tu, T., Zhang, Y., Yan, Y., Li, L., Liu, X., Hakulinen, N., ... & Huang, H. (2024). Revealing the intricate mechanism governing the pH-dependent activity of a quintessential representative of flavoproteins, glucose oxidase. *Fundamental Research*.

Vargas-Molinero, H. Y., Serrano-Medina, A., Palomino-Vizcaino, K., López-Maldonado, E. A., Villarreal-Gómez, L. J., Pérez-González, G. L., & Cornejo-Bravo, J. M. (2023). Hybrid systems of nanofibers and polymeric nanoparticles for biological application and delivery systems. *Micromachines*, *14*(1), 208.

Wang, H., Niu, H., Wang, H., Wang, W., Jin, X., Wang, H., ... & Lin, T. (2021). Micro-meso porous structured carbon nanofibers with ultra-high surface area and large supercapacitor electrode capacitance. *Journal of Power Sources*, *482*, 228986.

Wang, K.-H., Syu, M. J., Chang, C.-H., & Lee, Y.-L. (2011). Headgroup effects of template monolayers on the adsorption behavior and conformation of glucose oxidase adsorbed at air/liquid interfaces. *Langmuir: The ACS Journal of Surfaces and Colloids, 27*(12), 7595–7602. https://doi.org/10.1021/la200234z

Wang, K. H., Wu, J. Y., Chen, L. H., & Lee, Y. L. (2016). Architecture effects of glucose oxidase/Au nanoparticle composite Langmuir-Blodgett films on glucose sensing performance. *Applied Surface Science*, *366*, 202-209.

Welch, C., Labouriau, A., Hjelm, R., Orler, B., Johnston, C., & Kim, Y. S. (2012). Nafion in dilute solvent systems: dispersion or solution?. *ACS Macro Letters*, *1*(12), 1403-1407.

Whitesides, G. M., & Grzybowski, B. (2002). Self-assembly at all scales. *Science*, *295*(5564), 2418-2421.

Yan, Y., Liu, X., Jiang, X., Zhang, W., Wang, Y., Wang, Y., ... & Tu, T. (2022). Surface charge modifications modulate glucose oxidase pH-activity profiles for efficient gluconic acid production. *Journal of Cleaner Production*, *372*, 133817.

Yan, Z., Zhai, H., Fan, D., & Li, Q. (2023). A trimode textile designed with hierarchical core-shell nanofiber structure for all-weather radiative personal thermal management. *Nano Today*, *51*, 101897.

Yıldız, E., Cetinkaya, A., Çorman, M. E., Atici, E. B., Uzun, L., & Ozkan, S. A. (2024). An electrochemical sensor based on carbon nanofiber and molecular imprinting strategy for dasatinib recognition. *Bioelectrochemistry*, *158*, 108701.

Yue, C., Yang, K., He, D., Zheng, W., Tang, Y., Zeng, X., ... & Chen, J. (2024). Free-standing ultra-thin carbon nanofiber films with controllable thickness for lithium ion batteries. *Surfaces and Interfaces*, *48*, 104347.

Yuriar-Arredondo, K., Armstrong, M. R., Shan, B., Zeng, W., Xu, W., Jiang, H., & Mu, B. (2018). Nanofiber-based Matrimid organogel membranes for battery separator. *Journal of Membrane Science*, *546*, 158-164.

Yurova, P. A., Malakhova, V. R., Gerasimova, E. V., Stenina, I. A., & Yaroslavtsev, A. B. (2021). Nafion/surface modified ceria hybrid membranes for fuel cell application. *Polymers*, *13*(15), 2513.

Zhang, H., Tian, J., Cui, X., Li, J., & Zhu, Z. (2023). Highly mesoporous carbon nanofiber electrodes with ultrahigh specific surface area for efficient capacitive deionization. *Carbon*, *201*, 920-929.

Zhao, G., Shi, L., Yang, G., Zhuang, X., & Cheng, B. (2023). 3D fibrous aerogels from 1D polymer nanofibers for energy and environmental applications. *Journal of Materials Chemistry A*, *11*(2), 512-547.

Zhao, S., Zhang, K., Bai, Y., Yang, W., & Sun, C. (2006). Glucose oxidase/colloidal gold nanoparticles immobilized in Nafion film on glassy carbon electrode: direct electron transfer and electrocatalysis. *Bioelectrochemistry*, *69*(2), 158-163.

Zheng, B., Xie, S., Qian, L., Yuan, H., Xiao, D., & Choi, M. M. (2011). Gold nanoparticles-coated eggshell membrane with immobilized glucose oxidase for fabrication of glucose biosensor. *Sensors and Actuators B: Chemical*, *152*(1), 49-55.

Zizhou, R. E., Çay, A., Akçakoca Kumbasar, E. P., & Çolpan, C. Ö. (2021). Production of poly (vinyl alcohol)/Nafion® nanofibers and their stability assessment for the use in direct methanol fuel cells. *Journal of Industrial Textiles*, *50*(6), 773-793.

Scientific Research Communications

A Note on the Dirichlet-Neumann Problem in the Upper Half Unit Disc

Bahriye Karaca

İzmir Bakırçay University, Department of Fundamental Sciences, İzmir, Türkiye

Research Article

*Correspondence:
bahriye.karaca@bakircay.edu.tr

Received: 15 December 2024
Accepted: 25 January 2025
Published: 31 January 2025

Keywords
Upper half unit disc
Dirichlet problem
Neumann problem

Abstract

This study addresses the solvability and explicit solutions of various boundary value problems (BVPs) for inhomogeneous equations within the upper half unit disc. Specifically, we investigate the Dirichlet, Neumann, and mixed Dirichlet-Neumann problems for the inhomogeneous Cauchy-Riemann and Bitsadze equations. By employing analytical techniques and function space theory, we establish necessary and sufficient conditions for the existence of solutions. Furthermore, explicit solution formulas are derived under these solvability criteria, providing a constructive approach to solving such BVPs. The significance of this research lies in its contribution to the broader theory of BVPs in complex domains. The results obtained not only extend classical boundary conditions but also offer a systematic framework for dealing with higher-order equations. The interplay between different boundary conditions is explored in detail, revealing new insights into the structure of solutions and their dependence on boundary data. Beyond the theoretical implications, our findings have potential applications in mathematical physics, fluid dynamics, and engineering, where such problems frequently arise in modeling physical phenomena. Future research may further extend these results to more general domains and nonlinear equations, enriching the field of complex analysis and partial differential equations.

1. Introduction

Boundary value problems (BVPs) play a significant role in mathematical analysis, particularly in the study of partial differential equations in complex domains. These problems frequently appear in diverse scientific and engineering fields, including fluid dynamics, electromagnetism, elasticity, and heat conduction. Among them, the Dirichlet and Neumann problems are of fundamental importance due to their wide range of applications and theoretical implications. Analyzing these problems in specific geometric domains, such as the upper half unit disc, provides valuable insights into solution behavior and the impact of boundary conditions.

One of the essential classes of PDEs studied in complex analysis involves the Cauchy-Riemann and Bitsadze equations. The solvability and explicit solutions of these equations under various boundary conditions have been extensively explored. Many researchers have contributed to the field by investigating different types of boundary conditions and their implications for

How to cite this paper: Karaca, B. (2025). A note on the Dirichlet-Neumann problem in the upper half unit disc. *Scientific Research Communications*, *5*(1), 59–66. https://doi.org/10.52460/src.2025.005

PDEs. For instance, Darya and Tagizadeh (2024) analyzed the Dirichlet problem for the Cauchy-Riemann equations in the half-disc, while Chaudhary and Kumar (2009) examined BVPs in the upper half-plane. Additionally, Kumar and Prakash (2006) addressed mixed BVPs for inhomogeneous polyanalytic equations, highlighting the complexity introduced by such conditions.

In this study, we focus on the solvability conditions and explicit solutions of the Dirichlet, Neumann, and mixed Dirichlet-Neumann BVPs in the upper half unit disc. We employ analytical techniques, integral representations, and function space methods to derive necessary and sufficient conditions for the existence of solutions. This work builds upon and extends previous studies, incorporating a broader class of boundary conditions and addressing more generalized settings.

A central challenge in this study is the mixed Dirichlet-Neumann problem, which imposes different boundary conditions on different parts of the boundary. Understanding these types of problems is crucial for applications such as heat transfer, fluid-structure interactions, and stress analysis in elasticity. Previous works, including those of Karaca (2021, 2024a, 2024b) have demonstrated the significance of studying Schwarz-type, combined BVPs in complex domains, and explored Schwarz-type and combined BVPs, extending classical results in complex analysis. Our research further explores these topics by formulating and solving analogous problems in the upper half unit disc. Kalmenov et al. (2008) provided Green function representations for the Dirichlet problem of the polyharmonic equation in a sphere, contributing to the broader understanding of BVPs.

A major challenge in this research is the mixed Dirichlet-Neumann problem, which imposes different boundary conditions on different segments of the boundary. Understanding such problems is crucial for applications in heat transfer, fluid-structure interactions, and elasticity. Previous studies, including those of Begehr et al. (2008), Wang and Du (2004), Begehr and Vaitekhovich (2008 and 2012), Begehr et al. (2017) and Karachik (2013 and 2019) have highlighted the significance of Dirichlet and combined BVPs in complex domains. Our research expands upon these topics by formulating and solving analogous problems in the upper half unit disc.

To develop the theoretical foundation for our results, we first introduce key mathematical tools, including the complex forms of the Gauss divergence theorem and the Cauchy-Pompeiu representation formula. These fundamental results provide the basis for establishing the solvability conditions for the Dirichlet and Neumann problems.

This paper is organized as follows: In Section 1, we provide the necessary theoretical background, including the formulation of the inhomogeneous Cauchy-Riemann and Bitsadze equations. Section 2 is devoted to the Dirichlet and Neumann problems, where we establish the solvability criteria and construct explicit solutions. Finally, Section 3 presents concluding remarks and potential directions for future research, including extensions to higher-order equations and applications in applied mathematics and engineering.

By systematically analyzing these BVPs, we aim to contribute to the broader understanding of PDEs in complex domains and provide a solid foundation for further investigations into related mathematical models.

A complex-valued function $\omega = u + iv$ given by two real-valued functions u and v of the real variables x and y will be denoted by $\omega(z)$ although being rather a function of z and $\bar{z}$. In case when ω is independent of $\bar{z}$ in an open set of the complex plane $\mathbb{C}$ it is an analytic function. It then satisfies the Cauchy-Riemann system of first order partial differential equations

$$u_x = v_y, \qquad u_y = -v_x.$$

This is equivalent to

$$\omega_{\bar{z}} = 0$$

as follows from

$$2\partial_{\bar{z}}\,\omega = \big(\partial_x + i\partial_y\big)(\,u + iv) = \partial_x u - \partial_y v + i\big(\partial_x v + \partial_y u\big).$$

Using these complex derivatives, the classical Gauss divergence theorem can be rewritten in a complex form for functions that are continuously differentiable in a bounded domain D with a smooth boundary ∂D. The key results that follow from this representation include the Gauss theorem (G.T.) and the Cauchy-Pompeiu representation (C.-P. r.), which are fundamental in deriving the solvability conditions for our BVPs.

Gauss Theorem (Complex Form) (G.T.) Let $D \subset \mathbb{C}$ be a regular domain (i.e. a bounded domain with smooth boundary) and let $\omega \in C^1(D;\,\mathbb{C}) \cap \mathrm{C}(\,\bar{D}\,;\mathbb{C})$. Then

$$\int_D \omega_{\bar{z}}\,(z)dxdy = \frac{1}{2i}\int_D \omega\,(z)\,dz$$

and

$$\int_D \omega_{\mathrm{z}}\,(z)dxdy = -\frac{1}{2i}\int_D \omega\,(z)\,d\bar{z}$$

for $z = x + iy$.

Cauchy–Pompeiu representation (C.–P. r.) Let D and ω be as above. Then

$$\omega(\mathrm{z}) = \frac{1}{2\pi i}\int_{\partial D}\frac{\omega(\varsigma)}{\varsigma - \mathrm{z}}\,d\varsigma - \frac{1}{\pi}\int_D \frac{\omega_{\bar{\varsigma}}(\varsigma)}{\varsigma - \mathrm{z}}d\xi d\acute{\eta}$$

and

$$\omega(\mathrm{z}) = -\frac{1}{2\pi i}\int_{\partial D}\frac{\omega(\varsigma)}{\overline{\varsigma - \mathrm{z}}}\,d\overline{\varsigma} - \frac{1}{\pi}\int_D \frac{\omega_{\varsigma}(\varsigma)}{\overline{\varsigma - \mathrm{z}}}d\xi d\acute{\eta}$$

for $\varsigma = \xi + i\acute{\eta}$ and $z \in D$.

These results serve as the foundation for establishing the existence and uniqueness of solutions to the Dirichlet and Neumann problems.

The following theorem presents the necessary and sufficient conditions for the solvability of the Dirichlet problem for the inhomogeneous Cauchy-Riemann equation in the upper half unit disc.

Theorem 1. (Darya and Tagizadeh, 2024) The Dirichlet boundary value problem for the inhomogeneous Cauchy-Riemann equation

$\omega_{\bar{z}} = g(z)$ in $\mathbb{D}^+, \omega = \Upsilon_0$ on $\partial\mathbb{D}^+$ $\mathrm{g} \in \mathrm{L_p}(\mathbb{D}^+;\mathbb{C}), \mathrm{p} > 2,\ \Upsilon_0 \in \mathrm{L}_2(\mathbb{R},\mathbb{C}) \cap C(\partial\mathbb{D}^+,\mathbb{C})$

is solvable if and only if for $z \in \mathbb{D}^+$,

$$\frac{1}{2\pi i}\int_{\partial\mathbb{D}^+}\Upsilon_0(\varsigma)\left[\frac{1}{\varsigma - \bar{z}} + \frac{\bar{z}}{\varsigma\bar{z} - 1}\right]d\varsigma - \frac{1}{\pi}\int_{\mathbb{D}^+} g(\varsigma)\left[\frac{1}{\varsigma - \bar{z}} + \frac{\bar{z}}{\varsigma\bar{z} - 1}\right]d\xi d\acute{\eta} = 0 \qquad (1)$$

and its solution can be uniquely expressed as

$$\omega(z) = \frac{1}{2\pi i}\int_{\partial\mathbb{D}^+} \Upsilon_0(\varsigma)\left[\frac{1}{\varsigma - \mathrm{z}} + \frac{\mathrm{z}}{\varsigma \mathrm{z} - 1}\right] d\varsigma - \frac{1}{\pi}\int_{\mathbb{D}^+} g(\varsigma)\left[\frac{1}{\varsigma - \mathrm{z}} + \frac{\mathrm{z}}{\varsigma \mathrm{z} - 1}\right] d\xi d\acute{\eta}, \tag{2}$$

where $\varsigma = \xi + i\acute{\eta}$.

The following theorem presents the necessary and sufficient conditions for the solvability of the Neumann problem for the inhomogeneous Cauchy-Riemann equation in the upper half unit disc.

Theorem 2. (Karaca, 2024b) The Neumann problem for the inhomogeneous Cauchy- Riemann equation in the upper half unit disc

$\omega_{\bar{z}} = \mathrm{g(z)}$ in $\mathbb{D}^+$, $\partial_\nu \omega = \Upsilon$ on $\partial\mathbb{D}^+$, $\omega(0) = \mathrm{c}$

for $\mathrm{g} \in \mathrm{L_p}(\mathbb{D}^+; \mathbb{C}), \mathrm{p} > 2$, $\Upsilon \in \mathrm{L_2}(\mathbb{R}, \mathbb{C}) \cap C(\partial\mathbb{D}^+, \mathbb{C}), \mathrm{c} \in \mathbb{C}$

is solvable if and only if for $z \in \mathbb{D}^+$,

$$\begin{aligned}\frac{1}{2\pi i}\int_{\partial\mathbb{D}^+} \left(\Upsilon(\varsigma) - \overline{\varsigma}\, g(\varsigma)\right)\left[\frac{-1}{\varsigma - \bar{z}} + \frac{1}{\varsigma(1 - \varsigma\bar{z})}\right] d\varsigma \\ + \frac{1}{\pi}\int_{\mathbb{D}^+} g(\varsigma)\left[\frac{\bar{z}}{(\varsigma - \bar{z})^2} + \frac{\bar{z}}{(1 - \varsigma\bar{z})^2}\right] d\xi d\acute{\eta} = 0.\end{aligned} \tag{3}$$

The unique solution then is

$$\begin{aligned}\omega(z) = c - \frac{1}{2\pi i}\int_{\partial\mathbb{D}^+} \left(\Upsilon(\varsigma) - \overline{\varsigma}\, g(\varsigma)\right)\left[log\left(\frac{\varsigma - z}{\varsigma}\right) - log(1 - \varsigma z)\right]\frac{d\varsigma}{\varsigma} - \frac{1}{\pi}\int_{\mathbb{D}^+} g(\varsigma)\left[\frac{z}{\varsigma(\varsigma - z)}\right. \\ \left. + \frac{\mathrm{z}}{1 - \varsigma z}\right] d\xi d\acute{\eta}.\end{aligned} \tag{4}$$

By the help of Theorem 2, we have the following theorem, which is a special form of Neumann problem.

Theorem 3. (Karaca, 2024b) The problem

$\omega_{\bar{z}} = \mathrm{g(z)}$ in $\mathbb{D}^+$, $z\,\omega_z = \Upsilon$ on $\partial\mathbb{D}^+$, $\omega(0) = \mathrm{c}$

for $\mathrm{g} \in \mathrm{L_p}(\mathbb{D}^+; \mathbb{C}), \mathrm{p} > 2$, $\Upsilon \in \mathrm{L_2}(\mathbb{R}, \mathbb{C}) \cap C(\partial\mathbb{D}^+, \mathbb{C}), \mathrm{c} \in \mathbb{C}$

is solvable if and only if for $z \in \mathbb{D}^+$,

$$\frac{1}{2\pi i}\int_{\partial\mathbb{D}^+} \Upsilon(\varsigma)\left[\frac{-1}{\varsigma - \bar{z}} + \frac{1}{\varsigma(1 - \varsigma\bar{z})}\right] d\varsigma + \frac{1}{\pi}\int_{\mathbb{D}^+} g(\varsigma)\left[\frac{\bar{z}}{(\varsigma - \bar{z})^2} + \frac{\bar{z}}{(1 - \varsigma\bar{z})^2}\right] d\xi d\acute{\eta} = 0. \tag{5}$$

The unique solution then is

$$\omega(z) = c - \frac{1}{2\pi i}\int_{\partial\mathbb{D}^+} \Upsilon(\varsigma)\left[log\left(\frac{\varsigma - z}{\varsigma}\right) - log(1 - \varsigma z)\right]\frac{d\varsigma}{\varsigma} - \frac{1}{\pi}\int_{\mathbb{D}^+} g(\varsigma)\left[\frac{z}{\varsigma(\varsigma - z)} + \frac{\mathrm{z}}{1 - \varsigma z}\right] d\xi d\acute{\eta}. \tag{6}$$

2. The Dirichlet-Neumann Problem

In this section, we establish the theoretical foundation necessary for analyzing the BVPs presented in later sections. We begin by reviewing the inhomogeneous Cauchy-Riemann and Bitsadze equations within the upper half unit disc, outlining their significance and

mathematical properties. This groundwork is essential for formulating the solvability conditions and deriving explicit solutions.

The subsequent results build upon previously known theorems, extending them to encompass more complex boundary conditions. By leveraging analytical techniques and employing function spaces suited to the problem's geometry, we derive conditions that guarantee the existence and uniqueness of solutions.

Theorems 4 and 5, presented below, address the Dirichlet-Neumann problem and a more general boundary value problem for the inhomogeneous Bitsadze equation, respectively. These results highlight the interplay between boundary conditions and the inhomogeneous nature of the governing equations, providing a robust framework for further analysis.

Theorem 4. The Dirichlet-Neumann problem for the inhomogeneous Bitsadze equation in the upper half unit disc

$\omega_{\bar{z}\bar{z}} = \mathrm{g(z)}$ in $\mathbb{D}^+, \omega = \Upsilon_0,\ \partial_\nu \omega_{\bar{z}} = \Upsilon_1$ on $\partial\mathbb{D}^+, \quad \omega_{\bar{z}}(0) = \mathrm{c},$

for $\mathrm{g} \in \mathrm{L_p}(\mathbb{D}^+;\mathbb{C}), \mathrm{p} > 2,\ \Upsilon_0, \Upsilon_1 \in \mathrm{L_2}(\mathbb{R},\mathbb{C}) \cap C(\partial\mathbb{D}^+,\mathbb{C}), \mathrm{c} \in \mathbb{C}$ is solvable if and only if for $z \in \mathbb{D}^+$

$$
\begin{aligned}
c + \frac{1}{2\pi i}\int_{\partial\mathbb{D}^+} \Upsilon_0(\varsigma)\left[\frac{1}{\bar{z}(\varsigma-\bar{z})} + \frac{1}{\varsigma\bar{z}-1}\right]d\varsigma \\
+ \frac{1}{2\pi i}\int_{\partial\mathbb{D}^+} \left(\Upsilon_1(\varsigma) - \overline{\varsigma}\, g(\varsigma)\right)\frac{1-|z|^2}{|z|^2}\left[log\left(\frac{\varsigma - z}{\varsigma}\right) - log(1-\varsigma z)\right]\frac{d\varsigma}{\varsigma} \\
+ \frac{1}{\pi}\int_{\mathbb{D}^+} g(\varsigma)(|z|^2 - |t|^2)\left[\frac{1}{\bar{z}\varsigma(\mathrm{z}-\varsigma)} + \frac{1}{\bar{z}(\mathrm{z}\varsigma - 1)}\right]d\xi d\acute{\eta} = 0
\end{aligned} \tag{7}
$$

and

$$
\begin{aligned}
\frac{1}{2\pi i}\int_{\partial\mathbb{D}^+} \left(\Upsilon_1(\varsigma) - \overline{\varsigma}\, g(\varsigma)\right)\left[\frac{-1}{\varsigma - \bar{z}} + \frac{1}{\varsigma(1-\varsigma\bar{z})}\right]d\varsigma + \frac{1}{\pi}\int_{\mathbb{D}^+} g(\varsigma)\left[\frac{\bar{z}}{(\varsigma - \bar{z})^2} + \frac{\bar{z}}{(1-\varsigma\bar{z})^2}\right]d\xi d\acute{\eta} \\
= 0.
\end{aligned} \tag{8}
$$

The solution then is

$$
\begin{aligned}
\omega(z) = c\bar{z} + \frac{1}{2\pi i}\int_{\partial\mathbb{D}^+} \Upsilon_0(\varsigma)\left[\frac{1}{\varsigma - \mathrm{z}} + \frac{\mathrm{z}}{\varsigma\mathrm{z} - 1}\right]d\varsigma \\
+ \frac{1}{2\pi i}\int_{\partial\mathbb{D}^+} \left(\Upsilon_1(\varsigma) - \overline{\varsigma}\, g(\varsigma)\right)\frac{1-|z|^2}{z}\left[log\left(\frac{\varsigma - z}{\varsigma}\right) - log(1-\varsigma z)\right]\frac{d\varsigma}{\varsigma} \\
+ \frac{1}{\pi}\int_{\mathbb{D}^+} g(\varsigma)(|\varsigma|^2 - |z|^2)\left[\frac{1}{\varsigma(\varsigma - z)} + \frac{1}{1-\varsigma z}\right]d\xi d\acute{\eta}.
\end{aligned} \tag{9}
$$

Proof. The problem is equivalent to the system

$\omega_{\bar{z}} = \mathrm{u}$ in $\mathbb{D}^+,\ \omega = \Upsilon_0$ on $\partial\mathbb{D}^+,$

$u_{\bar{z}} = \mathrm{g(z)}$ in $\mathbb{D}^+,\ \partial_\nu \mathrm{u} = \Upsilon_1$ on $\partial\mathbb{D}^+,\ \mathrm{u}(0) = \mathrm{c}.$

The solvability conditions are

$$
\frac{1}{2\pi i}\int_{\partial\mathbb{D}^+} \Upsilon_0(\varsigma)\left[\frac{1}{\varsigma - \bar{z}} + \frac{\bar{z}}{\varsigma\bar{z} - 1}\right]d\varsigma - \frac{1}{\pi}\int_{\mathbb{D}^+} u(\varsigma)\left[\frac{1}{\varsigma - \bar{z}} + \frac{\bar{z}}{\varsigma\bar{z} - 1}\right]d\xi d\acute{\eta} = 0 \tag{10}
$$

and

$$\frac{1}{2\pi i}\int_{\partial\mathbb{D}^+}\left(\Upsilon_1(\varsigma)-\overline{\varsigma}\,g(\varsigma)\right)\left[\frac{-1}{\varsigma-\bar{z}}+\frac{1}{\varsigma(1-\varsigma\bar{z})}\right]d\varsigma+\frac{1}{\pi}\int_{\mathbb{D}^+}g(\varsigma)\left[\frac{\bar{z}}{(\varsigma-\bar{z})^2}+\frac{\bar{z}}{(1-\varsigma\bar{z})^2}\right]d\xi d\acute{\eta}=0 \tag{11}$$

and the unique solutions are

$$\omega(z)=\frac{1}{2\pi i}\int_{\partial\mathbb{D}^+}\Upsilon_0(\varsigma)\left[\frac{1}{\varsigma-\mathrm{z}}+\frac{\mathrm{z}}{\varsigma\mathrm{z}-1}\right]d\varsigma-\frac{1}{\pi}\int_{\mathbb{D}^+}u(\varsigma)\left[\frac{1}{\varsigma-\mathrm{z}}+\frac{\mathrm{z}}{\varsigma\mathrm{z}-1}\right]d\xi d\acute{\eta} \tag{12}$$

and

$$u(z)=c-\frac{1}{2\pi i}\int_{\partial\mathbb{D}^+}\left(\Upsilon_1(\varsigma)-\overline{\varsigma}\,g(\varsigma)\right)\left[log\left(\frac{\varsigma-z}{\varsigma}\right)-log(1-\varsigma z)\right]\frac{d\varsigma}{\varsigma}-\frac{1}{\pi}\int_{\mathbb{D}^+}g(\varsigma)\left[\frac{z}{\varsigma(\varsigma-z)}+\frac{\mathrm{z}}{1-\varsigma z}\right]d\xi d\acute{\eta} \tag{13}$$

according to Theorems 1 and 2. Substituting the Eq. (13) into the Eqs. (10) and (12), we get the desired result.

Theorem 5. The boundary value problem for the inhomogeneous Bitsadze equation in the upper half unit disc

$\omega_{\bar{z}\bar{z}}=g(z)\ in\ \mathbb{D}^+,\ \omega=\Upsilon_0,\ z\omega_{z\bar{z}}=\Upsilon_1$ on $\partial\mathbb{D}^+,\ \omega_{\bar{\mathrm{z}}}(0)=\mathrm{c}$

is solvable for $\mathrm{g}\in \mathrm{L}_1(\mathbb{D}^+;\mathbb{C}),\ \Upsilon_0,\Upsilon_1\in C(\partial\mathbb{D}^+,\mathbb{C}),\ \mathrm{c}\in\mathbb{C}$ if and only if for $z\in\mathbb{D}^+$,

$$\begin{aligned}c+\frac{1}{2\pi i}\int_{\partial\mathbb{D}^+}\Upsilon_0(\varsigma)\left[\frac{1}{\bar{z}(\varsigma-\bar{z})}+\frac{1}{\varsigma\bar{z}-1}\right]d\varsigma\\+\frac{1}{2\pi i}\int_{\partial\mathbb{D}^+}\left(\Upsilon_1(\varsigma)-\overline{\varsigma}\,g(\varsigma)\right)\frac{1-|z|^2}{|z|^2}\left[log\left(\frac{\varsigma-z}{\varsigma}\right)-log(1-\varsigma z)\right]\frac{d\varsigma}{\varsigma}\\+\frac{1}{\pi}\int_{\mathbb{D}^+}g(\varsigma)(|z|^2-|t|^2)\left[\frac{1}{\bar{z}\varsigma(z-\varsigma)}+\frac{1}{\bar{z}(z\varsigma-1)}\right]d\xi d\acute{\eta}=0\end{aligned} \tag{14}$$

and

$$\frac{1}{2\pi i}\int_{\partial\mathbb{D}^+}\Upsilon_1(\varsigma)\left[\frac{-1}{\varsigma-\bar{z}}+\frac{1}{\varsigma(1-\varsigma\bar{z})}\right]d\varsigma+\frac{1}{\pi}\int_{\mathbb{D}^+}g(\varsigma)\left[\frac{\bar{z}}{(\varsigma-\bar{z})^2}+\frac{\bar{z}}{(1-\varsigma\bar{z})^2}\right]d\xi d\acute{\eta}=0 \tag{15}$$

holds. The solution then is uniquely given by

$$\begin{aligned}\omega(z)=c\bar{z}+\frac{1}{2\pi i}\int_{\partial\mathbb{D}^+}\Upsilon_0(\varsigma)\left[\frac{1}{\varsigma-\mathrm{z}}+\frac{\mathrm{z}}{\varsigma\mathrm{z}-1}\right]d\varsigma\\+\frac{1}{2\pi i}\int_{\partial\mathbb{D}^+}\Upsilon_1(\varsigma)\frac{1-|z|^2}{z}\left[log\left(\frac{\varsigma-z}{\varsigma}\right)-log(1-\varsigma z)\right]\frac{d\varsigma}{\varsigma}\\+\frac{1}{\pi}\int_{\mathbb{D}^+}g(\varsigma)(|\varsigma|^2-|z|^2)\left[\frac{1}{\varsigma(\varsigma-z)}+\frac{1}{1-\varsigma z}\right]d\xi d\acute{\eta}.\end{aligned} \tag{16}$$

Proof. The proof follows the same steps as Theorem 4, but with Theorem 3 used in place of Theorem 2.

3. Conclusion

In this study, we analyzed the solvability and explicit solutions of the Dirichlet, Neumann, and Dirichlet-Neumann BVPs for inhomogeneous equations in the upper half unit disc. By leveraging fundamental techniques from complex analysis and functional spaces, we established necessary and sufficient conditions for the existence of solutions. Our results provide a systematic framework for solving these problems and extend previously known results by incorporating mixed boundary conditions.

A key contribution of this work is the explicit construction of solutions for the Dirichlet-Neumann problem, which highlights the interplay between different types of boundary conditions. By expressing solutions in a closed form, we offer a constructive approach that can be directly applied in further mathematical and applied studies. These findings not only deepen our theoretical understanding of BVPs but also have potential applications in mathematical physics, fluid dynamics, and engineering problems where such equations naturally arise.

Moreover, the methodology presented in this study can be extended to more general settings, including higher-order equations and different geometric configurations. Future research directions could explore nonlinear extensions of these problems, the impact of additional boundary constraints, and numerical methods for approximating solutions in cases where explicit formulas are difficult to obtain.

In conclusion, this study contributes to the broader literature on BVPs in complex domains by providing a rigorous analytical framework for inhomogeneous equations in the upper half unit disc. The results presented here not only unify and extend existing theories but also pave the way for new developments in applied mathematics and theoretical physics.

Authorship Contribution Statement

The author is solely responsible for the conceptualization, methodology, analysis, and manuscript preparation.

Conflict of Interest

The author declares no conflict of interest.

References

Begehr, H., Burgumbayeva, S., & Shupeyeva, B. (2017). Remark on Robin problem for Poisson equation. *Complex Variables and Elliptic Equations, 62*(10), 1589–1599. https://doi.org/10.1080/17476933.2017.1303052

Begehr, H., & Vaitekhovich, T. (2008). Iterated Dirichlet problem for the higher order Poisson equation. *Le Matematiche, 63*(1), 139–154.

Begehr, H., & Vaitekhovich, T. (2012). Harmonic Dirichlet problem for some equilateral triangle. *Complex Variables and Elliptic Equations, 57*(2–4), 185–196. https://doi.org/10.1080/17476933.2011.598932

Begehr, H., Du, J., & Wang, Y. (2008). A Dirichlet problem for polyharmonic functions. *Annali di Matematica Pura ed Applicata, 187*, 435–457. https://doi.org/10.1007/s10231-007-0050-5

Chaudhary, A., & Kumar, A. (2009). Boundary value problems in upper half plane. *Complex Variables and Elliptic Equations, 54*(5), 441–448. https://doi.org/10.1080/17476930902750840

Darya, A., & Tagizadeh, N. (2024). On the Dirichlet boundary value problem for the Cauchy-Riemann equations in the half disc. *European Journal of Mathematical Analysis, 4*(15), 1–9. https://doi.org/10.28924/ada/ma.4.15

Kalmenov, T. S., Koshanov, B. D., & Nemchenko, M. Y. (2008). Green function representation for the Dirichlet problem of the polyharmonic equation in a sphere. *Complex Variables and Elliptic Equations, 53*(2), 177–183. https://doi.org/10.1080/17476930701671726

Karaca, B. (2024a). Schwarz problem for model partial differential equations with one complex variable. *Sakarya University Journal of Science, 28*(2), 410–417. https://doi.org/10.16984/saufenbilder.1390617

Karaca, B. (2024b). A note on complex combined boundary value problem for the nonhomogeneous tri-analytic equation. *Boletim da Sociedade Paranaense de Matemática, 42*, 1–7. https://doi.org/10.5269/bspm.62443

Karaca, B. (2021, June 23–27). Schwarz-(Dirichlet-Neumann) problem for the nonhomogeneous tri-analytic equation. *Fifth International Conference of Mathematical Sciences (ICMS 2021)*, Maltepe University, Istanbul, Turkey.

Karachik, V. (2019). Green's function of Dirichlet problem for biharmonic equation in the ball. *Complex Variables and Elliptic Equations, 64*(9), 1500–1521. https://doi.org/10.1080/17476933.2018.1536702

Karachik, V. V. (2013). Solution of the Dirichlet problem with polynomial data for the polyharmonic equation in a ball. *Differential Equations, 51*(8), 1033-1042. https://doi.org/10.1134/S0012266115080078

Kumar, A., & Prakash, R. (2006). Mixed boundary value problems for the inhomogeneous polyanalytic equation. *Complex Variables and Elliptic Equations, 51*, 209–223. https://doi.org/10.1080/17476930500454134

Wang, Y., & Du, J. (2004). On Riemann boundary value problem for polyanalytic functions on the real axis. *Acta Mathematica Scientia, 24*(4), 663–671. https://doi.org/10.1016/S0252-9602(17)30251-5